PNL-6640 Vol. 2
UC-812

2F

Storage of LWR Spent Fuel in Air

Volume 2—Microstructural Characterization of Low-Temperature Oxidized LWR Spent Fuel

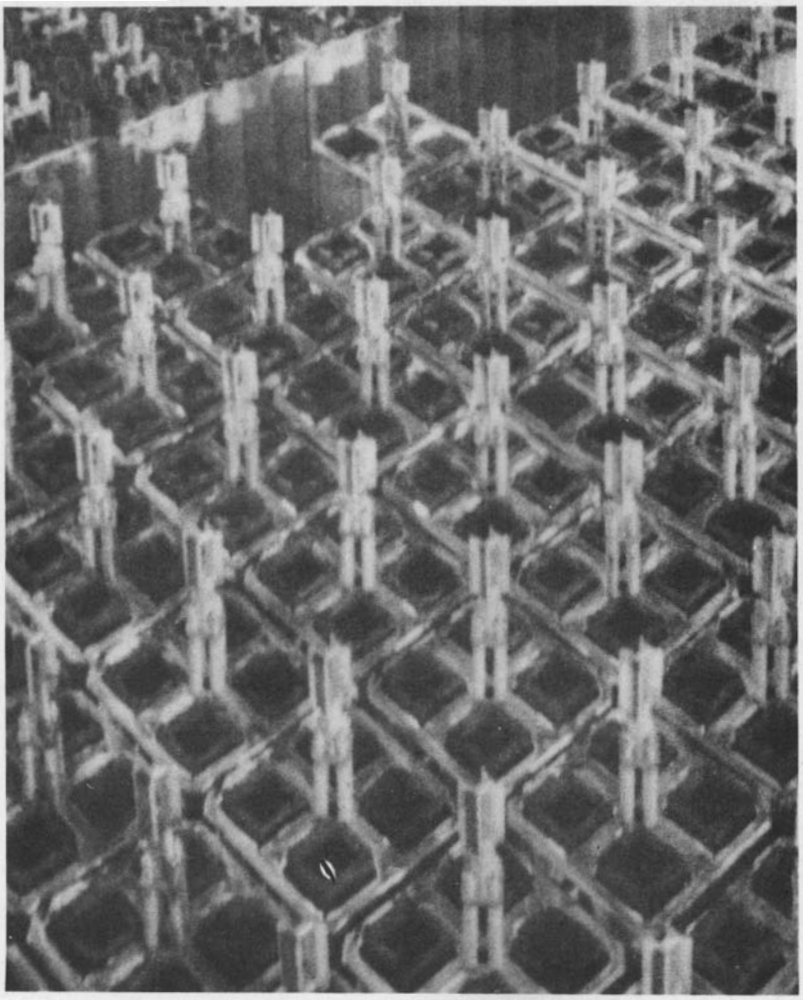

December 1989

Prepared for the U.S. Department of Energy
under Contract DE-AC06-76RLO 1830

Pacific Northwest Laboratory
Operated for the U. S. Department of Energy
by Battelle Memorial Institute

PNL-6640 Vol. 2

DISCLAIMER

PACIFIC NORTHWEST LABORATORY
operated by
BATTELLE MEMORIAL INSTITUTE
for the
UNITED STATES DEPARTMENT OF ENERGY
under Contract DE-AC06-76RLO 1830

Printed in the United States of America

Available to DOE and DOE contractors from the
Office of Scientific and Technical Information, P.O. Box 62, Oak Ridge, TN 37831;
prices available from (615) 576-8401. FTS 626-8401.

Available to the public from the National Technical Information Service,
U.S. Department of Commerce, 5285 Port Royal Rd., Springfield, VA 22161.

NTIS Price Codes, Microfiche A01

Printed Copy

Pages	Price Codes
001-025	A02
026-050	A03
051-075	A04
076-100	A05
101-125	A06
126-150	A07
151-175	A08
176-200	A09
201-225	A10
226-250	A11
251-275	A12
276-300	A13

PNL-6640 Vol. 2
UC-812

STORAGE OF LWR SPENT FUEL IN AIR

VOLUME 2 -- MICROSTRUCTURAL CHARACTERIZATION OF LOW-TEMPERATURE OXIDIZED LWR SPENT FUEL

L. E. Thomas
R. W. Knoll[a]
L. A. Charlot
J. E. Coleman
E. R. Gilbert, Project Manager

December 1989

Prepared for
the U.S. Department of Energy
under Contract DE-AC06-76RLO 1830

Pacific Northwest Laboratory
Richland, Washington 99352

(a) Johnson Controls, Inc., Madison Wisconsin

PREFACE

This report is the second of five to appear in a series entitled Storage of Spent Fuel in Air. The reports are being prepared for the U.S. Department of Energy, Office of Civilian Radioactive Waste Management, through the Commercial Spent Fuel Management Program of the Richland Operations Office on the storage of spent fuel in air. The program is managed by the Pacific Northwest Laboratory. Subjects covered in each volume in the series are as follows:

- Volume I--Design and Operation of an Experimental Facility for Conducting Spent Fuel Oxidation Tests.
- Volume II--Microstructural Characterization of Low-Temperature Oxidized LWR Spent Fuel.
- Volume III--Results from Spent Fuel Oxidation Tests in Air.
- Volume IV--Microstructural Characterization of Oxidized LWR Spent Fuel Rod Segments With Intentionally Breached Cladding.
- Volume V--Temperature Limits for Storing LWR Spent Fuel in Air.

ABSTRACT

An experimental program is being conducted at Pacific Northwest Laboratory (PNL) to determine the oxidation response of light-water-reactor (LWR) spent fuels under conditions appropriate to fuel storage in air. The program is designed to investigate several independent variables that might affect the oxidation behavior of spent fuel. Included are temperature (135 to 230°C), fuel burnup (to about 34 MWd/kgM), reactor type (pressurized and boiling water reactors), moisture level in the air, and the presence of a high gamma field. In continuing tests with declad spent fuel and nonirradiated UO_2 specimens, oxidation rates were monitored by weight-gain measurements and the microstructures of subsamples taken during the weighing intervals were characterized by several analytical methods. The oxidation behavior indicated by weight gain and time to form powder will be reported in Volume III of this series. The characterization results obtained from x-ray diffractometry, transmission electron microscopy, scanning electron microscopy, and Auger electron spectrometry of oxidized fuel samples are presented in this report.

SUMMARY

Storage of spent fuel in dry air has been proposed as an alternative to storage in inert gas. To determine recommended allowable time, temperature, and humidity conditions for storing and handling spent fuel in air, a series of long-time oxidation tests with spent fuel and nonirradiated UO_2 is being conducted in controlled-atmosphere ovens. The purpose of this report is to present the results of microstructural characterization of oxidized fuel samples from the tests. In these continuing tests, the oxidation rates of 144 specimens consisting of declad (bare) fuel pellet fragments and representing a wide variety of material and test conditions are being monitored by weight-gain measurements. Oxidation of bare fuel fragments is considered a worst-case test condition for oxidation of spent fuel contained in fuel rods with defective cladding. Test temperatures covering the range appropriate to dry storage are 135, 150, 170, 190, 210, and 230°C. The tests are conducted in air at three different humidity (dewpoint) levels and in the presence of an intense gamma radiation field (1.3×10^5 R/h) to simulate actual spent fuel storage conditions.

At intervals during the tests, selected samples of oxidized spent fuel and nonirradiated UO_2 were removed from the test ovens for microstructural characterization by X-ray diffractometry (XRD), transmission electron microscopy (TEM), scanning electron microscopy (SEM), and scanning Auger electron microscopy (SAM). The purpose of this characterization is to provide a physical basis for understanding oxidation behavior in spent fuel in order to support the development of models for predicting safe limits for dry storage and handling of LWR fuel in air. Also, microstructural characterization of the oxidized samples is used to determine whether powder formation during the tests could be used as an indicator of U_3O_8 formation and to determine the cause of unusually high weight gains observed in some of the tests. A key goal of this analysis is to determine the conditions for forming U_3O_8 because of the important implications of U_3O_8-induced fuel swelling and powder formation on spent fuel dry storage.

Microstructural characterization of bare fragment and powder samples by four different analytical techniques is covered in this report. The results

are related to average oxygen-to-metal atom ratios (O/Ms) derived from the weight-gain measurements by assuming that all weight gain was caused by oxygen. The oxidation kinetics data will be reported in Volume III.

The results of the characterization work show that LWR spent fuel at 130 to 230°C oxidizes by different mechanisms and forms a different sequence of oxidation product phases than nonirradiated UO_2. Initial oxidation of spent fuel occurs preferentially along grain boundaries believed to contain closely spaced fission-gas bubbles. Small grain boundary gas bubbles were observed in nonoxidized spent fuel by TEM. The intergranular bubbles together with fabrication-induced porosity in the fuel, may provide easy paths for oxygen penetration into the fuel. Oxidation initially produced two-phase structures with U_4O_9 along the grain boundaries and unaltered UO_2 at the grain centers. The lattice shrinkage of the $UO_2 \rightarrow U_4O_9$ transformation caused separation of the grain boundaries and may have been the cause of powder formation observed in specimens exposed at 135 and 150°C. Powder that formed on several specimens at 135°C and 150°C after relatively short exposures consisted of large polycrystalline clusters containing mainly UO_2 and U_4O_9.

XRD analysis of samples from spent fuel fragments oxidized at 150°C to 190°C for up to ~17,000 h showed significantly more U_4O_9 and less U_3O_8 than expected from the weight-gain data. The U_4O_9 in these samples contained closely spaced microcracks and unidentified vein-like structures. As the oxidation weight gains increased, fine-grained U_3O_8 formed along the microcracks and grew at the expense of the U_4O_9 (and occasional U_3O_7) phases. Uranium oxide hydrates (schoepite and dehydrated schoepite), also formed. At extremely large weight gains (O/M > 3.2) observed for a few samples, schoepite, dehydrated schoepite and an unidentified phase, probably also a hydrate, predominated.

Powder that formed at 230°C consisted of loosely bound clusters containing a few grains each and was composed mainly of U_3O_8, dehydrated schoepite, and schoepite. In most samples, however, U_3O_8 formation did not produce powder.

The following are the main conclusions of the microstructural characterization work:

- LWR spent fuel exposed to air over the temperature range of 135 to 230°C oxidizes by different mechanisms and forms a different sequence of oxidation product phases than nonirradiated UO_2 under similar conditions. **The present understanding of the oxidation behavior of nonirradiated UO_2 has limited applicability for spent UO_2 fuel.**

- The onset of significant U_3O_8 formation occurs at higher weight gains in LWR spent fuel than in nonirradiated UO_2. **Formation of U_3O_8 in spent** fuel is delayed by slow oxidation kinetics at the temperatures of these tests, or the U_4O_9 oxidation product phase is stabilized in spent fuel.

- Powder formation is not a reliable indicator of U_3O_8 formation during low-temperature oxidation of spent fuel.

- High weight gains corresponding to O/Ms above 3.0, which occurred in some oxidation tests, is associated with formation of uranium oxide hydrates.

- Significant volume expansion of spent fuel as a result of oxidative phase transformations may occur by several mechanisms besides $U_4O_9 \rightarrow U_3O_8$ conversion. **Other proposed expansion mechanisms include formation** of uranium oxide hydrates, microcrack formation in U_4O_9 or U_3O_7, and bubble formation by release of trapped fission gases during oxidation. Microstructural evidence of these effects was observed during the work.

ACKNOWLEDGEMENTS

This work was supported by the U.S. Department of Energy (DOE) Office of Civilian Radioactive Waste Management through the DOE Richland Operations Office, under the Commercial Spent Fuel Management Program. The comments and suggestions of J. O. Barner, J. M. Creer, J. W. Nageley, and E. P. Simonen in critically reviewing the report manuscript are sincerely appreciated. Special recognition is given to T. K. Campbell and M. E. Cunningham of PNL for their guidance and comments during this work.

CONTENTS

FIGURES

TABLES

1.0 INTRODUCTION

Dry storage of light-water-reactor (LWR) spent fuel in air is being considered as an alternative to storage in an inert gas atmosphere or in water pools (wet storage) at reactor sites. A major concern of dry storage is oxidation of the uranium oxide (UO_2) fuel in the small fraction of fuel rods where the UO_2 is exposed to air because of a cladding breach. In particular, the oxidation of UO_2 to U_3O_8 produces swelling which can strain the cladding and cause a cladding breach to propagate. Conversion of even a fraction of the UO_2 in an LWR fuel rod to U_3O_8 might rupture the cladding, disperse respirable powders, and radioactively contaminate the storage vessel. Until allowable temperatures for storage of spent fuel in air are established, a modular vault design presently approved by the Nuclear Regulatory Commission for storage in nitrogen cannot be approved for storage in air (Roberts 1988). Therefore, it is important to define time and temperature conditions for fuel storage and handling in air such that cladding rupture will not occur during the storage period.

In addition, models for the oxidation behavior of spent fuel in air are needed 1) to identify allowable conditions for handling and storing the fuel in air before it is sealed for disposal in a repository, 2) to determine the period of storage in inerted atmosphere after which monitoring of the inert gas is no longer necessary, and 3) to predict fuel rod degradation during abnormal events.

At the present time, information needed to develop models for predicting oxidation behavior of fuel under postirradiation handling and storage conditions is lacking. Oxidation data for prolonged exposure times and low temperatures, and a better understanding of the mechanisms of oxidation in spent fuel, are needed. Present information on the stability of uranium oxides comes mostly from studies of nonirradiated UO_2 and may be inapplicable to spent fuel. Oxidation studies have indicated, for example, that spent fuel is more resistant to U_3O_8 formation than nonirradiated UO_2 (Einziger and Strain 1986; Campbell et al. 1987). Oxidation tests with spent fuel have not been carried out for the long periods at the low temperatures appropriate to

dry storage, and the possibility exists that the mechanism of U_3O_8 formation at low storage temperatures differs from the mechanisms known from short-time, high-temperature tests.

To obtain the information needed to develop predictive models of spent fuel oxidation under dry storage conditions, long-term oxidation tests are being conducted at Pacific Northwest Laboratory (PNL) as part of the Commercial Spent Fuel Management (CSFM) Program. In these tests, bare (declad) fuel specimens from various commercial LWRs, along with nonirradiated UO_2 samples, are being held in controlled air atmospheres at selected temperatures ranging from 135 to 230°C and at three different humidity (dewpoint) conditions (Campbell et al. 1987). Bare fuel fragments were used as a worst-case scenario for oxidation; i.e., no benefit from potentially protective cladding. The tests are being conducted in the presence of an intense gamma radiation field (1.3×10^5 R/h) to simulate actual spent fuel storage conditions (Thornhill, Campbell and Thornhill 1988). Specimens are periodically removed from their ovens and weighed to monitor oxidation weight gain. At the end of the tests, in 1990, some specimens will reach exposures as high as 35,000 hours (4 years).

At intervals during the oxidation tests, small samples of the oxidized fuel fragments were removed from the test ovens and characterized by several analytical methods: the analyses and their purposes were a) X-ray diffraction (XRD) to identify phases by their crystal structures, b) transmission electron microscopy (TEM) to examine local oxidation microstructures and to identify the oxidation products and their formation mechanisms, c) scanning electron microscopy (SEM) to examine grain boundaries and other surfaces exposed by fracturing the samples, and d) scanning Auger microscopy (SAM) to chemically identify oxidation phases on fracture surfaces. The results of the microstructural examinations and analyses of samples taken from the specimens after 4,600 to 17,000 hours of exposure are the subject of this report.

1.1 OBJECTIVES

The objectives of the work reported here were to perform detailed characterization of oxidized fuel samples from the high-gamma oxidation test, and thereby to 1) determine the microstructural and microchemical changes that occur in LWR spent fuel as it oxidizes to higher oxidation states, 2) correlate these changes with the oxidation weight gains, and 3) identify possible relationships between the oxidation phases, microstructural changes in the fuel due to oxidation, and cladding degradation. The work was done to develop an understanding of the microstructural aspects of spent fuel oxidation that could be incorporated into models for determining acceptable fuel storage and handling conditions. The purpose of this report, Volume II, is to present and discuss data obtained by characterization of the oxidized bare fuel samples.

A previous report in this series, Volume I, described the design and operation of the oxidation test facility (Thornhill, Campbell, and Thornhill 1988). A description of the oxidation tests, including a tabulation of interim oxidation kinetics data, has been reported separately from this report series by Campbell et al. (1987). Complete oxidation kinetics data will be reported in Volume III. Volume IV will cover the microstructural analysis of the oxidized fuel in artificially breached fuel rods. Recommended temperature limits for air dry storage of LWR spent fuel rods will be presented in Volume V.

A further goal of this work was to determine if powder formation during the oxidation tests was a reliable indicator of U_3O_8 formation. In tests with nonirradiated UO_2, U_3O_8 formation has been associated with degradation of initially solid samples into a sooty powder. Powders that formed during the oxidation tests were analyzed to identify the oxidation product phases and determine their relative amounts.

1.2 REPORT OVERVIEW

The report is organized as follows. To provide a framework for presenting the analytical results, a brief review of UO_2 oxidation behavior, based on previous studies, is provided in Section 2.0. Important aspects of the

spent fuel oxidation tests are also briefly described. The four analytical techniques used in this study, and the types of information expected from these techniques, are then described in Section 3.0. Sample preparation techniques and instrument modifications that have not been previously reported are also described. Data obtained from characterization of the oxidized fuel samples follow in Section 4.0. Available data from the TEM, XRD, SAM, and SEM studies are integrated to show how the microstructures change with increasing oxygen-to-uranium (metal) (O/M) ratios. The degree of oxidation in the test samples is expressed by the average O/M ratios derived by assuming that weight gains measured during the tests are entirely caused by oxygen uptake. In fact, part of the weight gains are caused by formation of uranium oxide hydrates.

Because of special interest in time-to-powder data for spent fuel (Campbell et al. 1987) and in the characteristics of powder that spalled from some specimens during the oxidation tests, results obtained from examination of several powder samples are described separately, in Section 4.3. The results of the work are discussed in Section 5.0 and conclusions are presented in Section 6.0. Section 7.0 presents plans for continuing work. Reference X-ray diffraction data useful for identification of known uranium oxide and uranium oxide hydrate phases, detailed review information concerning oxide and hydrate phases formed by oxidizing UO_2, and supplemental information concerning the analytical equipment and methods used in this work are given in separate appendices.

2.0 OVERVIEW OF UO_2 OXIDATION

UO_2 is thermodynamically unstable in air, and its oxidation behavior is rather complex. At the relatively low temperatures of interest for spent fuel storage, below 230°C, UO_2 transforms through a series of intermediate oxides to UO_3; in moist air, uranium oxide hydrates can also result. Materials parameters (e.g., porosity and grain size), irradiation parameters (e.g., burnup and local fuel operating temperatures), and test variables (oxidation temperature and composition of the oxidizing atmosphere) can affect the nature of the oxidation products and their rates of formation.

Since the 1940s, the uranium-oxygen system has been studied extensively to identify the higher oxides that form from UO_2 and to determine the phase relationships. These studies have yielded no general agreement on the stabilities or stoichiometries of the intermediate U-O phases; many different phase diagrams for the UO_2-UO_3 system are found in the literature, and these often use different names for the same phases. An "accepted" phase diagram for the UO_2-UO_3 system is provided in Figure 2.1. Other phase diagrams for this system are found in various reviews (Weigel and Hoekstra 1986; Colmenares 1975, 1984; Abmann et al. 1982; Keller 1973; Smith 1984) or other references (Roth, Negas and Cook 1981).

In addition, the present understanding of UO_2 oxidation is based almost entirely on studies of nonirradiated material. Most experimenters have worked with fine powders of nonirradiated UO_2 under conditions of relatively high temperature to approach equilibrium in short times. As a result, the information is directly applicable to 1) oxidation of nonirradiated UO_2, 2) surface-controlled, rather than volume-controlled reactions, and 3) high-temperature reactions. Very little characterization work on oxidized spent fuel has been reported.

In this section, a simplified view of oxidation in nonirradiated UO_2 is presented to provide a basis for interpreting the process of oxidation in spent fuel. Also, the oxidation behavior of UO_2 spent fuel is briefly reviewed. Supplemental detailed information on the phases formed by

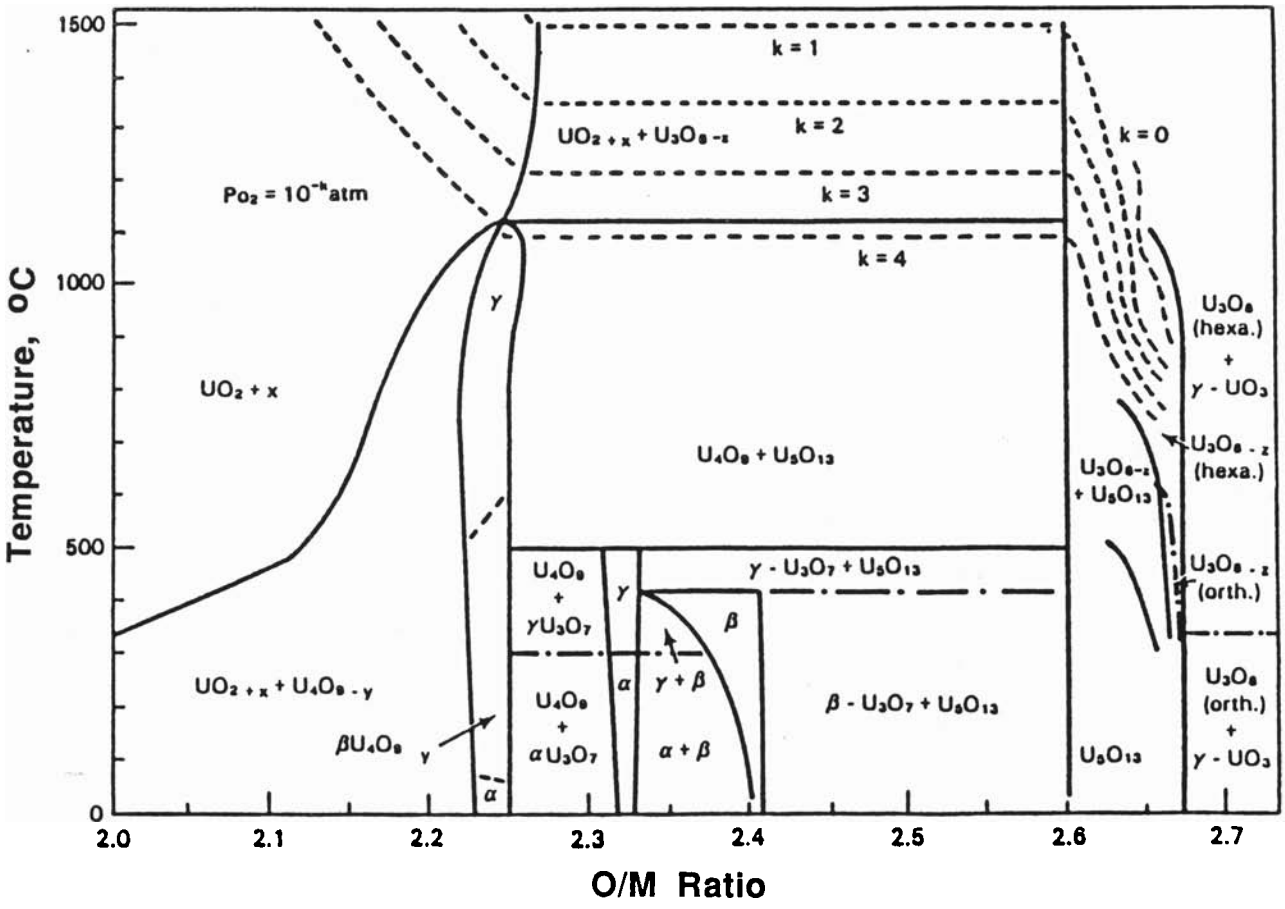

FIGURE 2.1. Example of a Currently Accepted Uranium-Oxygen Phase Diagram

oxidation of nonirradiated UO_2 and on identification of these phases by X-ray diffractometry is given in the tables and figures of Appendixes A and B.

2.1 OXIDATION PHASES IN NONIRRADIATED UO_2

Numerous different uranium oxide phases have been identified by X-ray diffraction. For example, the international JCPDS database of X-ray powder diffraction standards (JCPDS 1988) includes 36 listings of U-O phases from UO_2 to UO_3. Comparing these patterns, shown in Figure A.1 of Appendix A, reveals a simplification that is often overlooked. Disregarding phases formed in high pressure experiments (Hoekstra, Siegel and Gallapher 1970),

most of the phases between UO_2 and UO_3 are variations of just two basic crystal structures: the fluorite structure of UO_2 and the uranyl-bonded structure of α-U_3O_8.

Within this classification, variants of the UO_2 structure include several polymorphs of U_4O_9 and U_3O_7. Many of the phases with different assigned names, e.g., α-U_2O_5, α-U_3O_8, and α-UO_3 (JCPDS Cards 32-1403, 31-1425, and 31-14160), have obviously similar crystal structures. Except for α-UO_3, the six crystalline polymorphs of UO_3 fall outside this classification; most U-O phase diagrams indicate γ-UO_3 as the only stable form.

In Figure 2.2, a simplified phase diagram shows the approximate locations of the commonly named phases: UO_2, U_4O_9, U_3O_7, U_3O_8, and UO_3. Polymorphs, alternative names, and conditions of formation for these phases are discussed in Appendix B. Table B.1 provides crystallographic and density information for the UO_2-UO_3 phases.

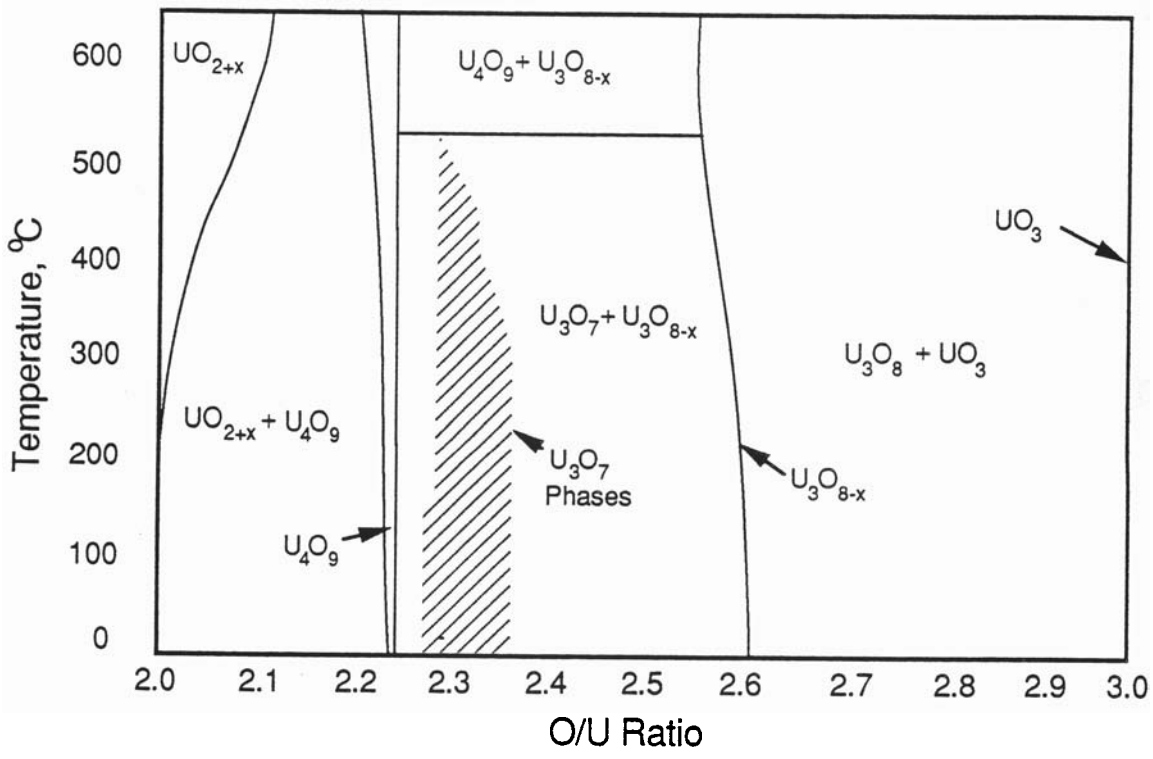

FIGURE 2.2. Simplified UO_2-UO_3 Phase Diagram

Phase development during oxidation of UO_2 can be further understood by considering how adding oxygen to UO_2 affects the crystal structures. A generalized phase development sequence for nonirradiated UO_2 at oxidation temperatures between 135 and 230°C is shown in Figure 2.3. Also shown in this figure are the X-ray densities, based on lattice parameters determined by XRD. Near 200°C, oxygen has little solubility in UO_2; the x in UO_{2+x} is <0.001. Excess oxygen in UO_{2+x} forms U_4O_9, a distinct phase based on the UO_2 structure but containing ordered or partially ordered oxygen defect complexes. As shown in the phase diagrams, U_4O_9 coexists with UO_2 over a wide range of compositions. Formation of U_4O_9 from UO_2 shrinks the lattice by about 0.4%. The U_4O_9 phase is usually considered a solid-solution having a range of compositions and is not actually stoichiometric $UO_{2.25}$.

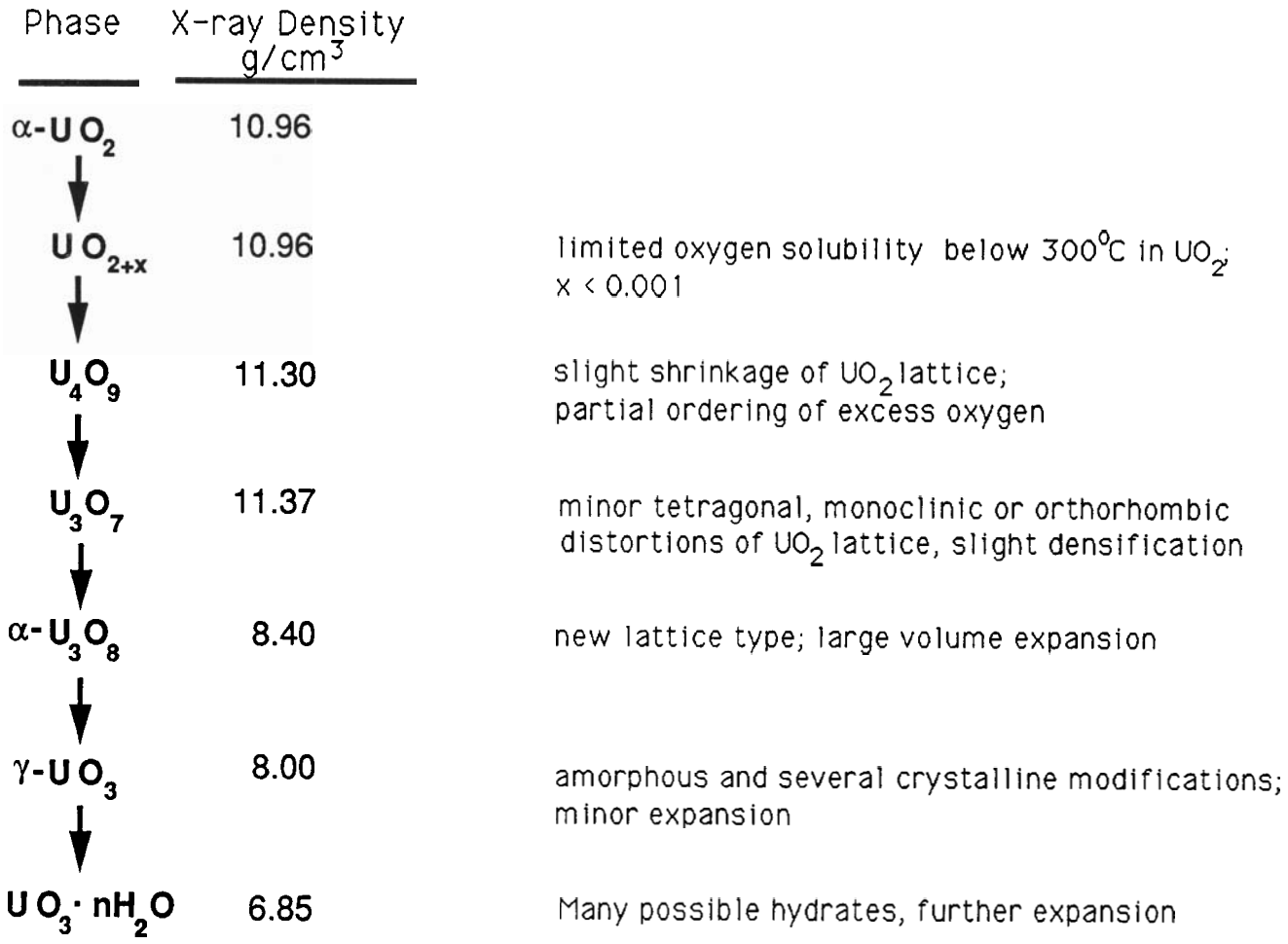

FIGURE 2.3. Low-Temperature Oxidation Sequence Beginning with UO_2

Further oxygen additions beyond U_4O_9 distort the fluorite lattice to tetragonal, monoclinic or orthorhombic variants--the U_3O_7 phases. The distortions are slight; tetragonal and monoclinic variants of U_3O_7, for example, still have nearly cubic symmetry (see Table A.1). Compositions of these phases range from about $UO_{2.3}$ (α-U_3O_7) to $UO_{2.5}$ (γ-U_2O_5). Based on X-ray data, the U_3O_7 phases are slightly denser than U_4O_9.

At the limit of oxygen accommodation in the fluorite structure, a new series of phases based on the U_3O_8 structure begins. Formation of U_3O_8 from U_4O_9 or U_3O_7 involves about a 30% density decrease and, consequently, large changes in sample dimensions. Stoichiometries of the U_3O_8-structure phases may range from $UO_{2.5}$ (U_2O_5) to $UO_{3.0}$.

Beyond U_3O_8, UO_3 phases representing several different structures and having slightly lower densities can form. One of the commonly observed UO_3 phases is amorphous or else has such a small grain size that it appears amorphous by X-ray diffraction.

UO_2 oxidation in the presence of water vapor also results in a series of hydrates with formulas of the type $UO_3.nH_2O$. Oxides beyond U_3O_8 are not found as natural minerals (Smith 1984), probably because these compounds have a strong affinity for water and for various cations.

2.2 OXIDATION OF UO_2 SPENT FUEL

Oxidation of irradiated (spent) UO_2 fuel has been studied less extensively than that of nonirradiated UO_2; most of the work has concentrated on temperatures above about 200°C, where oxidation kinetics are rapid (Campbell et al. 1987; Bennett, Price, and Wood 1987; Einziger, and Strain 1986; White and Gilbert 1986; White et al. 1983; Boase and Vandegraff 1977). Generally, the fuel oxidation behavior has been studied by measuring oxidation weight gains.

Several of these studies indicate that nonirradiated UO_2 and spent fuel have different oxidation behaviors, particularly with respect to powder formation. Nonirradiated UO_2 forms powders at lower weight gains and shorter oxidation periods. Powder formation during oxidation of nonirradiated UO_2 is usually assumed to be a visual indicator of U_3O_8 formation, although this

assumption has not been verified in all cases. Only Einziger, and Strain (1986) confirmed the presence of U_3O_8 phases in LWR fuel fragments oxidized above 283°C; other experimenters used weight-gain data to infer U_3O_8 formation.

A recent TEM study of oxidation in LWR fuels at 150 to 170°C (Thomas, Einziger, and Woodley 1989) shows that initial oxidation occurred preferentially along grain boundaries by forming γ-U_4O_9 directly from the UO_2. This observation is direct evidence of a difference in oxidation behavior between irradiated and nonirradiated UO_2. Studies of nonirradiated UO_2 pellets by X-ray diffraction and X-ray photoelectron spectrometry (XPS) (Taylor, Burgess, and Owen 1980; Allen, Tempest, and Tyler 1987) found that the β-U_3O_7 formed directly on UO_2 surfaces without intermediate U_4O_9 formation. TEM examinations of nonoxidized fuel (Thomas, McCarthy, and Gilbert 1986a,b; Thomas, and Guenther 1989) also suggested a correspondence between initial oxidation along grain boundaries and closely spaced fission gas microbubbles observed along the grain boundaries. By providing pathways for internal oxidation, irradiation-induced microstructures can change the rate-limiting mechanism of oxidation and thus affect initial oxidation rates. The apparent differences in stability of the intermediate oxides in spent fuel and nonirradiated UO_2 have not been explained.

2.3 SUMMARY OF UO_2 OXIDATION BEHAVIOR

Points to consider in understanding the oxidation behavior of irradiated and nonirradiated UO_2 include the following:

- The major oxides of uranium are UO_2, U_4O_9, U_3O_7, U_3O_8, and UO_3. Most of these have several structural variants, but (except for UO_3) are represented by just two basic structures.
- With increasing oxidation above UO_2, a major structural expansion (density decrease) accompanies the transformation from UO_2-structure phases (UO_2. U_4O_9, or U_3O_7) to U_3O_8. The ideal densities of the UO_2-structure phases increase with the addition of oxygen atoms to form U_4O_9 and U_3O_7.
- Existing U-O phase information was developed from studies of nonirradiated UO_2. A UO_2-UO_3 phase diagram for spent UO_2 fuel does not exist and there is evidence that the diagrams for nonirradiated material might be inapplicable for LWR fuels.

3.0 EXPERIMENTAL EQUIPMENT AND METHODS

A brief description of the oxidation tests was given in the Introduction. The tests have also been documented in detail by Campbell et al. (1987) and by Thornhill, Campbell, and Thornhill (1988). A description of some important aspects of the tests is repeated here to provide a background for the presentation and interpretation of the analytical results.

This section also includes a description of the methods used for preparing and examining the highly radioactive fuel samples. Additional background information on the analytical techniques, TEM, XRD, SEM and SAM, is given in Appendix C.

3.1 OXIDATION TESTS

In the oxidation tests, the weight-gain behavior of 144 bare fuel specimens is being tracked. The tests are being conducted within hermetically-sealed stainless steel ovens in a hot-cell at PNL. An array of twelve ovens are being used, and each oven holds twelve fuel specimens in individual aluminum boats. Each oven is maintained at a specified test temperature except during fuel weighing operations, when the oven is cooled to room temperature while each specimen is removed, weighed, and photographed. In addition to temperature, the effects of three different humidity levels on fuel oxidation are being studied. A matrix indicating the oven test temperatures and dewpoints is given in Table 3.1. To simulate the gamma field present under actual spent fuel storage conditions, a CsCl gamma source was placed in front of each oven door to provide a gamma dose rate of approximately 1.3×10^5 R/h.

Each oven contains eleven spent fuel specimens and one nonirradiated UO_2 specimen. The spent fuel specimens are from five different commercial LWR power reactors: the Shippingport, Point Beach, and H. B. Robinson pressurized water reactors (PWR), and the Quad Cities-1, and Monticello boiling water reactors (BWR). Fuel burnups range from 7.5 to 34 GWd/MTU. Each

TABLE 3.1. Nominal Temperature and Dewpoint for the Oxidation Test Ovens

Oven No.	Nominal Temperature, °C	Nominal Dewpoint, °C
1	150	20
2	150	40
3	170	20
4	190	20
5	190	40
6	135	40
7	150	0
8	190	0
9	210	20
10	135	0
11	170	20
12	230	20

oven contains a variety of fuel types and burnups. The characteristics and the oven location of each of the 144 fuel specimens are tabulated by Campbell et al. (1987).

Each nonirradiated fuel specimen consists of three PNL-fabricated UO_2 pellets weighing a total of about 16 grams. Each spent fuel specimen initially consisted of fragments with edge lengths ranging from approximately 2 to 10 mm, depending on fuel type and burnup. Initial specimen weights ranged from about 20 to 45 grams, and the largest individual fragments generally weighed about one gram.

Early results of the weight-gain measurements and visual examination of the oxidized test samples were as follows (Campbell et al. 1987): 1) The oxidation behavior of the spent fuel fragments differed markedly from the nonirradiated UO_2 pellets; for the spent fuel, the initial rates of weight gain were higher, the period required for powder to form was longer, and powder formation began at higher levels of weight gain. 2) Application of a high gamma field increased the weight gain of nonirradiated UO_2 pellets under a sealed cover gas system, but did not affect oxidation rates of spent fuel exposed to a continuous supply of fresh air. The increased oxidation rates

in static atmosphere therefore attributed to production of strongly oxidizing species by radiolytic decomposition of air. 3) Different moisture levels in the oxidizing atmosphere did not significantly affect the oxidation rates of spent fuel.

3.2 SAMPLING METHODS

Samples for microanalytical examination were removed from selected specimens that had been oxidized in the test ovens after various exposure periods. Initially, all of the test specimens consisted of fragments. As oxidation progressed, fine particles spalled from some of the specimens, forming a mixture of powder and fragments in the boats. Samples removed from the boats, therefore, consisted of two types: "powder" and "fragment" samples. After removal from a boat, each sample was encapsulated in a labeled vial and then transferred to a sample preparation hot cell. From these samples, subsamples were removed and prepared for examination. The identify, oxidation temperature and time, burnup, and weight gain of samples that have been examined are listed in the Results Section.

The number of samples that could be obtained and examined was limited by cost. Therefore, an effort was made to develop a sampling matrix that would produce a representative picture of the spent UO_2 oxidation behavior. Also, because of radiation work procedures and hot-cell scheduling considerations, oxidized UO_2 samples could be removed only during certain periods. Most sampling was done at two sampling intervals, after approximately 6,000 and 16,000 hours of oxidation.

Although each fuel sample removed from a specimen boat consisted of up to one gram of fragments or powder, microanalytical analysis was performed on much smaller quantities (subsamples) of material removed from these samples. The shielded SEM and SAM instruments are capable of examining an entire fuel fragment. However, sample preparation and handling were greatly simplified by working with small particles because of the radioactivity of the fuel (~400 R/h of gamma radiation per gram of fuel at contact). Small particles were chipped from selected locations on the fuel fragments using a carbide-tipped probe or vibratory tool; this method is illustrated in Figure 3.1a.

Particles chipped from the fragments varied in size from fine powder up to ~1-mm dia. However, particles selected for examination typically had a maximum edge dimension of 0.3 to 0.6 mm. Samples were then prepared from the chipped particles, or from powder particles, according to the methods described below.

Because of the method used to obtain sample particles from fuel fragments, the particles usually were removed from near the outer surface of a fragment. Fracture almost always occurred intergranularly, exposing grain facets, edges, and grain boundary triple points. These fresh, relatively clean grain surfaces were the focus of the SEM and AES examinations. To obtain representative data from the surface analysis techniques, it was important to know whether a particular surface was freshly fractured or whether it represented part of the original fragment surface. Fortunately, many particles contained both types of surfaces, and the surface types could be easily distinguished from each other. This is illustrated on the low magnification SEM micrograph of a fractured particle presented in Figure 3.1b. The brighter areas, mainly on the left and bottom side of the sample, are new fracture surfaces. The darker area that covers the right side of the sample is part of the original (as-oxidized) fragment surface. Generally, the as-oxidized surfaces were covered with particulate debris that obscured the underlying structures.

3.3 SAMPLE PREPARATION AND EXAMINATION

The following is a brief description of the methods used to prepare and analyze the radioactive fuel samples.

3.3.1 TEM

The process of sample preparation for TEM examination of spent fuel has been described by McCarthy and Thomas (1985). Briefly, a 0.05- to 0.3-μm particle, sampled as described above, was epoxied within a 3-mm O.D. metal annulus. This composite was mechanically ground and polished in a series of steps to a thickness below 15 μm. Final thinning was performed with an ion micromill; the sample was thinned by sputtering with an energetic argon ion beam. During ion milling, the samples were held in good thermal contact on a

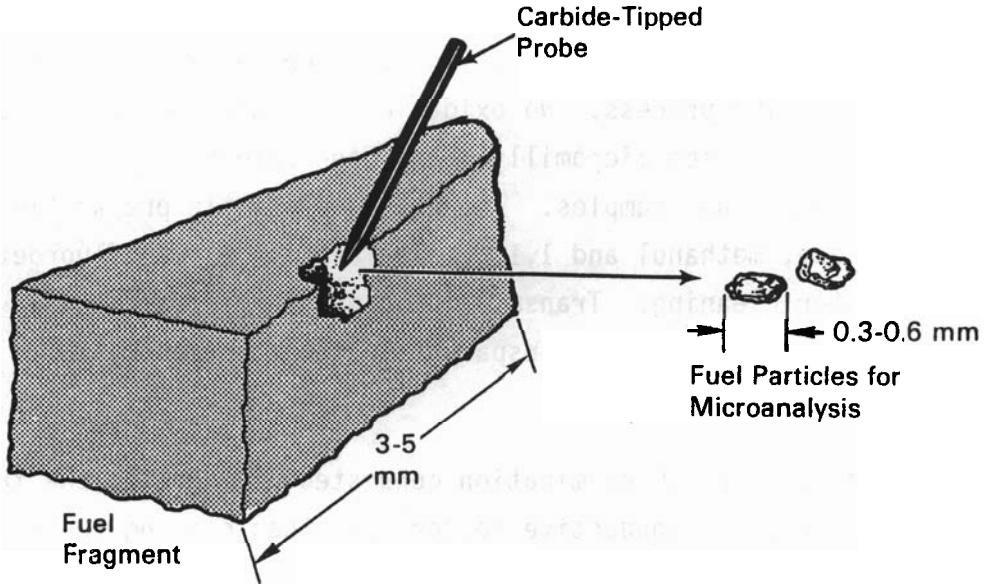

(a)

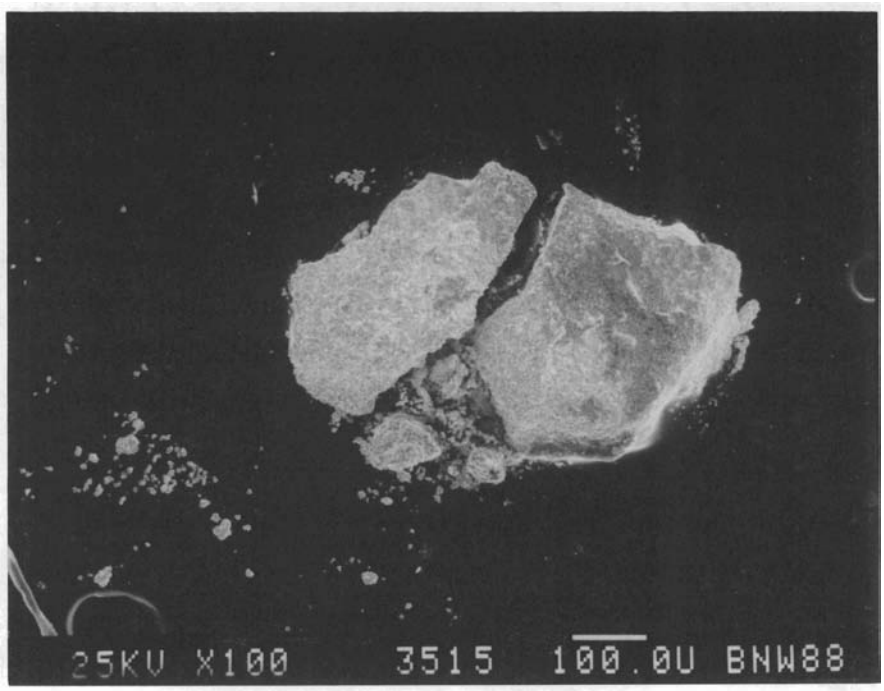

(b)

FIGURE 3.1. Spent Fuel Microsampling Method: a) Schematic Showing Method of Obtaining Fuel Particles for Analysis; b) Scanning Electron Micrograph of Sample Particle. Lighter regions are fresh fractures; darker regions are as-oxidized particle surfaces.

mounting block that was cooled with liquid nitrogen to minimize sample heating. Oxygen was excluded from the milling chamber to avoid oxidizing the samples during the milling process. No oxidation or other significant sample degradation resulting from ion micromilling has been detected by TEM examination of the spent fuel samples. The method of sample preparation used no water; only acetone, methanol and 1,1,2 trichloro-1,2,2 tetrafluoroethane solvents were used for cleaning. Transmission electron microscopy was performed on regions of the sample transparent to the electron beam.

3.3.2 SEM

Sample preparation for SEM examination consisted of mounting the fuel particles on an electrically conductive holder, and then coating the particles with a thin carbon film to prevent charge buildup during microscopic examination. The fuel particles were mounted on aluminum sample holders using double-sided adhesive tape. During mounting, the particles were gripped by their sides (with a fine tweezers) and pressed into the tape, taking care not to damage or deform the top surface. This procedure was performed with large pieces of fuel in a hot cell or with smaller pieces in a glovebox. Exposed surfaces of the particles and mounting tape were then coated with a 10- to 20-nm carbon layer to prevent charging during SEM examination. A typical particle mounted for SEM examination is shown in Figure 3.1b. Generally, two or three particles were prepared from each sample, and representative regions were photographed at the same magnifications to facilitate comparisons among different samples.

3.3.3 SAM

Sample preparation for SAM examination is similar to that for SEM examination, except that surface contamination must be prevented because of the sensitivity of Auger spectroscopy to monatomic layers. Application of a conductive coating to reduce charge buildup would interfere with the analysis. Fortunately, uncoated spent fuel, and in most cases the oxidized UO_2, was sufficiently conductive to avoid charging under the electron beam in the SAM. To securely hold the fuel particles and provide an electrical path close to the region of analysis, the particles were mounted by pressing them into a 0.13-mm thick indium foil using a clean glass slide. The particles

were intentionally fractured during this process to provide fresh surfaces for analysis. The mounting procedure was done in a glovebox. The foil was then mounted in a specially designed Auger sample holder. Indium foil rather than adhesive tape was used here because it was electrically conductive and compatible with the ultra-high vacuum of the SAM sample chamber.

Radioactivity of the spent fuel samples prevented the use of surface cleaning procedures normally used to prepare samples for SAM analysis. Normally, surface contamination due to handling and atmospheric exposure is removed by mechanically cleaning or ion beam sputtering the sample surface within the ultra-high vacuum analysis chamber of the instrument. In this work, in-situ cleaning within the analysis chamber was avoided to prevent radioactive contamination of the SAM. Some samples were sputter cleaned in an auxiliary chamber, then transferred under vacuum to the analysis chamber. When possible, the need for surface cleaning was minimized by selecting for analysis grain surfaces that were freshly created by fracture of the particle when pressing it into the indium foil.

Auger electron spectrometry was performed in an area-scan mode after identifying a region for analysis in the SEM imaging mode. Electron accelerating voltages varied from 3 to 20 keV and beam currents ranged from 5 to 200 nA. Different voltage/current combinations were required for each sample to prevent charging, apparently because of variations in the electrical conductivity of the samples. Auger surveys were done initially in the energy range of 30 to 2030 eV, then in the 30 to 630 eV range if no high energy peaks were observed. A minimum of 10 surveys were taken from each sample, unless charging prevented data acquisition. The collected data were stored in a computer and later analyzed.

To determine whether the SAM could be used to distinguish different uranium oxides, "standard" samples of nonirradiated UO_2 and U_3O_8, and non-oxidized spent fuel (Sample 86-37 from the Monticello BWR) were analyzed by Auger electron spectrometry. Auger spectra obtained from newly fractured samples of these materials were compared to observe intrinsic differences as well as any sample degradation effects caused by sputter-cleaning or electron beam exposure in the SAM. Spectra from the nonirradiated UO_2 and irradiated

UO_2 spent fuel were indistinguishable. Minor spectral variations caused by sample charging in the electron beam of the SAM, sputter cleaning, and electron bombardment induced damage was observed. However, easily recognizable and reproducible differences not caused by these extraneous effects were found in the uranium-peak fine-structure from UO_2 and U_3O_8. Differences in the uranium fine-structure from UO_2 and U_3O_8 are apparent in the spectra shown in Figure 3.2. The oxygen peak region for these phases was indistinguishable and therefore is not shown in Figure 3.2.

3.3.4 XRD

The powder diffractometer used in this study required a sample surface area of several cm^2. The high activity of the spent fuel prohibited the use of a bulk powder sample of this size. Instead, thin film samples were made by crushing milligram quantities of fuel and dispersing them in a collodion/solvent mixture, then applying the mixture to a glass slide and allowing the solvent to evaporate. The result was a relatively low-activity sample that could be safely handled with long tongs and examined in the diffractometer without significant instrumental interference from the sample radioactivity. Typical radiation fields about 2 in. from the XRD samples were 1 to 2 R/h.

The XRD spectra were analyzed by using standard computer-aided search/match methods involving automated comparisons of the experimental data with library spectra in the JCPDS database (JCPDS 1988). However, final phase identification was done by visually comparing selected library patterns with the experimental patterns. The "stick figure" plots given in Appendix A, Figure A.1, showing relative peak intensities as a function of diffraction angle (or d-spacing), were useful for overlay comparisons.

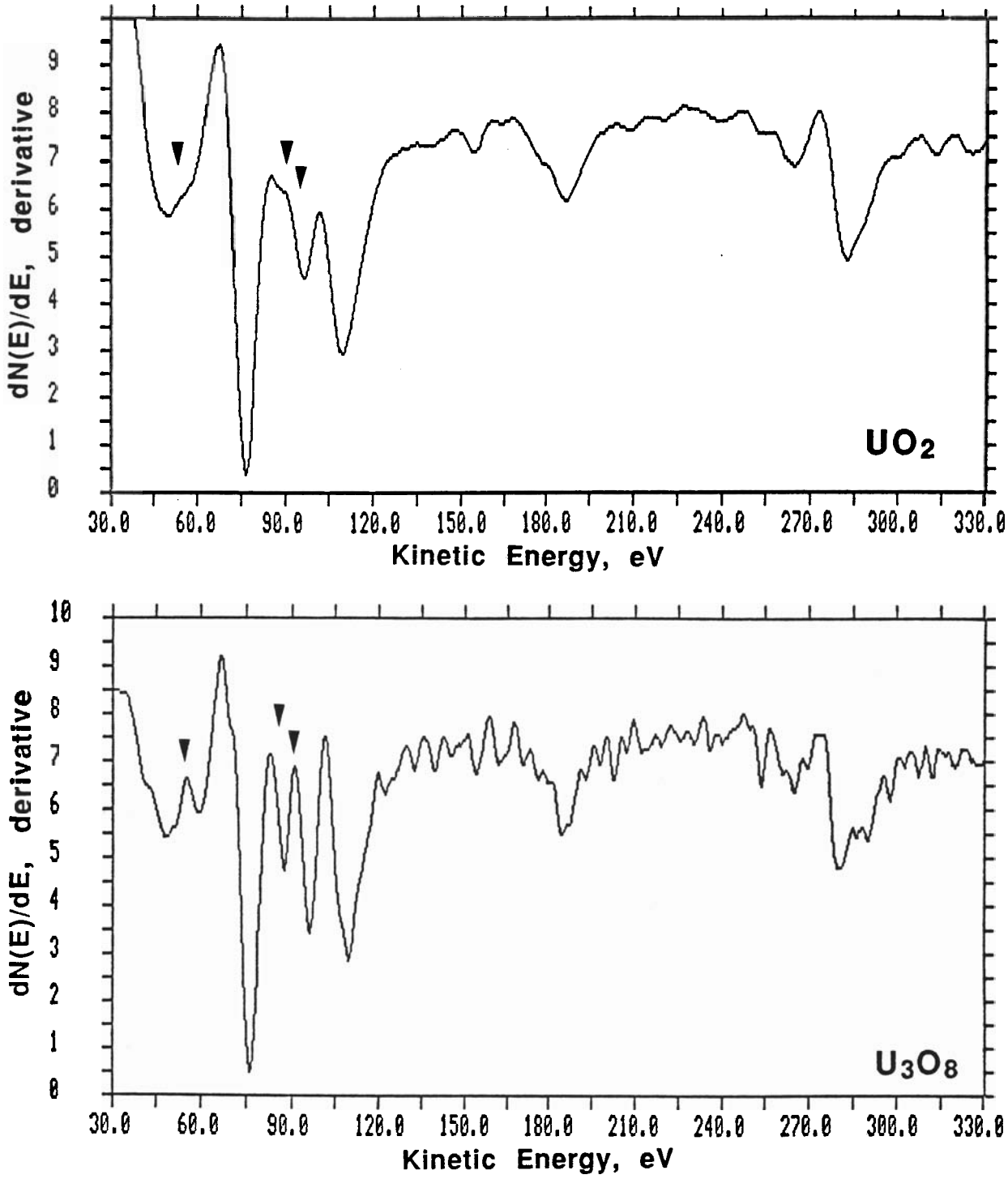

FIGURE 3.2. Auger Electron Spectra from Uranium Oxides, Showing Characteristic Differences in Uranium Peak Fine-Structure (arrowed): a) Nonoxidized UO_2 Spent Fuel (Monticello Reactor, 33 GWd/MTU burnup); b) Nonirradiated U_3O_8

4.0 MICROSTRUCTURAL CHARACTERIZATION RESULTS

Presented in this section are the results of the microstructural characterization of the oxidized samples. Twenty-seven different oxidized samples were examined by at least one of the four available analytical techniques (TEM, XRD, SEM, and SAM). As shown in Table 4.1, twenty of the samples were intact fragments, and the remaining six consisted of powder that spalled from fragments during the oxidation tests. The samples are listed in order of increasing weight gain and, hence, O/M. For each sample, Table 4.1 lists the reactor, fuel rod sample number, exposure (time) at oxidation temperature, and oxidation weight gain (%) when the sample was removed from its hot cell oven. The specimen I.D. number in Table 4.1 refers to the oven and boat number from which the sample was taken, and the suffix (p) after the sample I.D. number indicates a powder sample.

Four sets of samples were time-sequence pairs, i.e., samples removed from the same specimen after two different exposure times. Time-sequence pairs included 86-24 and 87-169 (Quad Cities-1, 135°C), 86-26a and 87-164 (Monticello, 135°C), 86-33 and 87-174 (H.B. Robinson, 170°C), and powder samples 87-01 and 88-01 (Quad Cities-1, 230°C). Three additional sample pairs were powder and fragment samples from the same specimens. These samples, all from Quad Cities-1 BWR fuel, included 86-25 and 87-03 (135°C), 87-168 and 86-38 (150°C), and 86-29, 87-01, and 88-01 oxidized at 230°C.

Results of the XRD, TEM and SEM of each sample are summarized in Table 4.2. SAM results were not included in Table 4.2 because none of the oxidized samples showed definitive differences in the SAM; all gave similar spectra closely resembling the nonirradiated U_3O_8 spectrum shown in Figure 3.2. Also listed in Table 4.2 are the O/M ratios based sample weight-gain measurements. Because of interest in the use of time-to-powder data as an indicator of U_3O_8 formation (Campbell 1987), analysis results from examination of the six powder specimens are presented separately from the fragment data.

TABLE 4.1. Samples Analyzed by XRD, TEM, SAM or SEM, Ordered by Increasing Weight Gain

Sample I.D. No.	Specimen I.D.	Source Reactor (Rod)	Oxidation Temp.,°C	Burnup, MWd/kgM	Exposure Time, hrs.	Weight Gain, %	TEM	SEM	SAM	XRD
86-37	86-21	Monticello	none	33.3	N/A (0A08-4)	N/A	X	X		
86-25	10B-10	Quad Cities-1	135	24.2	6763 (1C02-4)	0.022	X	X		
86-24	10B-6	Quad Cities-1	135	7.9	6763 (1A01-2)	0.043		X		
87-03 (p)	10B-10	Quad Cities-1	135	24.2	8754 (1C02-4)	0.044		X	X	X
87-169	10B-6	Quad Cities-1	135	7.9	14587 (1A01-2)	0.087		X	X	X
86-26a	6B-11	Monticello	135	34.4	7468 (0A08-4)	0.097	X			
86-32	10B-3	H.B. Robinson	135	27.6	6763 (HBRG9T)	0.102	X			
87-164	6B-11	Monticello	135	34.4	13177 (0A08-4)	0.100	X	X		X
87-166	2B-9	Monticello	150	21.4	14180 (OA03-4)	0.494				X
87-165	2B-3	Quad Cities-1	150	7.8	14180 (1B02-4)	0.71		X	X	
87-163	7B-5	H.B. Robinson	150	28.4	13888 (HBRG9T)	0.8	X	X	X	X
86-38 (p)	1B-4	Quad Cities-1	150	7.7	7344 (1B02-4)	0.88		X	X	X
87-162	7B-11	H.B. Robinson	150	9.9	13888 (HBRG9T)	1.01	X			
87-168	1B-4	Quad Cities-1	150	7.7	1444 (1B02-4)	1.33		X	X	X
87-175	11B-7	Monticello	170	33.7	16685 (5D18-3)	1.76				X

TABLE 4.1. (contd)

Sample I.D. No.	Specimen I.D.	Source Reactor (Rod)	Oxidation Temp.,°C	Burnup MWd/kgM	Exposure Time, hrs.	Weight Gain, %	TEM	SEM	SAM	XRD
86-33	11B-4	H.B. Robinson	170	27.6	7633 (HBRG9T)	2.21	X	X		X
86-28	4B-7	Quad Cities-1	190	23.5	7171 (1A01-1)	2.50	X	X		X
87-172	11B-8	Quad Cities-1	170	8.0	16685 (1A01-2)	2.58		X		X
86-27a	4B-4	Quad Cities-1	190	7.9	7171 (1B02-4)	3.02	X	X	X	X
87-174	11B-4	H.B.Robinson	170	27.6	16685 (HBRG9T)	3.25		X		
86-30	12B-9	Quad Cities-1	230	24.2	4617 (1C02-4)	>4.34	X			
87-02 (p)	12B-9	Quad Cities-1	230	24.2	5430 (1C02-4)	4.34		X		X
86-34	12B-3	H.B.Robinson	230	26.8	4607 (HBRG9T)	4.76	X			
86-29	12B-6	Quad Cities-1	230	8.0	4607 (1A01-2)	5.31		X	X	X
87-01 (p)	12B-6	Quad Cities-1	230	8.0	5430 (1A01-2)	5.48				X
88-01 (p)	12B-6	Quad Cities-1	230	8.0	13597 (1A01-2)	7.13				X
88-02 (p)	12B-12	Nonirradiated	230	0.0	13597	10.59		X		X

(p): Powder samples. Other samples were obtained from fragments.

ID = Identification number.

TABLE 4.2. Summary of XRD, TEM and SEM Results for Oxidized Spent Fuel Samples

Sample I.D. No.	Oxidation Temp., °C	Burnup, MWd/kgM	Exposure Time, h	Average O/M	Results
86-37	none	33.3	N/A	2.000	TEM: UO_2 grains with 10-50 nm fission product particles on grain boundaries, smaller particles in UO_2 grains SEM: no detectable structure on grain boundaries; no cracks
86-25	135	24.2	6763	2.004	TEM: Similar to non-oxidized fuel. Grain boundary cracking, but no U_4O_9 observed. SEM: Clean fracture surfaces, no detectable oxide scale; tightly bound grains.
86-24	135	7.9	6763	2.007	SEM: Little visible oxide scale; intergranular fracture, few cracked grain boundaries.
87-03(p)	135	24.2	8754	2.007	XRD: ~70% UO_2, 30% U_4O_9. SEM: Powder not visibly different from larger parent particles (sample 85-25).
87-169	135	7.9	14587	2.015	XRD: ~100% UO_2, minor U_4O_9. SEM: Clean fracture surfaces; trace oxide scale at grain boundary edges.
86-26a	135	34.4	7468	2.016	TEM: U_4O_9 along grain boundaries. Unaltered UO_2 grain centers. Grain boundary cracking.
86-32	135	27.6	6763	2.017	TEM: U_4O_9 along grain boundaries. Unaltered UO_2 grain centers. Grain boundary cracking.
87-164	135	34.4	13177	>2.017	XRD: ~85% UO_2, 15% U_4O_9. TEM: Extensive U_4O_9 formation along grain boundaries. Similar to more highly oxidized (O/M = 2.14) samples. SEM: Thin nodular oxide scale at grain edges matches U_4O_9 seen by TEM
87-166	150	21.4	14180	2.08	XRD: ~70% UO_2, 30% U_4O_9.
87-165	150	7.8	14180	2.12	SEM: Thin oxide scale on intergranular fracture surfaces; no thick scale as on 87-168.

TABLE 4.2. (contd)

Sample I.D. No.	Oxidation Temp., °C	Burnup, MWd/kgM	Exposure Time, h	Average O/M	Results
87-163	150	28.4	13888	2.14	XRD: ~70% UO_2, 30% U_4O_9. TEM: Extensive U_4O_9 formation along grain boundaries. Dense UO_2/U_4O_9 grains with few microcracks. SEM: Thin oxide scale on intergranular fracture surfaces; tightly bound grains.
86-38 (p)	150	7.7	7217	2.15	XRD: ~50:50 UO_2:U_4O_9; 15% α-U_3O_7. SEM: Powder particles are multigrain fragments, coated with thick nodular scale.
87-162	150	9.9	13888	2.17	XRD: ~100% U_4O_9. TEM: Dense U_4O_9 with few microcracks. Irregular grain boundaries with unidentified fill material.
87-168	150	7.7	14447	2.22	XRD: ~55% UO_2, 45% U_4O_9. SEM: Thick oxide scale on grain boundary surfaces.
87-175	170	33.7	16685	2.30	XRD: ~45% UO_2, 55% U_4O_9.
86-33	170	27.6	7633	2.37	XRD: ~25% UO_2, 75% U_4O_9. TEM: Extensively microcracked U_4O_9 with scattered fine grains of U_3O_8. Complex diffraction patterns. SEM: Thin smooth scale, tightly bound grains on fracture surfaces.
86-28	190	23.5	7171	2.42	XRD: ~100% U_4O_9. TEM: Highly altered structure with extensively microcracked U_4O_9 grains; fine-grained phase (U_3O_8) and small bubbles along microcracks. Complex diffraction patterns. SEM: Nodular scale on grain boundary fracture surfaces.
87-172	170	8.0	16685	2.44	XRD: U_4O_9/U_3O_7 mixture with trace U_3O_8. SEM: Thin nodular scale and intact grain boundaries on fracture surfaces; thick scale, loose grains near external surface.

TABLE 4.2. (contd)

Sample I.D. No.	Oxidation Temp., °C	Burnup, MWd/kgM	Exposure Time, h	Average O/M	Results
86-27a	190	7.9	7171	2.50	XRD: All α-U_3O_7. No U_3O_8. TEM: Dense ordered phase in prior UO_2 grains. (May be U_3O_7). Grains are cut by veins containing unidentified fine-grained polycrystalline phase. SEM: Moderately thick nodular scale on intergranular fracture surfaces; Lines on grain surfaces match veins seen by TEM.
87-174	170	27.6	16685	2.55	SEM: Thick oxide scale; some microcracks. XRD: ~100% U_4O_9.
86-30	230	24.2	4607	>2.73	TEM: Highly altered structure with network of microcracked veins containing fine-grained U_3O_8. Diffraction indicates phases are mostly fluorite structure type.
87-02(p)	230	24.2	5430	>2.73	XRD: Mostly U_4O_9 plus minor U_3O_8. Trace dehydrated schoepite ($UO_3 \cdot H_2O$). SEM: Powder particles are clusters of loosely connected grains. Grains show highly altered structure with intersecting veins
86-34	230	26.8	4607	2.80	TEM: Highly altered structure with microcracks and veins filled with fine-grained U_3O_8. Complex mixture of U_3O_8 and fluorite-type structures.
86-29	230	8.0	4607	2.89	XRD: Mostly U_3O_8 and U_4O_9 with shoepite and dehydrated schoepite. Estimate ~60% U_3O_8. SEM: Particles consist of loosely bound grain clusters; nodular, textured oxide scale covers each grain.
87-01(p)	230	8.0	5430	2.93	XRD: Mostly U_3O_8 with some U_4O_9 dehydrated schoepite and schoepite. Estimate ~60% U_3O_8.
88-01(p)	230	8.0	13597	3.20	XRD: U_3O_8 , dehydrated schoepite and and schoepite, plus minor U_4O_9.
88-02(p)	230	0.0	13597	3.78	XRD: Schoepite, unidentified phase (probably a hydrate), U_3O_8 and dehydrated schoepite. No UO_2-structure phase. SEM: Thick, flowery oxide scale covering each grain; particles consist of loosely bound grain clusters.

(p): Powder samples. Other samples were obtained from fragments.

The results in this section are organized primarily with respect to the sequence of phase development found with increasing test temperatures and O/M ratios. Because of the rapid acceleration in oxidation rates with increasing test temperature, and the limited sampling time intervals, a given range of O/Ms corresponded to usually only one test temperature. O/M ranges in the samples used for analysis overlapped only at test temperatures 170 and 190°C. For the oxidation weight-gain data, see Campbell et al. (1987).

4.1 NONOXIDIZED SPENT FUEL

Spent fuels from the Monticello BWR and the H. B. Robinson PWR were examined by TEM in the as-irradiated (nonoxidized) condition. Detailed examination of H. B. Robinson spent fuel and other moderate burnup, low gas release PWR and BWR fuels was also reported previously (Guenther et al. 1988; Thomas and Guenther 1989). The microstructures of the as-irradiated LWR fuels generally consisted of equiaxed UO_2 grains containing most fission products in solution or as finely dispersed 1- to 10-nm-dia particles. Larger particles found mostly along grain boundaries were ϵ-ruthenium phase--a solid solution alloy of molybdenum, ruthenium, technetium, palladium, and rhodium. The only other phase observed in these fuels was xenon/krypton, either as gas bubbles or as condensed-phase particles (near the fuel rod centers). All other fission products in the low-release fuels apparently remained in solution in the UO_2 matrix.

Grain boundaries in the as-irradiated spent fuels were generally coated with small (<10-nm dia) fission gas bubbles and solid particles as shown in Figure 4.1. Similar concentrations of small bubbles were found along the grain boundaries in randomly selected samples. The sizes and spacings of the bubbles generally increased toward the high-temperature centers of fuel pellets (Thomas and Guenther 1989). The tendency of spent fuel to oxidize preferentially along grain boundaries has been attributed to these bubbles (Thomas, McCarthy and Gilbert 1986a,b; Thomas, Einziger and Woodley 1989). The closely spaced bubbles are believed to provide short-circuit paths for oxygen to penetrate along the grain boundaries.

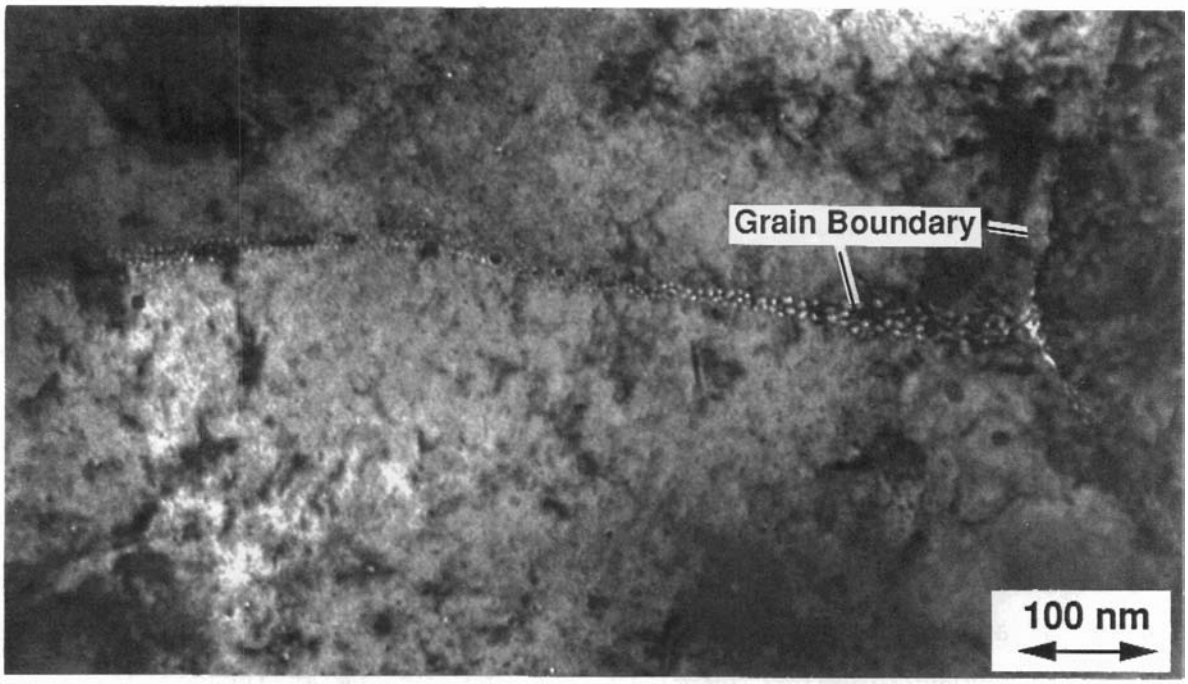

FIGURE 4.1. Fission Gas Bubbles and Solid Particles on Grain Boundary in Nonoxidized (as-irradiated) H. B. Robinson Spent Fuel; TEM brightfield micrograph.

Only UO_2 was detected in the nonoxidized fuels by x-ray diffractometry. The concentrations of the fission product phases or any other uranium oxides were below the minimum detection limits for XRD (typically about 1 wt.%).

SEM examinations of surfaces obtained by fracturing the nonoxidized fuel samples showed equiaxed UO_2 grains with few bubbles or second-phase particles visible on the grain boundaries. Slow crushing tended to fracture the spent fuel preferentially along grain boundaries, and most grains in the as-irradiated fuel appeared well-bonded (uncracked) along the boundaries.

4.2 OXIDIZED FUEL FRAGMENTS

In this section, the results of microstructural examination of the oxidized fuel fragment samples are presented.

4.2.1 Low-Temperature Oxidation: O/Ms from 2.004 to 2.55

The overall results summarized in Table 4.2 show a general progression of phase development through U_4O_9 to U_3O_8, and eventually to uranium hydrates, with increasing O/M ratios. In a few samples, α-U_3O_7 also appeared. **The order of phase appearance with increasing O/M generally** followed the sequence sketched earlier in Figure 3.3.

Progressive development of the fluorite-structure phases with increasing O/M to 2.55 is illustrated by the x-ray diffractograms in Figure 4.2. The x-ray spectra in Figure 4.2 are from mixtures of UO_2, U_4O_9, and U_3O_7. Diffraction angles from 46 to 60° 2θ allow observation of the characteristic peak shifts and peak splitting that distinguish these fluorite-structure phases by XRD. The UO_2 phase produced narrow peaks near 46.9, 55.6, and 58.3° 2θ. Formation of U_4O_9 was marked by the appearance of broadened peaks on the high-angle sides of the UO_2 peaks. **With increasing O/M, the U_4O_9 peak** intensities increased relative to the UO_2 intensities. The U_4O_9 lattice parameter (referred to the UO_2 unit cell), measured from six samples, averaged 0.5448 ± 0.0004 nm--slightly larger than the lattice parameter given on JCPDS card No. 20-1344) for U_4O_9. **The lattice parameter of the UO_2** innonoxidized and partially oxidized fuel samples was 0.5475 ± 0.0003 nm, in agreement with JCPDS card No. 5-550.

At O/Ms below 2.55, U_3O_8 was undetectable or, in sample 87-172 at O/M = 2.44, barely detectable by XRD: A broad U_3O_8 peak (actually several closely spaced peaks) would appear near 52° 2θ in Figure 4.2--well separated from the fluorite-structure peaks--if U_3O_8 were present at a significant concentration.

Peak splitting, characteristic of U_3O_7, appeared in two samples, 87-172 and 86-27A, oxidized to O/Ms of 2.44 and 2.50 at 170 and 190°C, respectively. The U_3O_7 in sample 86-27A approximately matched α-U_3O_7 (JCPDS card No. 15-4); that in sample 87-172 did not match any U_3O_7 phases in the JCPDS database (see x-ray patterns for these phases in Figure A.2 of Appendix A). **Apparent** variability in forming U_3O_7 or U_4O_9 at O/Ms from 2.42 to 2.55 might be caused by sample inhomogeneities or could be a fuel burnup effect. **Samples in this** O/M range that formed U_3O_7 were from low burnup (8 MWd/kgM) Quad Cities

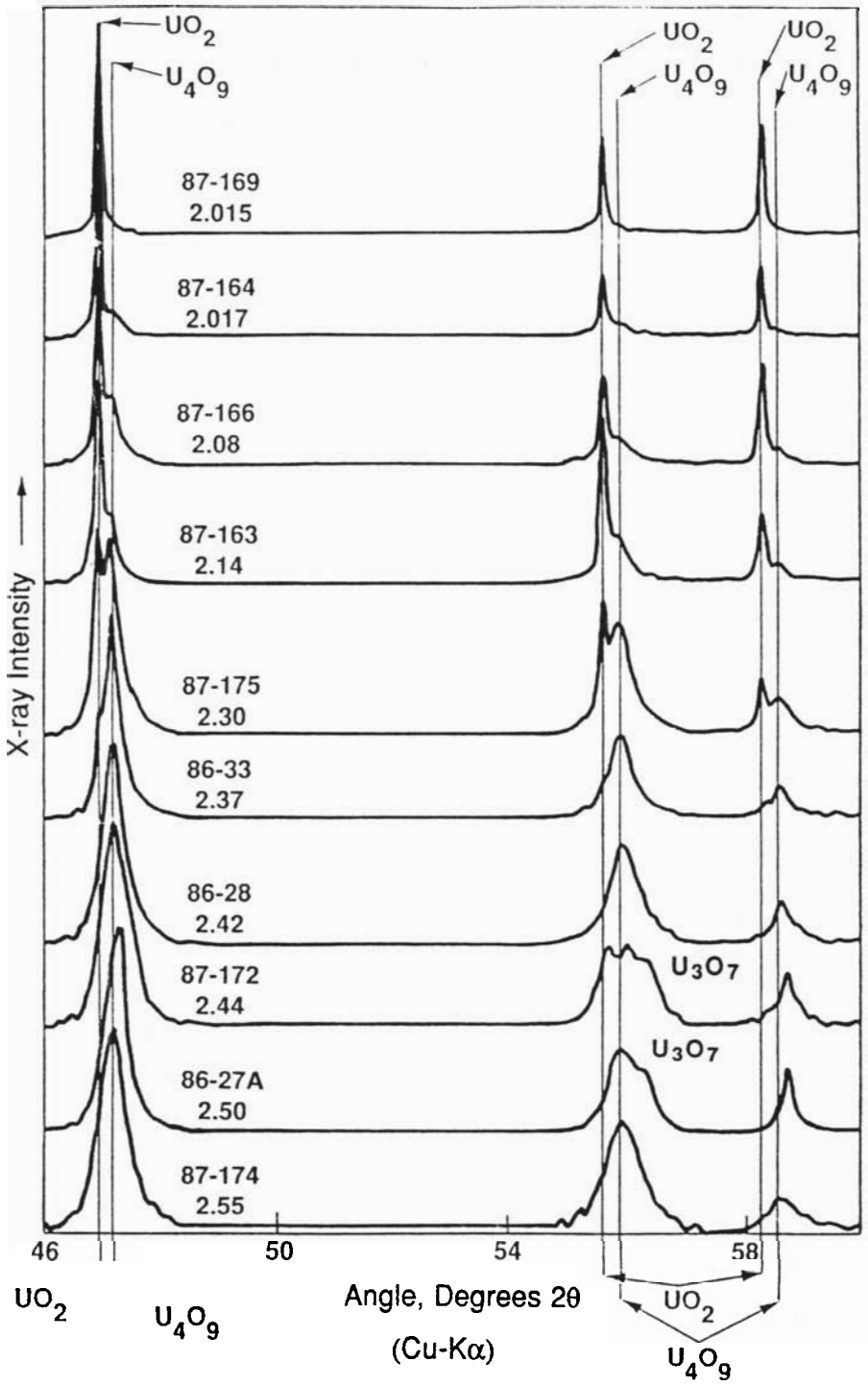

FIGURE 4.2. X-Ray Diffractograms from Oxidized Fuel Fragments, Showing Conversion of UO_2 to U_4O_9 and U_3O_7 at Average O/Ms to 2.55. Sample ID Numbers and Average O/M Ratios Determined from Oxidation Weight Gains are Shown in Figure.

fuel; corresponding samples of higher burnup (24 MWd/kgM) Quad-Cities fuel contained 100% U_4O_9 at similar oxidation times and temperatures.

In the following, the microstructures and diffraction characteristics associated with the various phases indicated by the XRD analysis are described.

4.2.2 UO_2-U_4O_9 Microstructures: O/M from 2.00 to 2.30

Microstructural examination of the oxidized samples by TEM and SEM shows how the U_4O_9 formed in UO_2 spent fuel. The initial stage of oxidation, observed in samples with average O/Ms to about 2.2, consisted of relatively rapid U_4O_9 formation along grain boundaries and slower growth of the U_4O_9 into the UO_2 grains. The U_4O_9 has the same crystallographic orientation as the parent UO_2 phase and grows by sweeping a smooth, coherent U_4O_9/UO_2 interface from the grain boundaries into the grain interiors (Thomas, Einziger and Woodley 1989). In the TEM, U_4O_9 can be recognized by effects of enhanced electron scattering from partially ordered excess oxygen in its crystal lattice. The U_4O_9 appears in brightfield transmission electron micrographs as dark bands of (strongly scattering) material, as shown in Figure 4.3a. Microstructural features visible within the nonoxidized UO_2 regions in Figure 4.3a include many small precipitate particles and gas bubbles produced during burnup.

The enhanced scattering from U_4O_9 appears in electron diffraction patterns as bands and streaks of diffuse-scattered intensity at non-Bragg positions. Shown in Figures 4.3b and 4.3c are selected-area electron diffraction patterns from UO_2 and U_4O_9 regions indicated by circles on the transmission micrograph. The adjacent UO_2 and U_4O_9 regions have the same crystallographic orientation across the phase interface and produce the same fundamental reflections, but the extra, diffuse scattering reflections in Figure 4.3c are characteristic of γ-U_4O_9. All U_4O_9 found in irradiated fuel after oxidation at 150 to 230°C was the partially disordered γ-U_4O_9 phase.

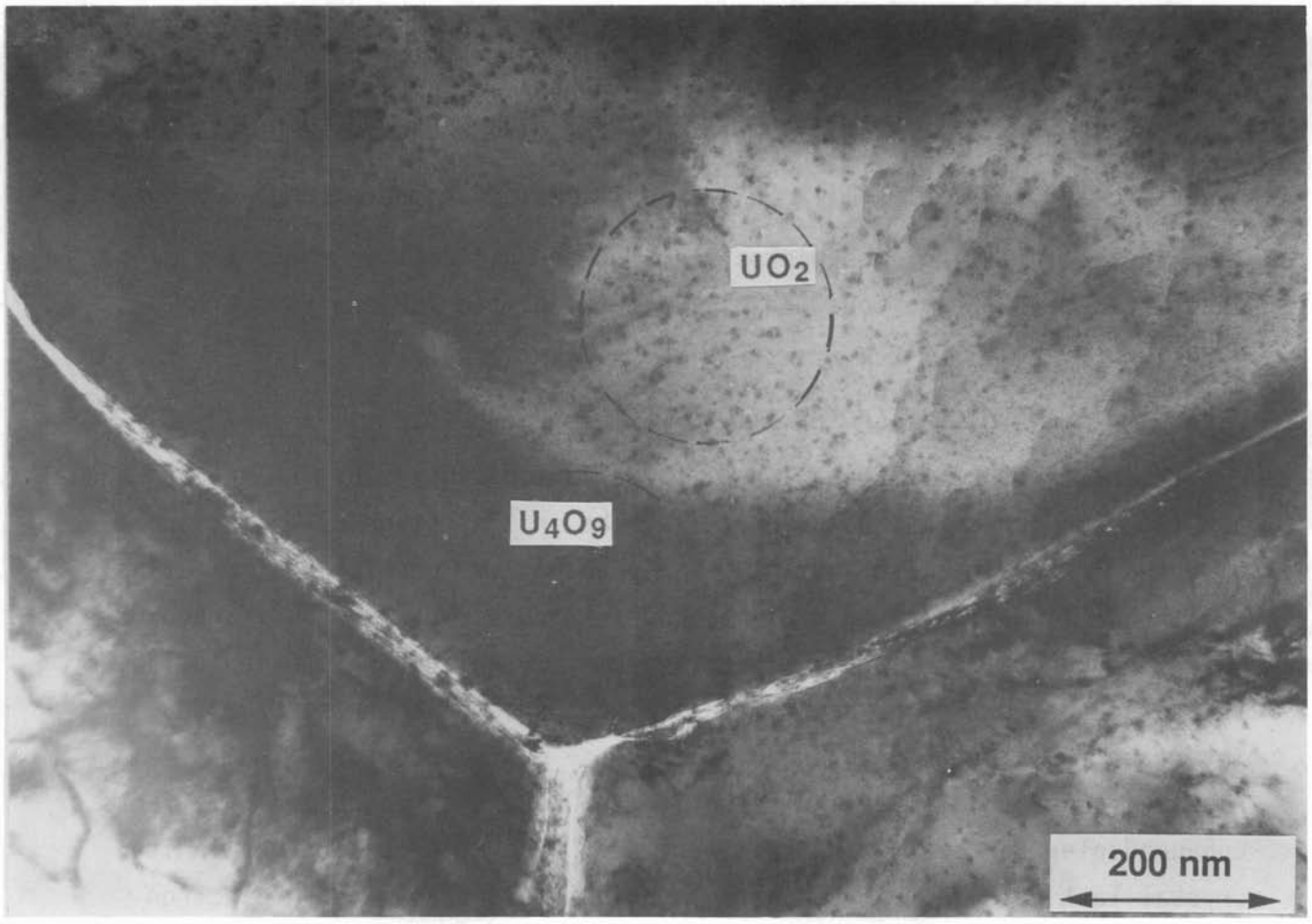

(a)

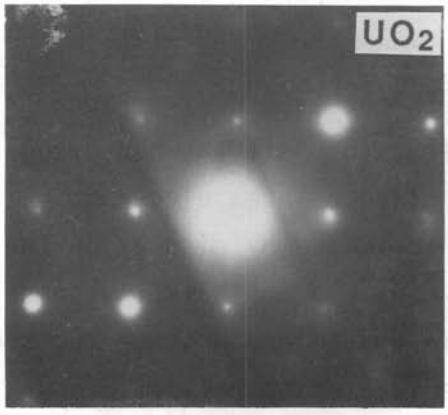

(b)

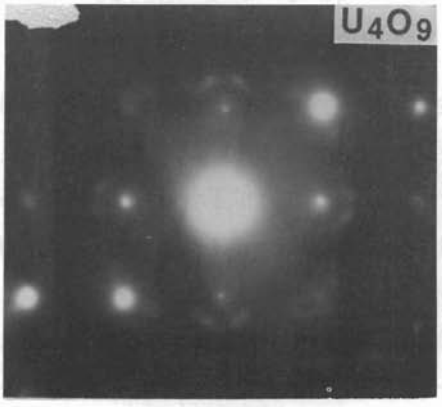

(c)

FIGURE 4.3. U_4O_9 Formation Along Grain Boundaries in Oxidized Monticello BWR Fuel (135°C oxidation; average O/M = 2.016): a) Transmission Electron Micrograph; b) Selected-Area Diffraction Pattern from UO_2 Region; c) Selected-Area Diffraction Pattern from U_4O_9, Showing Extra, Diffuse-Scattering Reflections

Formation of U_4O_9 along prior-UO_2 grain boundaries caused the boundaries to crack open along the grain edges. The grain boundary cracks are apparent in Figure 4.3a. The U_4O_9 grew initially from the grain edges, which are sites of preferential gas bubble formation in as-irradiated fuel, and spread along the grain faces as well as into the grain interiors. In the SEM, thin bands of nodular oxide marked the extent of U_4O_9 formation along grain faces exposed by intergranular cleavage. The SEM micrographs in Figure 4.4 show the U_4O_9 development along the boundaries. At O/M = 2.007 (Figure 4.4b), the oxidation is hardly detectable by SEM; and at O/M = 2.017 (Figure 4.4c), the oxidized regions correspond to those seen extending into the UO_2 grains in Figure 4.3a.

At O/Ms of about 2.1 to 2.2, a few microcracks appeared within otherwise dense U_4O_9 regions, and U_4O_9 replaced most of the UO_2. Thick nodular oxide developed on the grain boundaries, as shown in SEM micrograph Figure 4.5a.

4.2.3 U_4O_9 + U_3O_8 Microstructures: O/Ms from 2.30 to 2.55

Except for one fragment sample in which XRD analysis showed only α-U_3O_7, XRD analyses of the samples with O/Ms between 2.30 and 2.55 indicated mostly the presence of U_4O_9 and only a trace of U_3O_8. TEM examination of samples 86-33 and 86-28, having average O/Ms of 2.37 and 2.42, respectively, showed that the U_4O_9 grains were extensively microcracked and contained a fine-grained polycrystalline phase along microcrack networks. Electron diffraction identified the 20- to 50-nm-diameter particles as α-U_3O_8.

Transmission electron micrographs in Figure 4.6 show these highly altered structures in Sample 86-28. A network of closely spaced microcracks is shown near the center of a prior-UO_2 grain in Figure 4.6a, and selectively imaged U_3O_8 particles in a similar area of the same sample are shown in Figure 4.6b. Another structure observed near grain boundaries in the same sample consisted of small bubbles along the microcrack networks; this structure is shown in Figure 4.6c. The bubbles are not typical of as-irradiated fuel microstructures and are clearly associated with the oxidation-induced microcracks. These bubbles may result from oxidation-induced release of fission gases.

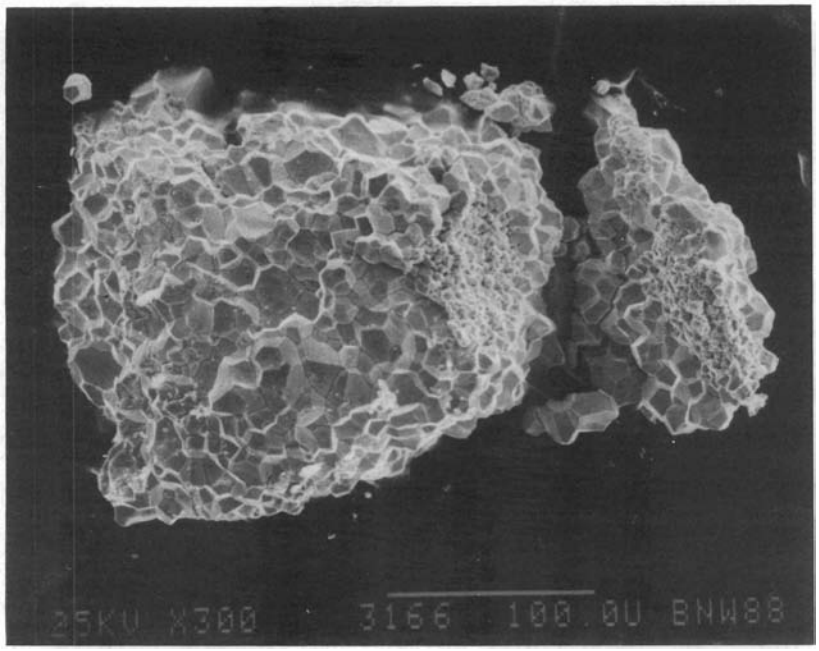

(a)

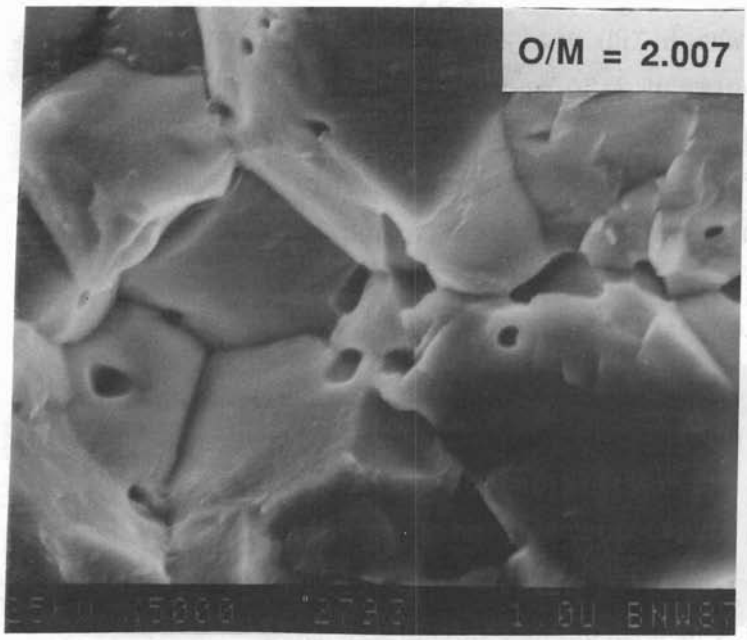

(b)

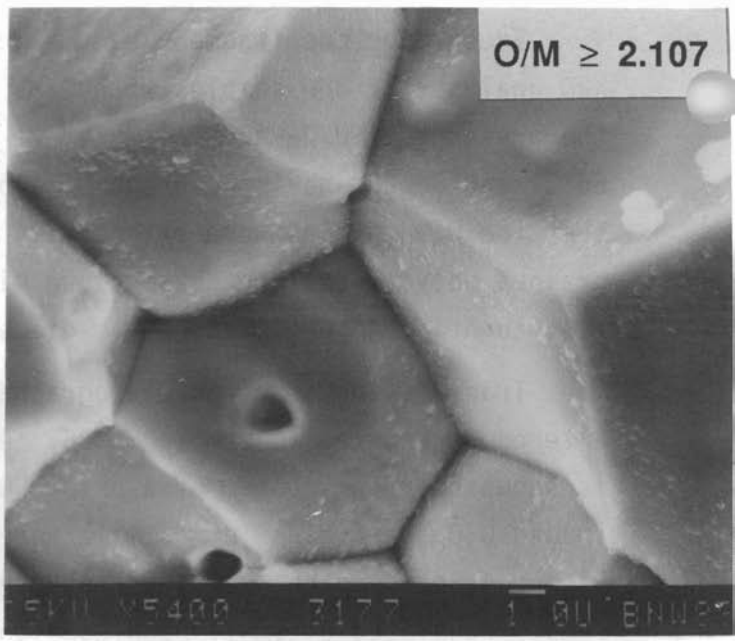

(c)

FIGURE 4.4. Fracture Surfaces of Spent Fuel Oxidized at 135°C; Scanning Electron Micrographs: a) Overall View of Oxidized Particles, Sample No. 87-164; b) Sample 86-24, 6700 h, Oxidation Hardly Detectable; c) Sample 87-164, 13,177 h, Showing Oxidation Along Grain Edges

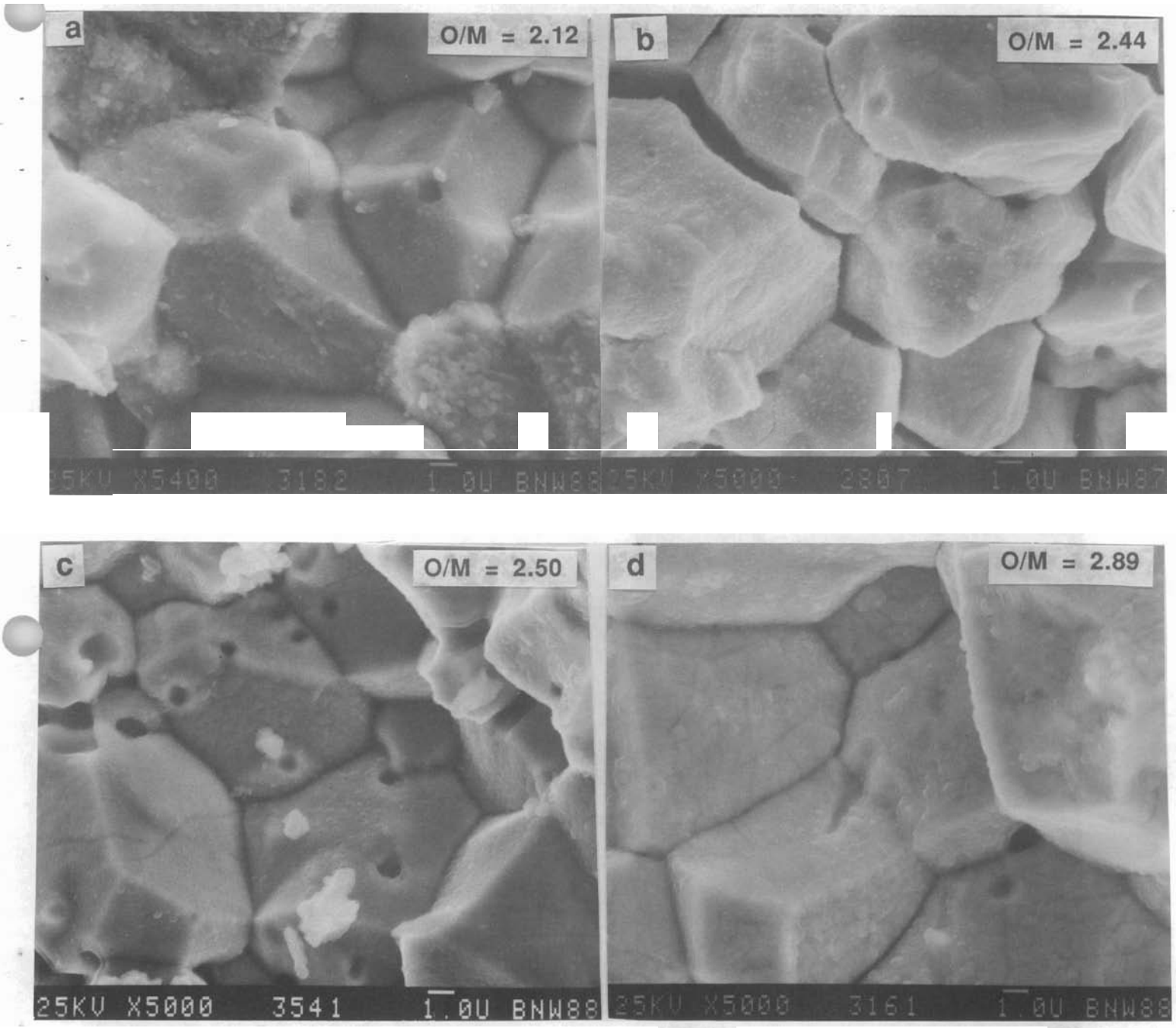

FIGURE 4.5. SEM Micrographs of Spent Fuel Oxidized at Different Temperatures: a) Sample 87-165, 14,180 h at 150°C, O/M = 2.12; b) Sample 87-172, 16,685 h at 170°C, O/M = 2.44; c) Sample 87-27A, 1,171h at 190°C, O/M = 2.70; d) Sample 86-29, 4,607 h at 230°C, O/M = 2.89

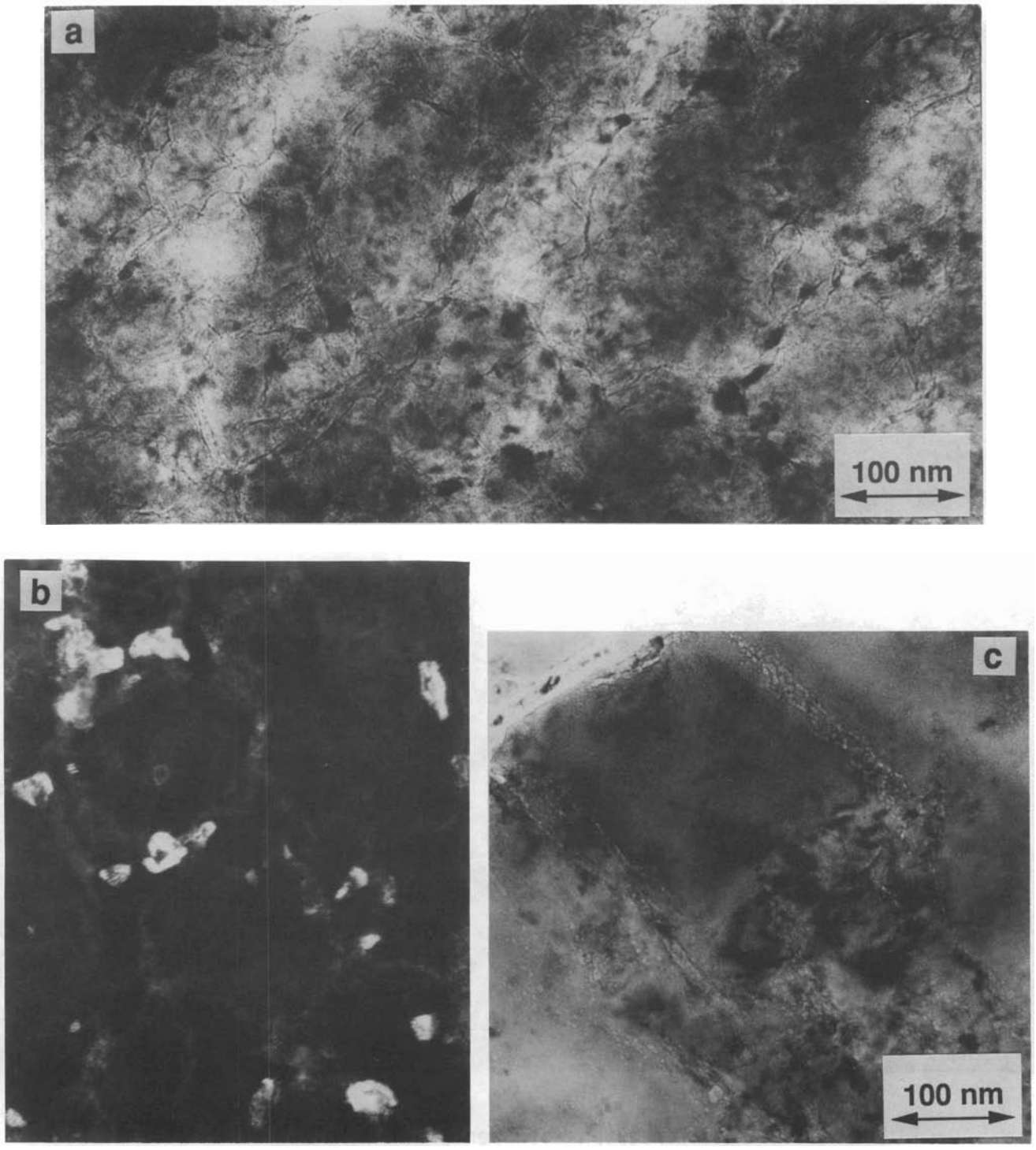

FIGURE 4.6. Oxidation Microstructures in Quad Cities BWR Fuel (O/M = 2.43, 190°C test): a) Microcracks and Fine-Grained U_3O_8 in U_4O_9 Matrix; b) Selectively Imaged U_3O_8 Grains; c) Small Bubbles Along Microcracks Near Grain Boundary

SEM observation of intergranular fracture surfaces in Sample 87-172, with O/M = 2.44 (Figure 4.5b) showed thick nodular oxide scale on the boundaries, and a structure of intersecting lines ("veins") on grain surfaces in the SEM.

According to the XRD results, Sample 87-174 consisted of 100% U_4O_9 with no detectable U_3O_8 at O/M = 2.55.

4.2.4 U_3O_7 Microstructure: O/M = 2.50

X-ray diffraction analysis of sample 86-27A (190°C test temperature) indicated 100% α-U_3O_7 at O/M = 2.50. For this sample, fine-scale microcracking was absent, but the oxidized material contained relatively wide "veins" of an unidentified fine-grained polycrystalline phase (Figure 4.7a). Regions between the veins contained large grained monophase material assumed to be the U_3O_7. Electron diffraction patterns from the "U_3O_7" phase produced superlattice reflections, and a TEM darkfield image (Figure 4.7b) formed with these reflections showed what appeared to be very small domains of the ordered material. An SEM micrograph of this sample (Figure 4.5c) shows the veins and thick oxide on the intergranular (grain boundary) fracture surfaces.

4.2.5 U_3O_8 Formation: O/M = 2.73 to 3.2

U_3O_8 formation in the oxidized fuel samples increased at the expense of U_4O_9 or U_3O_7 at O/Ms from 2.7 to 3.2, and schoepite (uranium trioxide dihydrate) appeared. An x-ray diffractogram shown in Figure 4.8, from Sample 86-29 at O/M = 2.89, indicated a mixture of α-U_3O_8, U_4O_9, dehydrated schoepite, and schoepite. Also shown for comparison in Figure 4.8 are an experimentally obtained diffraction pattern from a U_3O_8 "standard," and appropriate JCPDS reference patterns for the α-U_3O_8, U_4O_9, and schoepite. A corresponding SEM micrograph of Sample 86-29 (Figure 4.5d) shows loosely connected prior-UO_2 grains with nodular, textured oxide on the surfaces.

The diffraction pattern shown for comparison in Figure 4.8b is from a U_3O_8 "standard" that was produced by heating nonirradiated UO_2 in air at 400°C for about 20 h. From the oxidation weight gain, an average O/M of 2.548 was determined for this sample. The best reference pattern match to

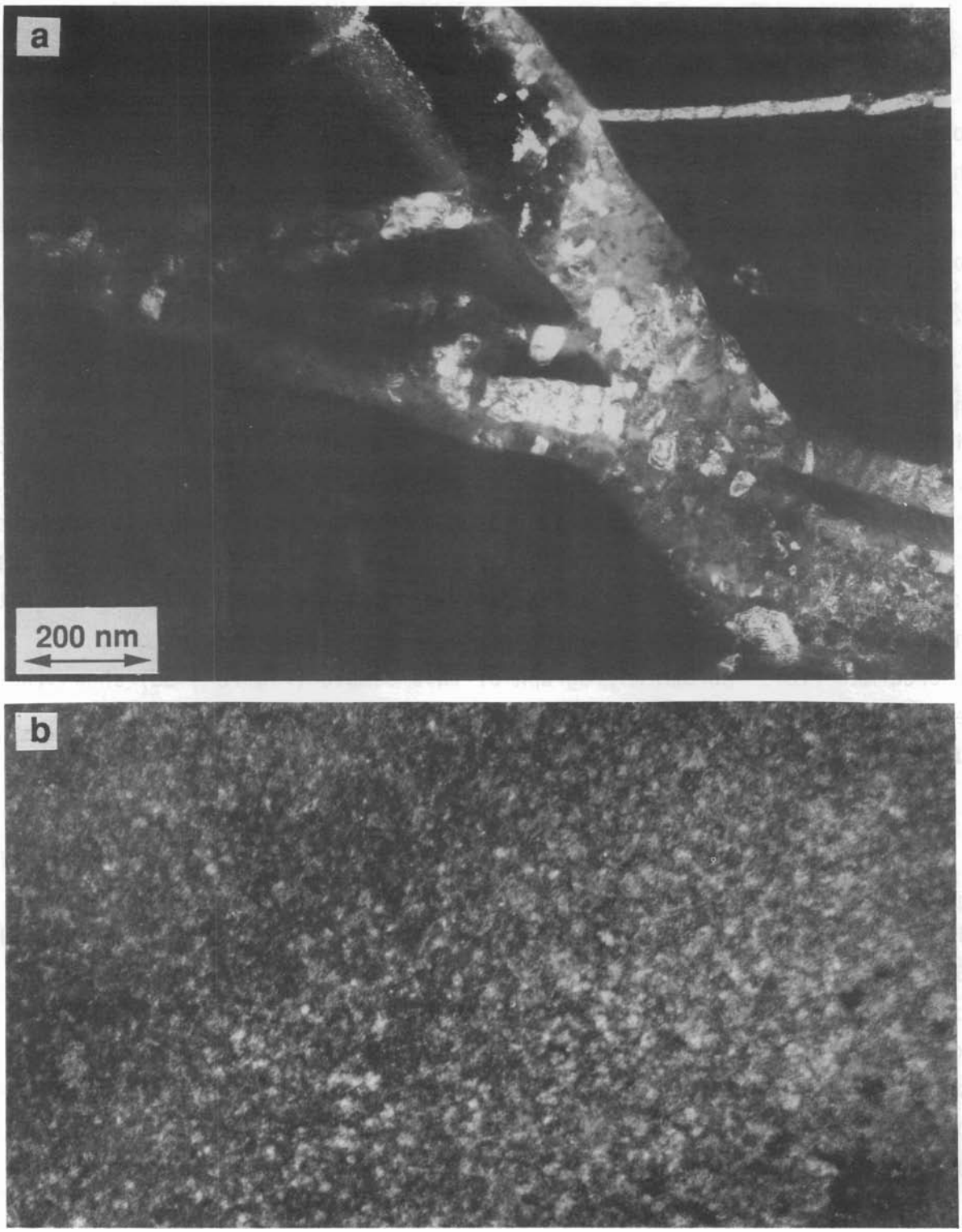

FIGURE 4.7. Oxidation Microstructures in Quad Cities BWR Fuel at O/M = 2.55, 190°C Test; a) Veins Containing Unidentified Polycrystalline Phase in α-U_3O_7 Matrix; b) Fine Domain Superstructure in U_3O_7 Grain

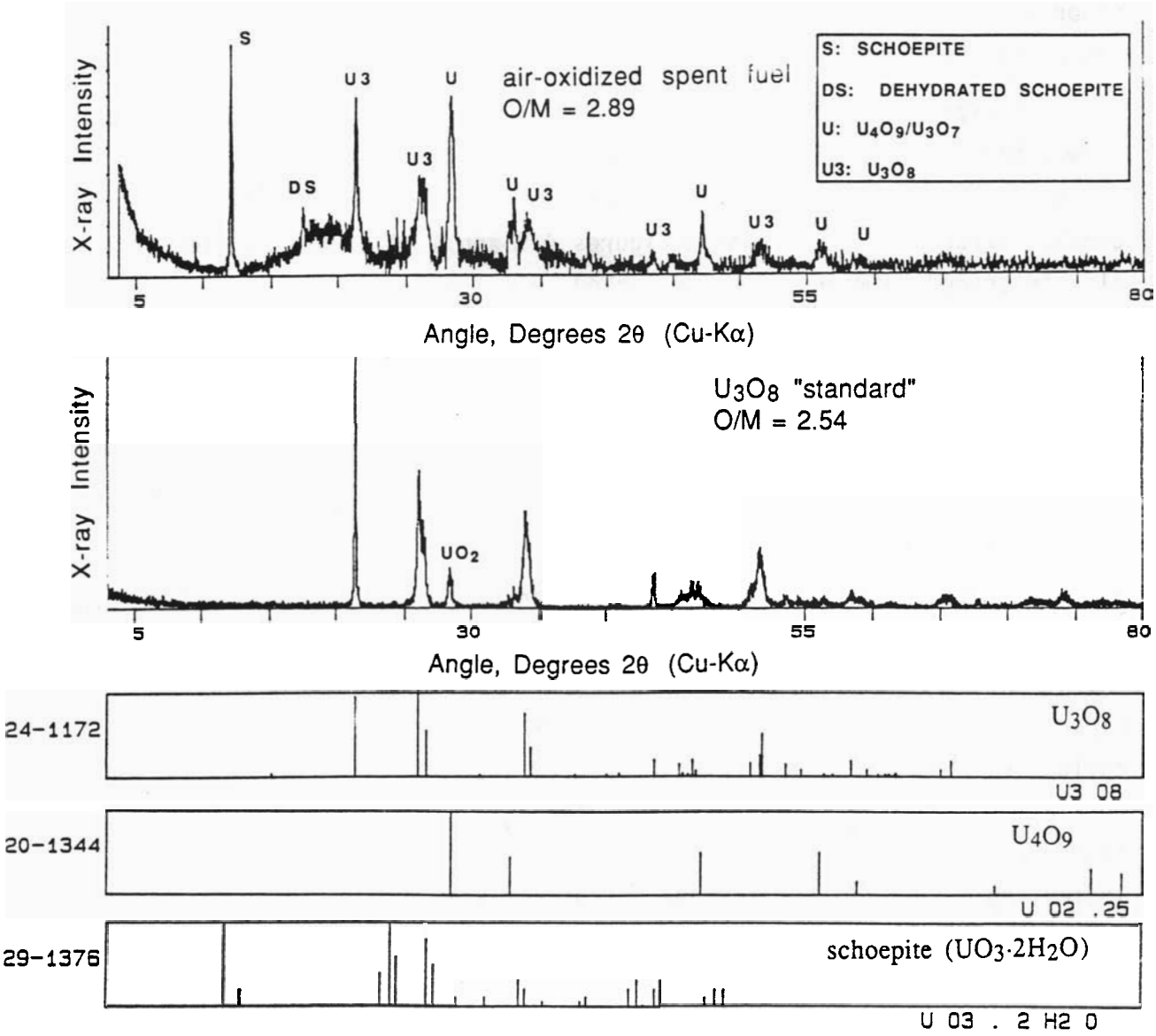

FIGURE 4.8. X-Ray Diffraction Analysis of Oxidized Spent Fuel Fragment from 230°C Oxidation Test: 1) X-Ray Diffractogram from Sample 86-29, Average O/M-2.89; b) Diffractogram from α-U_3O_8 "Standard Produced by Heating Nonirradiated UO_2 in Air at 400°C Average O/M-2.54. Unmarked Peaks are from U_3O_8. c-e) JCPDS Reference Patterns

this sample, and to the U_3O_8 formed from spent fuel, was JCPDS card No. 24-1172 for α-U_3O_8. The experimentally produced standard also contained minor peaks from U_4O_9. In contrast, oxidized spent fuel at O/M = 2.55 contained 100% U_4O_9.

TEM examination of fragment samples in the O/M range of 2.73 to 2.80 showed highly altered microstructures with microcracked vein networks containing fine-grained U_3O_8 in a matrix of fluorite-structure phases. These complex structures are shown in Figures 4.9 and 4.10. Both samples contained closely spaced networks of microcracked veins containing small particles of U_3O_8 along the veins. The image contrast characteristics of the vein material surrounding the small U_3O_8 particles indicated an amorphous phase. Imaging conditions for Figures 4.9 and 4.10 were chosen to highlight different aspects of the similar structures. The complex microstructures shown in these high-magnification photos occurred at the interiors of individual prior-UO_2 grains, and do not include prior-UO_2 grain boundaries.

The selected-area electron diffraction patterns (SADPs) from the oxidized samples also indicate the progression of oxidation structures with increasing O/M. SADPs taken near the (001) orientation are shown in Figure 4.11. Starting from UO_2, the formation of diffuse scattering reflections indicates the appearance of the U_4O_9 phase. With increasing O/M to 2.37, the diffuse reflections from the U_4O_9 become stronger and increasingly sharper. At O/M = 2.42 and 2.50, new spot patterns appear, indicating new phases. The fine-spot patterns at O/M = 2.50 are apparently from U_3O_7 because this phase was indicated in the sample by XRD. At O/M = 2.80, a ring pattern from polycrystalline U_3O_8 is superimposed on the spot patterns from fluorite-structure phases. However, the highly oxidized samples at O/M = 2.80 and >2.73 still contain large proportions of the fluorite structure phases in agreement with the XRD results.

Above O/M = 3.0, the samples were recovered as powders. Analyses of the highly oxidized powder samples by XRD indicated increasing formation of

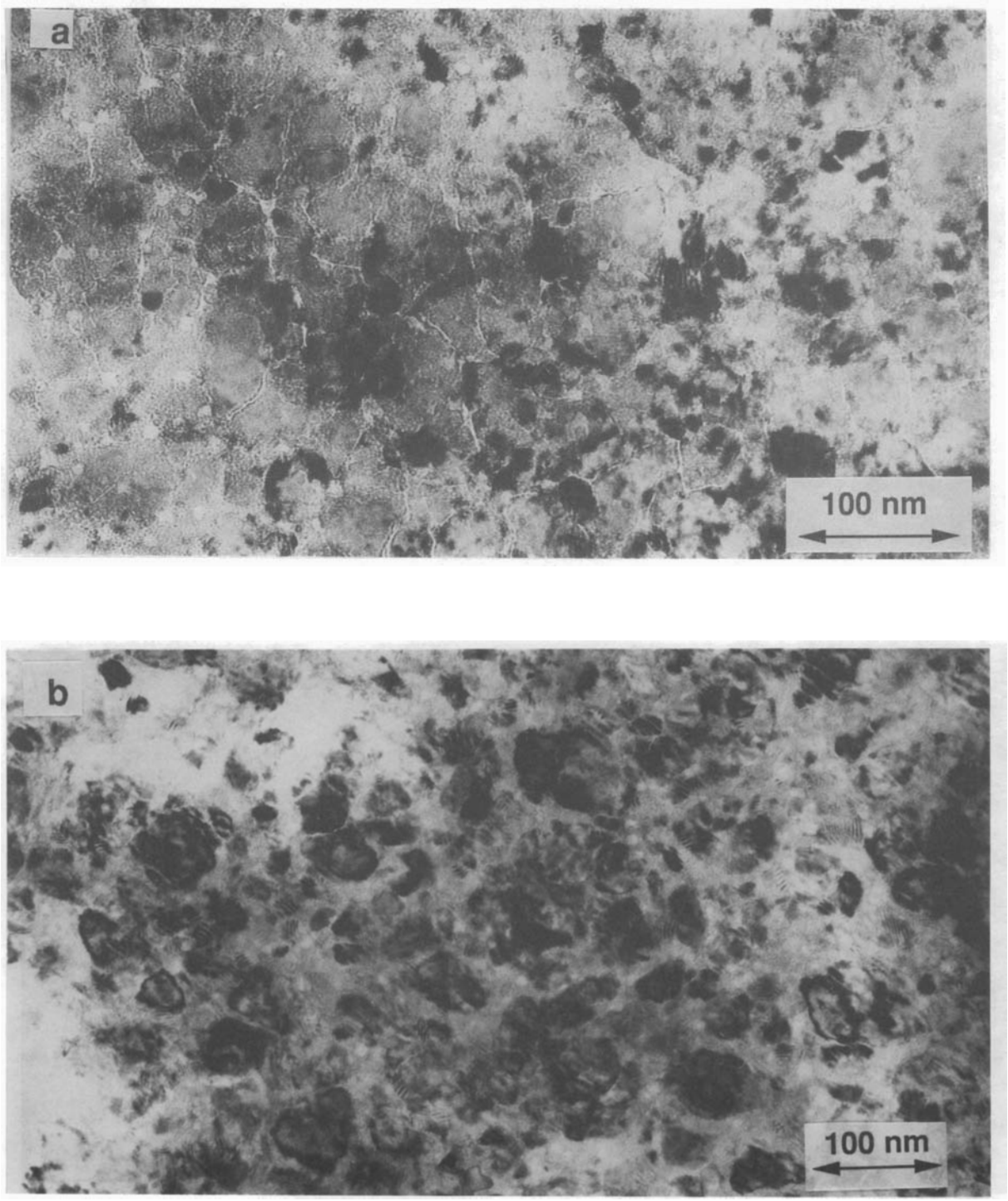

FIGURE 4.9. Microstructures in Oxidized Fuel at O/M ~2.73. Sample 86-30, Quad Cities Fuel Oxidized at 230°C, Brightfield TEM; a) Microcracks, U_3O_8 Grains, and Possibly Gas Bubbles Inside Prior UO_2 Grain, b) Retained U_4O_9 or $U3O_7$ (dark) in Similar Region to (a).

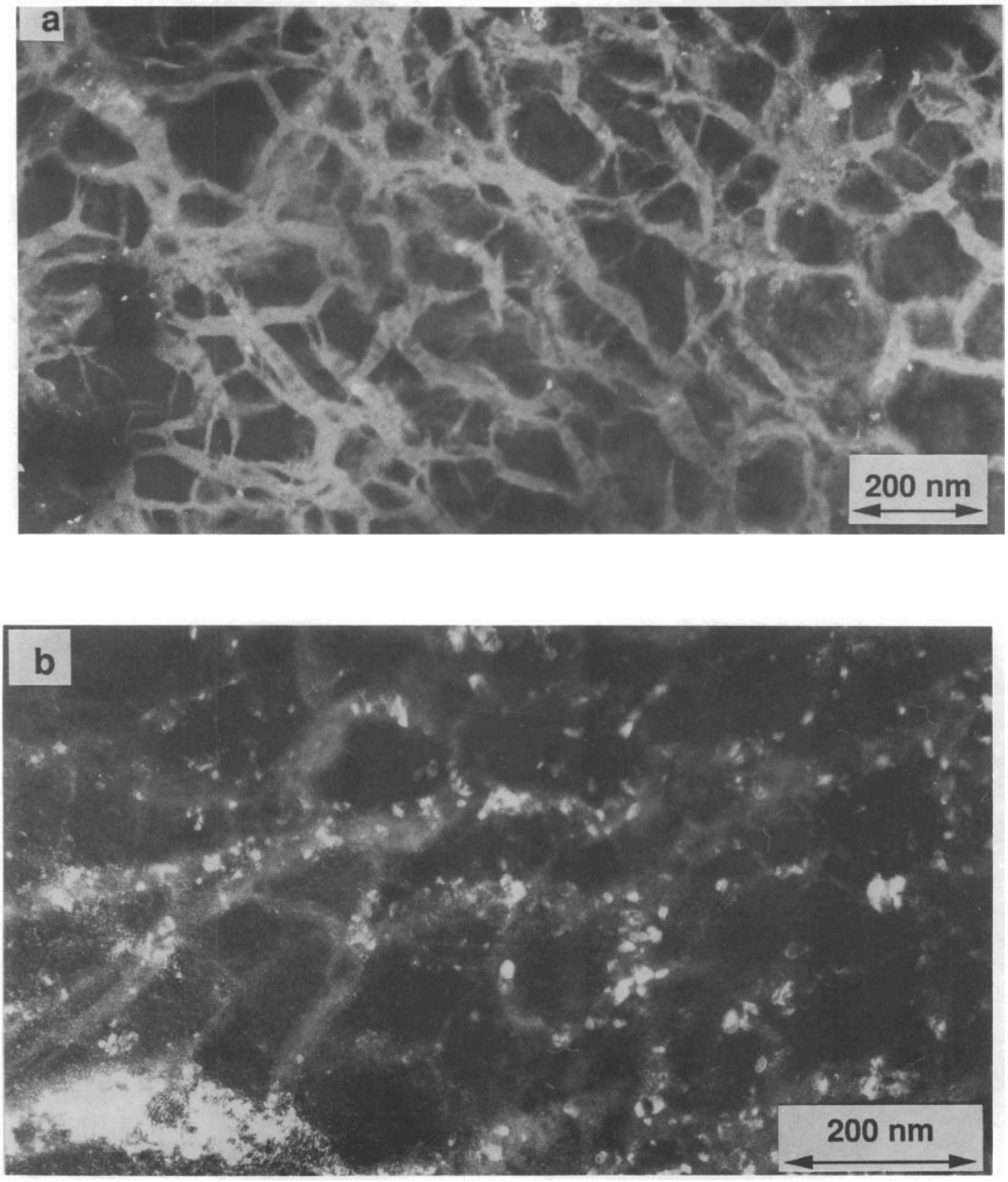

FIGURE 4.10. Microstructures in Oxidized Fuel at O/M = 2.80. Sample 86-34, H. B. Robinson Fuel Oxidized at 230°C, a) Vein Network, Possibly Containing Amorphous Material in Matrix of U_4O_9 or U_3O_7, TEM Darkfield; b) U_3O_8 Grains Along Vein Network.

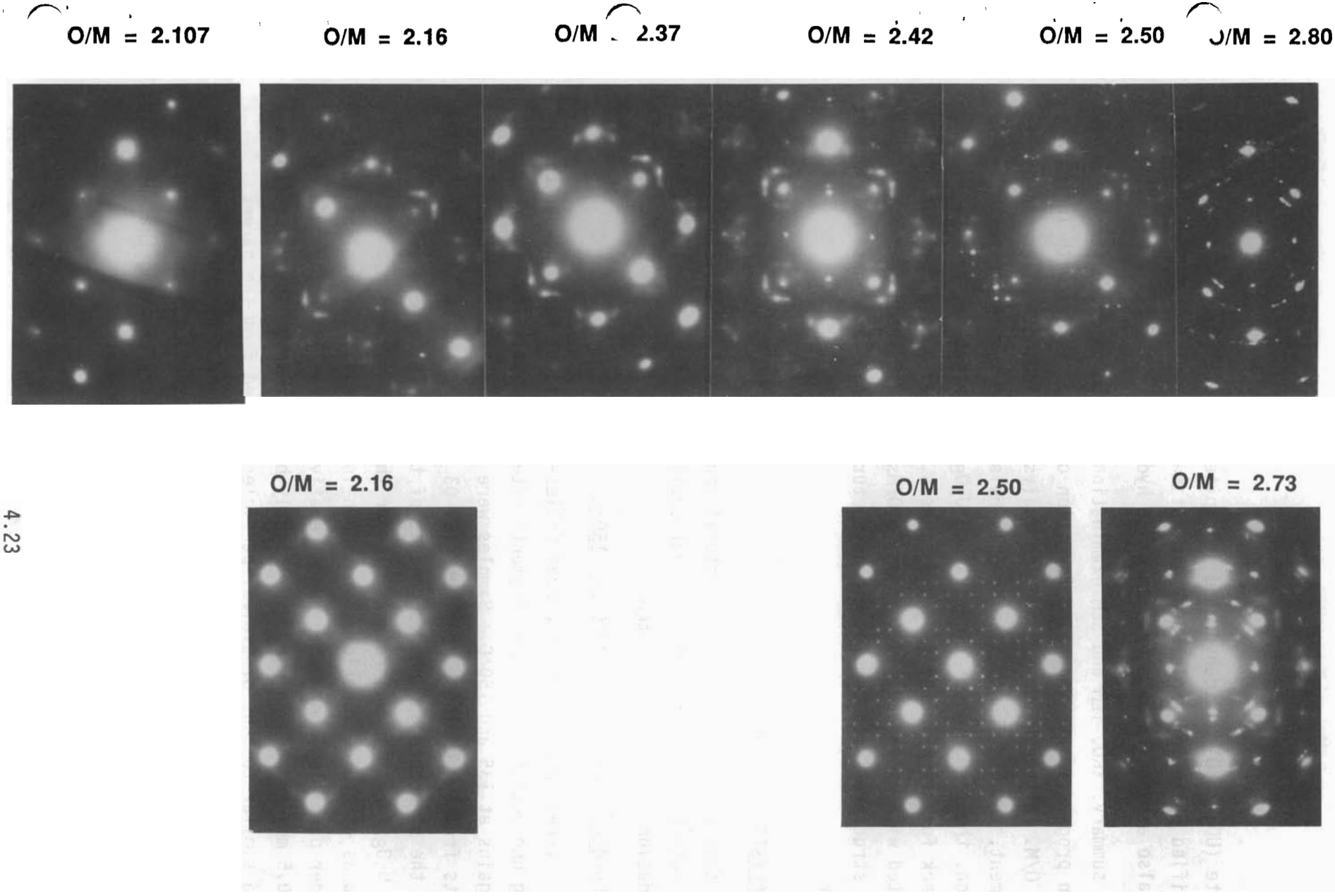

FIGURE 4.11. Electron Diffraction Patterns from Oxidized Fuel Samples. Showing characteristic patterns observed with increasing O/M. Crystallographic orientations near (001) zone axis of UO_2-type structures.

schoepite ($UO_3 \cdot 2H_2O$) and dehydrated schoepite ($UO_3 \cdot 0.8H_2O$). Another unidentified phase in sample 88-02 did not match any of the JCPDS references but is also assumed to be a uranium oxide hydrate.

In summary, XRD, TEM and SEM examinations of the oxidized samples showed a common progression to increased formation of higher oxides with increasing average O/M. Although the XRD and TEM analyses indicated similar phase development, the TEM showed fine details relating to the mechanisms of oxidation, the formation of fine grained U_3O_8 not detectable by XRD, microcrack formation in the U_4O_9/U_3O_7 phases, and gas bubble formation associated with oxidation. Oxidation to O/Ms near 2.8 produced greatly altered structures with complex microstructural changes and phase development behavior.

4.3 ANALYSIS OF POWDER SAMPLES

In this section, the microstructural characterization and phase identification results for powders that spalled from fuel fragments during the oxidation tests are presented.

4.3.1 Powder Formation at 135°C and 150°C

In several specimens of the Quad Cities-1 BWR spent fuel, powder began spalling unexpectedly from the fragments after relatively low exposures and weight gains at 135 and 150°C. Samples were obtained from powder and fragments from two of these specimens (87-03 at 135°C and 86-38 at 150°C) to compare the structure and phases content of the samples and to determine whether U_3O_8 formation was responsible for the power formation. SEM micrographs of typical particles are shown in Figure 4.12. Examination of the powder particles showed they were relatively large (effective diameter of nearly 0.5 mm) and composed of many tightly bound grains. Their structures appeared similar to that of typical particles chipped from the parent fragments. By their size, the "powder" particles cannot be truly considered a powder. High magnification SEM micrographs (Figures 4.12b and 4.12d) showed oxide coatings on the grains and grain boundary cracking that probably caused the particles to spall from the original fragments.

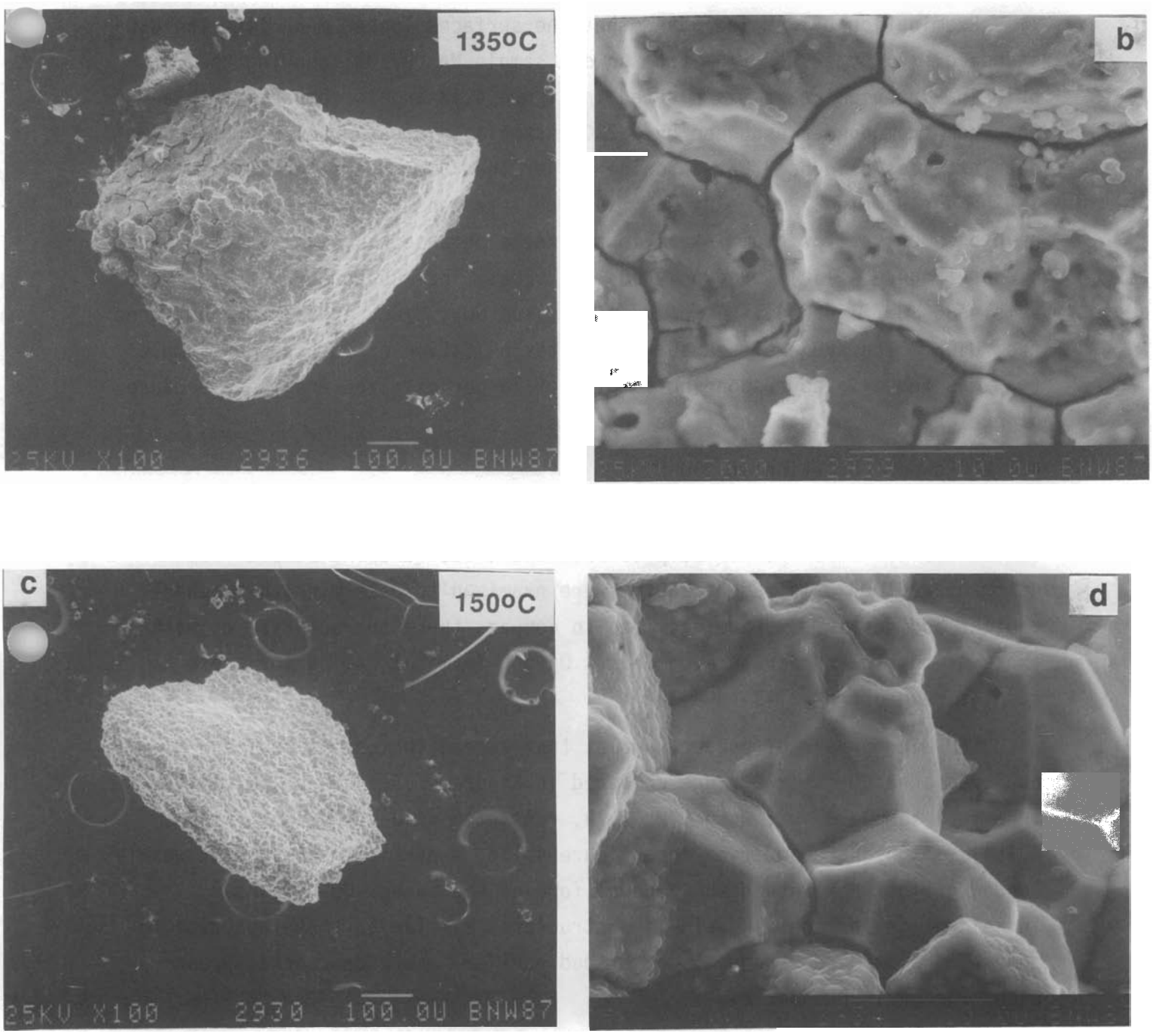

FIGURE 4.12. Powder Particles from Oxidation Tests; SEM Micrographs: a) Sample 87-03, Oxidized at 135°C, Average O/M - 2.007; b) Higher Magnification View of (a); c) Sample 86-38, Oxidized at 150°C, Average O/M - 2.15; d) Higher Magnification View of (c)

Examination by SAM indicated that the surfaces looked much like the U_3O_8 standard. An Auger spectrum from powder sample No. 87-03, showing the principal uranium peaks, is plotted in Figure 4.13 and is compared with a spectrum from powder produced by a 230°C sample (discussed below). The SAM data provides evidence that an oxide higher than UO_2 covers the surface of the powder sample 87-03. Any U_3O_8 surface layer on the powder particles must have been only a few atom layers in thickness because XRD examination of the powder (Figure 4.14a) found only UO_2 and U_4O_9. The XRD spectrum from powder sample 86-38 (Figure 4.14b) showed peaks from UO_2, U_4O_9, and α-U_3O_7, but none from U_3O_8. The XRD analyses showed greater oxidation of both powder samples than was found in corresponding samples of larger oxidized fragments because of preferential oxidation of the surfaces.

4.3.2 Powder Formation at 230°C

Powder formation was observed in many of the fuel specimens oxidized at 170 to 230°C. Three powder samples from spent fuel and one sample from unirradiated UO_2 oxidized at 250°C, were examined to determine their phase content and particle morphology, and to compare these characteristics with those of the low-temperature powders. Oxygen to metal ratios for these samples ranged from 2.73 to 3.78.

SEM micrographs of powder samples that formed from spent fuel and from nonirradiated UO_2 at 230°C are compared in Figure 4.15. Powder particles from fuel sample 87-02, with O/M ~2.73, consisted of a few grains (Figure 4.15a). At higher magnification, Figure 4.15b, a particle consists of weakly bonded grains that retain the general form of the parent UO_2 grains. Individual grains contain vein-like structures similar to those observed in some of the oxidized fragments described earlier, and wide cracks appear along the grain boundaries.

Analysis of powder sample 87-02 by XRD indicated a mixture of α-U_3O_8 and schoepite, with only a trace of retained U_4O_9. Compared to fragment samples with similar average O/Ms, the powders were more highly oxidized. Auger analysis of this sample (Figure 4.13b) also indicated conversion of the particle surfaces to U_3O_8.

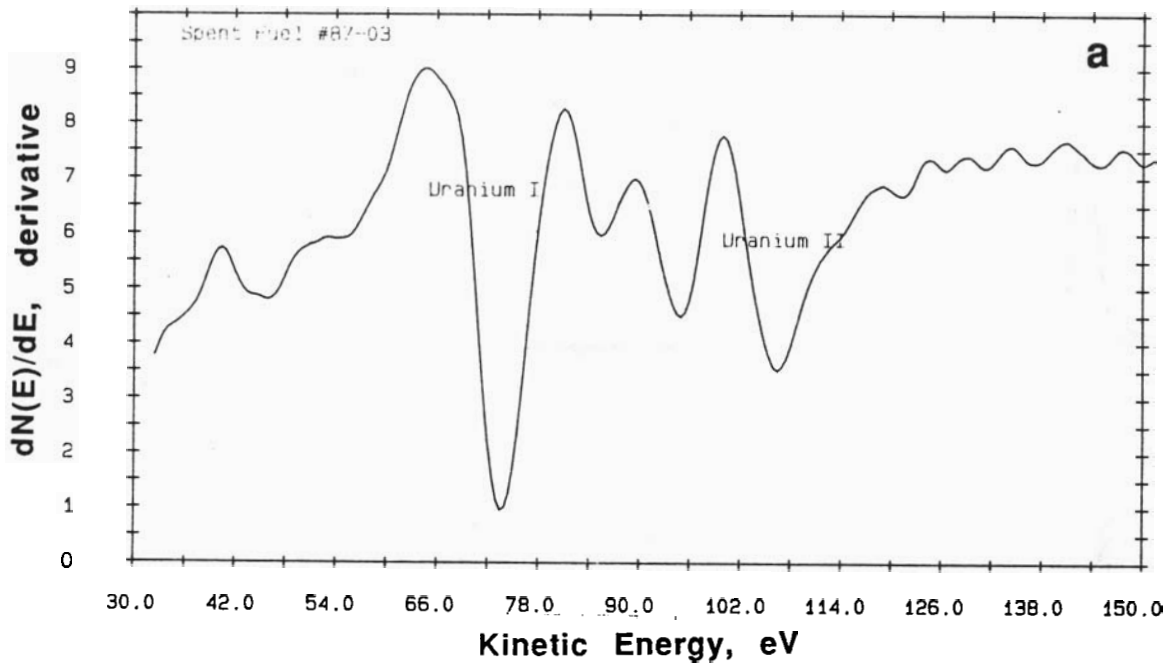

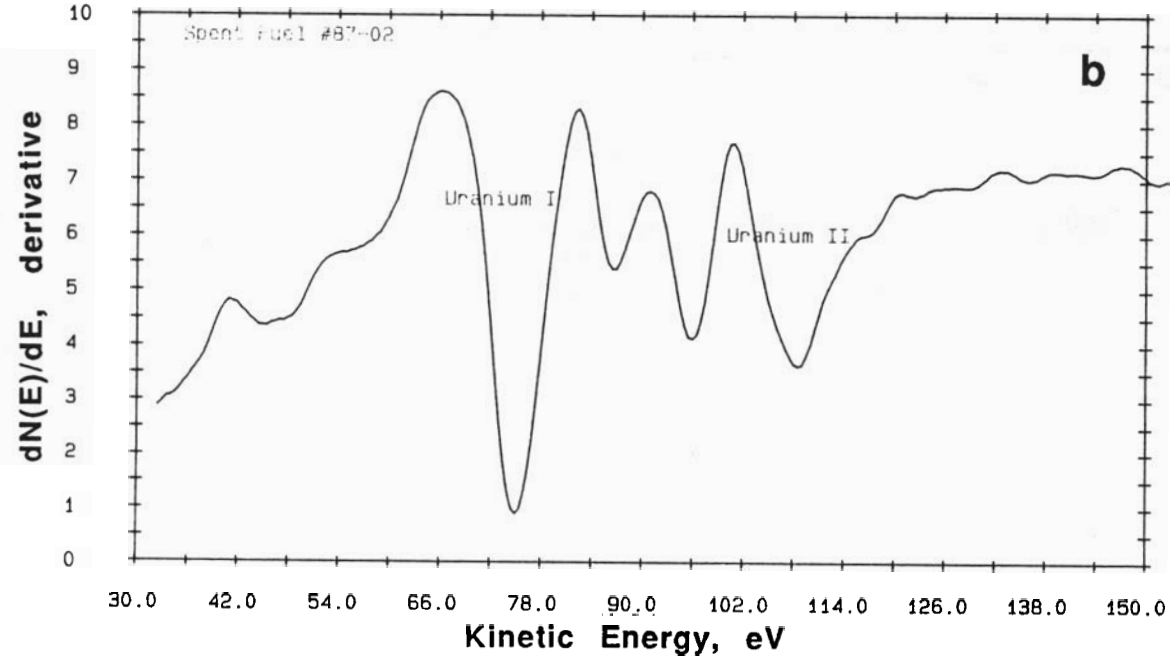

FIGURE 4.13. Expanded Auger Spectra from Powders Formed During Low-Temperature Oxidation (both are characteristic of U_3O_8): a) Sample 87-03, 135°C Oxidation; b) Sample 87-02, 230°C Oxidation

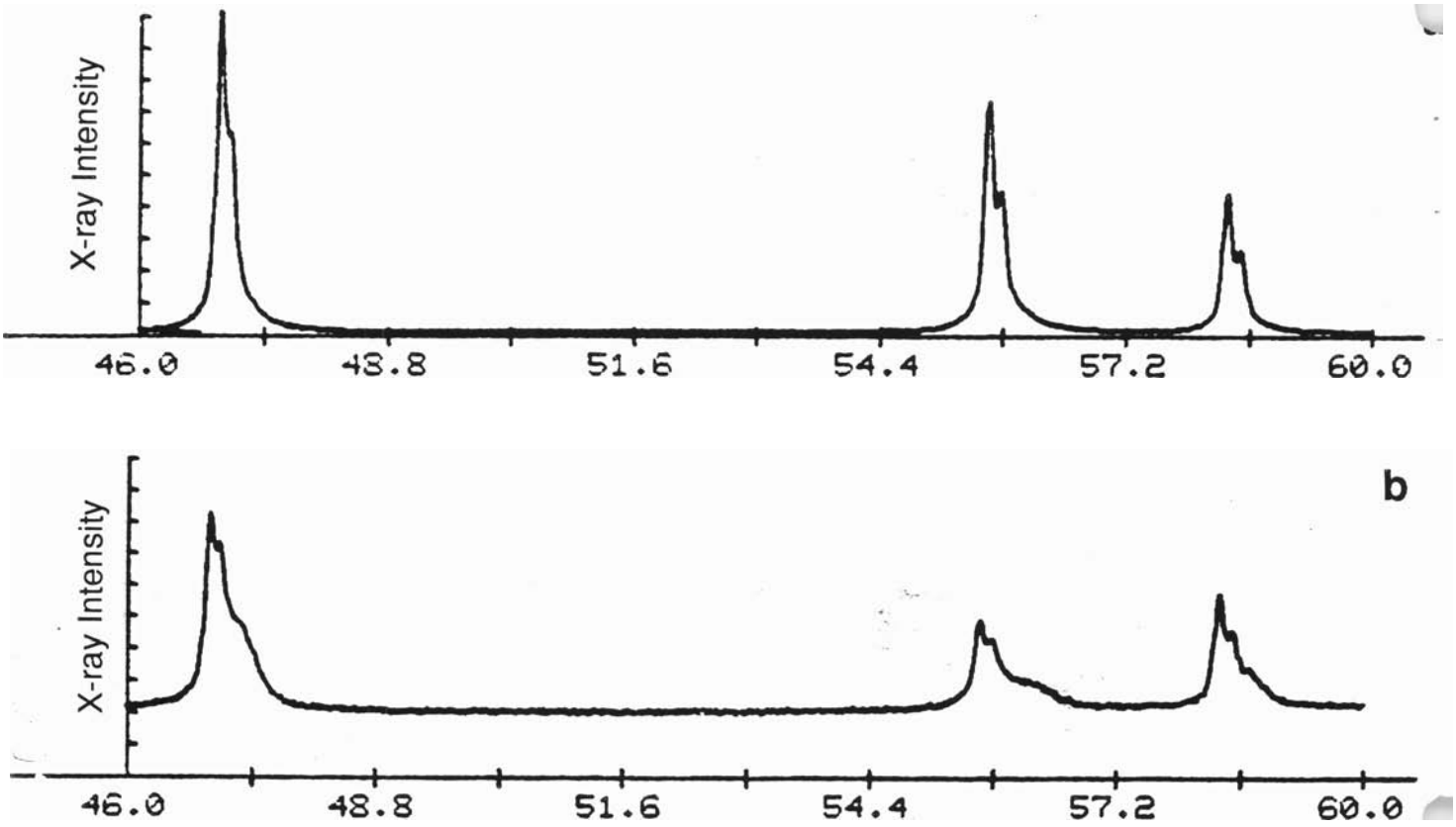

FIGURE 4.14. X-Ray Diffractograms from Powders Formed During Low-Temperature Oxidation: a) Sample 87-03 (135°C), Peaks are from UO_2 and U_4O_9; b) Sample 86-38 (150°C), Showing Peaks from UO_2, U_4O_9, and α-U_3O_7

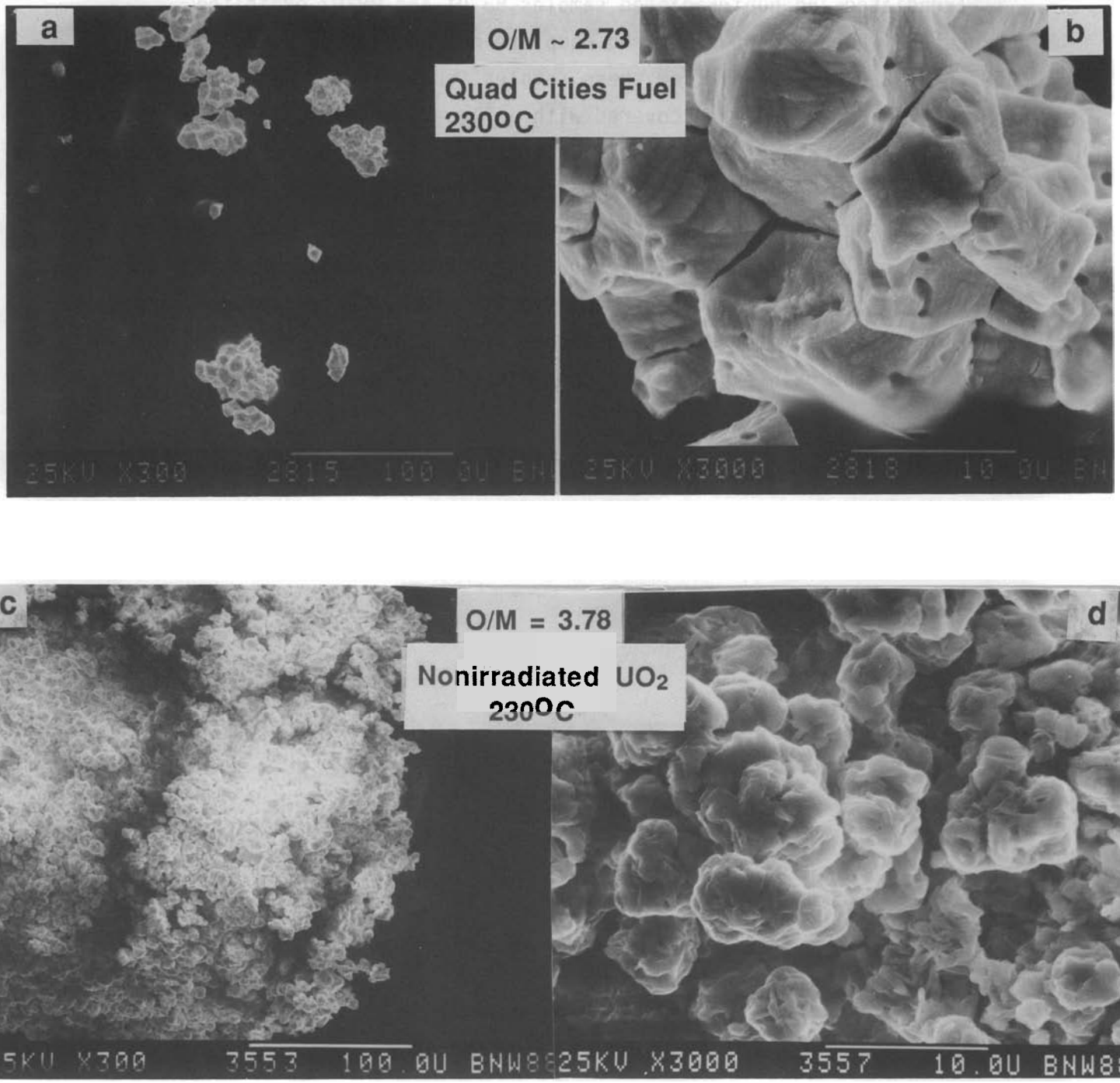

FIGURE 4.15. Powder Particles Formed During Oxidation at 230°; SEM Micrographs: a) Typical Particles Consisting of a Few Prior UO_2 Grains, Sample 87-02, O/M ~273; b) Higher Magnification View of (a); c) Nonirradiated UO_2 Sample 88-02, O/M = 3.78; d) Higher Manification View of (c)

Irradiated and nonirradiated samples 88-01 and 88-02 exhibited unexpectedly high weight gains and complete degradation to powder after 13597 h at 230°C. Grains from these samples, shown in SEM micrographs in Figure 4.14c and 4.16d, are covered with a flowery oxide scale and have lost their polyhedral shapes. XRD analysis (Figure 4.16) showed that the samples consisted of α-U_3O_8 and hydrates. In spent fuel sample 88-01 (average O/M-3.2), the predominant hydrate was dehydrated schoepite ($UO_3 \cdot 2H_2O$) and a phase that could not be identified from the JCPDS database. Probably the unidentified phase is another uranium hydrate. Hydrate formation during the oxidation tests in moist air could account for observed weight gains that exceeded the ~6% gain expected for complete conversion to UO_3.

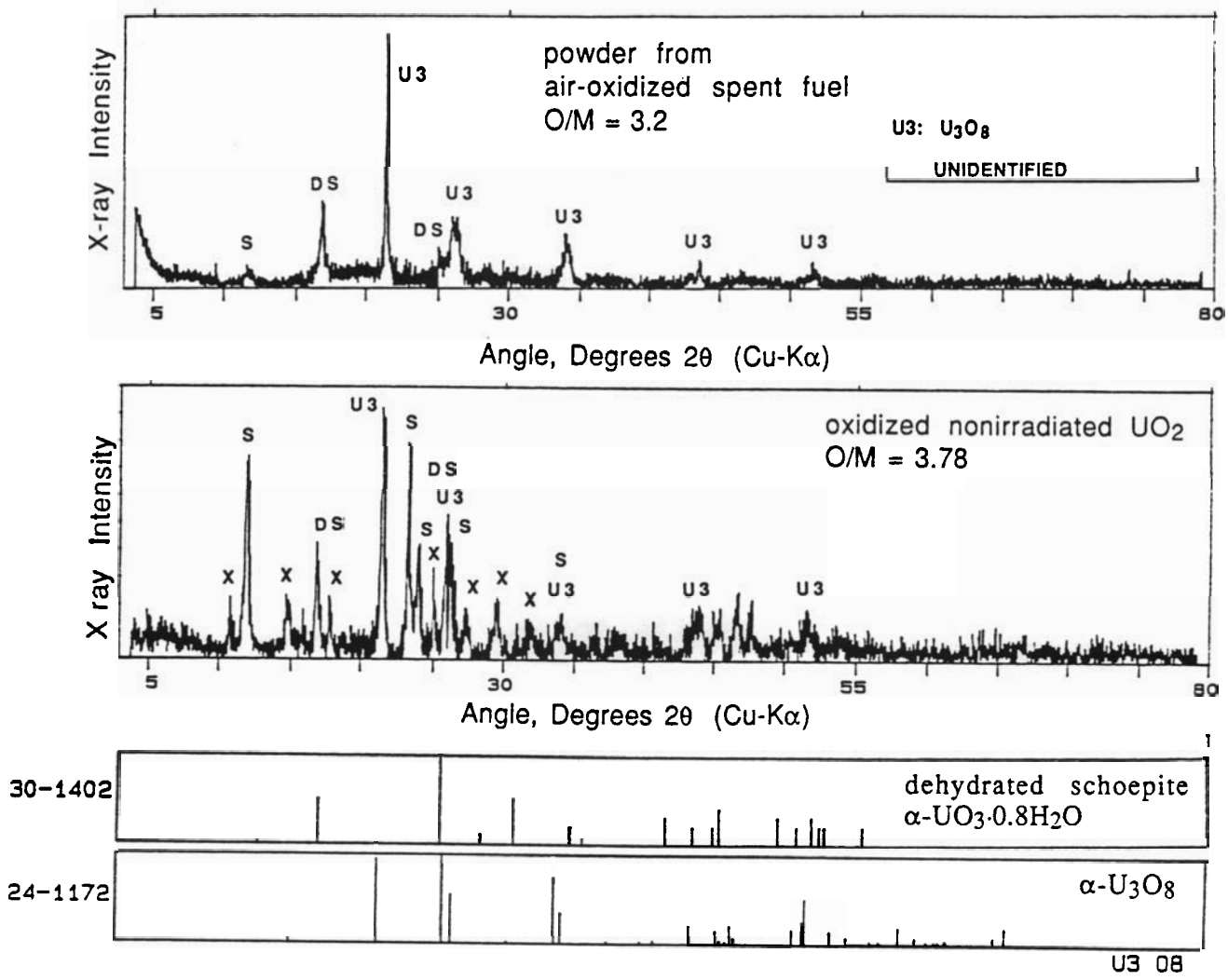

FIGURE 4.16. X-Ray Diffractograms from Powders Formed by Oxidation of Spent Fuel at 230°C: a) Spent Fuel Sample 88-01, Average O/M-3.2; Consisting of α-U_3O_8, Dehydrated Schoepite, and Schoepite; b) Nonirradiated Sample 88-02, Average O/M-3.78, Containing More Schoepite and Additional Unidentified Phase (probably also a hydrate); c and d) JCPDS Reference Patterns for α-U_3O_8 and Dehydrated Schoepite

5.0 DISCUSSION

Results of weight-gain measurements and observations of powder formation in the continuing oxidation tests (Campbell et al. 1987) have raised the following questions: 1) To what extent is the present understanding of oxidation behavior in UO_2 applicable to LWR spent fuels? 2) At what O/M ratio does significant formation of U_3O_8 begin in spent fuel? 3) Is powder formation a reliable indicator of U_3O_8 formation in spent fuel? 4) What causes the high weight gains (O/Ms above 3.0) observed in some tests? 5) What are the mechanism(s) of oxidation in spent fuel, and how do these differ from oxidation mechanisms in nonirradiated UO_2? 6) What changes caused by oxidation in air could cause fuel swelling and possible splitting of breached fuel rods? Some answers based on the microstructural characterization results, and speculation concerning the differences in oxidation behavior of spent UO_2 fuel and nonirradiated UO_2, are presented in this section.

5.1 APPLICABILITY OF PHASE DIAGRAMS TO SPENT FUEL OXIDATION IN AIR

This investigation into the progression of oxidation in UO_2 provided compelling evidence that the oxidation behavior of spent UO_2 fuel differs from that of nonirradiated UO_2. Although the phases formed during oxidation of spent fuel at 135 to 230°C--U_4O_9, U_3O_7, and U_3O_8--are superficially familiar from phase diagrams established by oxidation studies of non-irradiated UO_2, standard phase diagrams are inapplicable to spent fuel. This conclusion is reached from the following observations:

- During initial oxidation of solid spent-fuel fragments, U_4O_9 forms directly from UO_2, growing from the grain boundary edges into the centers of the UO_2 grains. In nonirradiated fuel oxidized at similar temperatures, XRD and XPS analyses (Allen, Tempest and Tyler 1987) indicate that β-U_3O_7 forms directly from the UO_2 surfaces without forming U_4O_9.
- The U_4O_9 formed during air oxidation of spent fuel was γ-U_4O_9, not the β-U_4O_9 indicated on phase diagrams for nonirradiated UO_2.
- U_4O_9 was present in the spent fuel samples at average O/M ratios to 2.9. Samples composed entirely of U_4O_9 were found at average O/Ms to 2.55. At this composition, the phase diagrams for nonirradiated material

indicate conversion to mixtures of U_3O_7 and U_3O_8. Significant conversion of the spent fuels to U_3O_8 was not found below O/Ms near 2.8.

- The U_3O_7 found in oxidized fuel samples was α-U_3O_7 or another variant not in the JCPDS database, not the β-U_3O_7 usually produced by oxidizing nonirradiated UO_2 at similar test temperatures.
- Oxidation of the fuels to O/Ms above about 2.9 produced a hydrate phase (schoepite) rather than UO_3. No UO_3 was found in the oxidation tests with spent fuel.

The standard phase diagrams developed from studies on nonirradiated UO_2 are inapplicable to spent UO_2 fuel under the conditions of the present oxidation tests. It is suspected that the entire phase development sequence observed in these tests reflects nonequilibrium oxidation behavior. A clear example of nonequilibrium behavior in these tests is the limited formation of U_3O_8 at O/M ratios greater than the known composition of the phase ($UO_{2.667}$).

5.2 U_3O_8 FORMATION

Concerns about formation of U_3O_8 in LWR spent fuel arise from the large volume change (about 28%) that accompanies the $UO_2 \rightarrow U_3O_8$ transformation and the possibility of rupturing the cladding in defected fuel rods by oxidation-induced swelling of the fuel. To predict allowable conditions for storing spent fuel rods in air, i.e., times and temperatures for which no appreciable fuel swelling occurs, oxidation models must relate the results of weight gain measurements to the phase development.

Compared to nonirradiated UO_2, significant U_3O_8 formation (detectable by XRD) in spent fuel occurs at relatively high weight gains (O/Ms of 2.8 or greater). Although the weight gain results are outside the scope of this report, U_3O_8 formation also appears to be delayed to longer times in spent fuel.

5.3 POWDER FORMATION

Powder formation during oxidation of spent fuel is not a reliable indicator of U_3O_8 formation. Examination of powders formed at test temperatures of 135°C and 150°C showed no U_3O_8 detectable by XRD. These "powder" particles were composed of UO_2 and U_4O_9 plus α-U_3O_7 (in the 150°C

test sample). Although a thin layer of U_3O_8 on the particles surfaces was indicated by Auger analysis, such coatings could have formed by oxidation of exposed surfaces after the grain boundaries became fractured. Microstructural observations of fuel samples oxidized at these temperatures suggest that powder forms during low-temperature oxidation by breaking small pieces of fuel along grain boundaries that become cracked during initial formation of U_4O_9. In LWR spent fuel, the initial stage of oxidation from UO_2 to U_4O_9 involves grain boundary cracking driven by the density decrease of the $UO_2 \rightarrow U_4O_9$ transformation. Powder formation during low-temperature oxidation of spent fuel may be a consequence of the fuel's tendency to oxidize preferentially along gas-bubble-coated grain boundaries and crack along the oxidized boundaries.

At the highest oxidation temperature, 230°C, the oxidized samples remained generally intact despite extensive formation of U_3O_8. Although some powder usually formed during the 230°C tests, the particles were more highly oxidized than the parent fragments and were extensively converted to hydrates. It is, therefore, possible that the powder formation observed in the spent fuel that formed U_3O_8 in tests at 230°C could be related to hydrate formation.

5.4 HIGH WEIGHT GAINS

The high weight gains observed in some oxidation tests, corresponding to O/Ms above 3.0, were associated with formation of uranium oxide hydrate (schoepite) and an unknown phase (apparently another hydrate that formed after schoepite). Hydrate formation occurred at the expense of the uranium oxide phases. Schoepite and dehydrated schoepite were detected by XRD at O/Ms near 2.8, just after U_3O_8 appeared. The high weight gains measured during the oxidation tests appeared consistent with the phase contents of the samples indicated by XRD analyses.

5.5 OXIDATION STAGES IN SPENT FUEL

Based on characterization of oxidized fuel samples, low-temperature oxidation of LWR spent fuels in air can be considered to occur in the following four stages of microstructural development:

In Stage I, observed at average O/Ms up to about 2.2 in this work, oxygen initially penetrates along grain boundaries and through open porosity in the spent fuel, forming U_4O_9 along the grain boundaries and leaving nonoxidized UO_2 at the grain cores. This initial stage of oxidation was described for H. B. Robinson spent fuel by Thomas, Einziger and Woodley (1989). The U_4O_9 replaces UO_2 without major rearrangement of the UO_2 crystal lattice by advancing a coherent, regular U_4O_9/UO_2 interface into the grains. In this stage, two kinds of oxidation fronts exist in competition: the macroscopic front separating nonoxidized UO_2 regions from regions in which the grain boundaries have converted to U_4O_9 and the microscopic fronts within the partially oxidized grains.

A contributing factor in the oxidation process in Stage I may be the opening of cracks along oxidized grain boundaries. The lattice shrinkage of the $UO_2 \rightarrow U_4O_9$ transformation causes this cracking. The cracks appear first at the grain-boundary triple points (grain corners) and spread along the grain faces, as does the U_4O_9. Scattered transgranular cracks also form at this stage, allowing oxidation to also initiate within some UO_2 grains.

In Stage II, found at O/Ms of about 2.3 to 2.5, closely spaced microcracks develop within the U_4O_9 grains. In effect, the microstructure becomes broken into a mosaic of small, misfitting blocks about 100 nm in diameter. Microcracking may be an accommodation of the UO_2 lattice structure to excess oxygen above the normal limiting composition of $UO_{2.25}$ for U_4O_9, and might be caused by the same tetragonality strains that produce U_3O_7. Peak broadening observed in the XRD patterns from U_4O_9 and U_3O_7 in the oxidized fuel samples is a possible indication of the lattice strains in these phases.

Stage II microcracking in oxidized spent fuel produces a possibly significant contribution to fuel swelling that is not related to U_3O_8

formation. If the total volume of the microcracks is large enough to offset the lattice shrinkage caused by formation of U_4O_9 from UO_2, a net expansion can occur.

Formation of microcrack-free U_3O_7 (in sample 86-27A, with O/M = 2.50) may be an alternative path for microstructural development during oxidation of spent fuel. Formation of U_3O_7 instead of U_4O_9 at O/Ms between 2.4 and 2.5 occurred only in low-burnup fuel and therefore might be influenced by burnup.

In Stage III development of oxidation microstructures, at O/Ms from about 2.5 to 2.8, fine-grained U_3O_8 forms along the networks of microcracks within U_4O_9. The U_3O_8 forms within vein-like structures that coincide with the microcracks but apparently develops from the U_4O_9. With increasing O/M in this range, the proportion of U_3O_8 increased without reducing the samples to powder.

Stage IV, beginning near O/M = 2.8, corresponds to formation of hydrates at the expense of the uranium oxide phases. UO_3 was not detected (by XRD) as an intermediate product between Stages III and IV. At O/M = 3.2, an oxidized fuel sample was partly converted to dehydrated schoepite and, at O/M = 3.78, a nonirradiated UO_2 sample converted beyond schoepite to an unknown (hydrate) phase.

Several factors may be responsible for the apparent differences in oxidation behavior and microstructural development in spent fuel and nonirradiated UO_2. These factors include 1) the slow approach to equilibrium at the low oxidation temperatures in the present tests, 2) the availability of different oxidation pathways in spent fuel (e.g., gas-bubble-coated grain boundaries in the spent fuel), and 3) the chemical composition of the UO_2 matrix in spent fuel. Typically, the UO_2 in LWR fuels at moderate burnups contains several percent of mixed fission products--for example, zirconium, rare earth elements, strontium, barium, and cesium--plus about 1% plutonium). In addition, spent fuel contains radiation damage--frozen-in vacancies, interstitials, defect complexes, and possibly larger defect cluster--that could affect the development or stabilities of higher oxides such as U_4O_9 or U_3O_7.

5.6 FUEL EXPANSION CAUSED BY OXIDATION

Concerns about volume expansion of fuel during oxidation usually focus on U_3O_8 formation. At least two other possible sources of fuel swelling may be considered. Initial oxidation of UO_2 to form U_4O_9 or U_3O_7 involves a small density decrease of the fluorite structure lattice. In oxidized fuel at O/Ms near 2.5, however, high densities of microcracks form throughout the U_4O_9 grains. **The volume increase caused by microcracking might produce a net** volume expansion without forming U_3O_8. Based on observation of the microcracks in Figure 4.6a, a structure containing uniformly distributed microcracks 1 nm in width and spaced an average of 50 nm apart would cause a 6% volume expansion. **Such an expansion in clad fuel might be enough to** rupture the cladding by extending an existing cladding breech.

Fuel oxidation behavior, as indicated by oxidation weight gains, appeared insensitive to the humidity level of the test ovens (Campbell 1987). However, samples from these tests tended to form hydrates directly from U_3O_8 rather than forming intermediate UO_3. **The volume expansion caused by the** $U_3O_8 \rightarrow UO_3 \cdot 2H_2O$ transformation is not as large as the expansion associated with $U_4O_9 \rightarrow U_3O_8$ conversion but might be an important factor in the integrity of defected fuel rods stored in moist air.

Another possible source of fuel expansion without forming U_3O_8 is gas bubble formation by oxidative release of fission gases from solution in the UO_2 matrix. **Bubble formation associated with oxidation was observed in** several fuel samples with O/Ms from 2.4 to 2.7. Estimated volumes occupied by bubbles in these samples (see Figures 4.6c and 4.9a) are about 0.1 to 1%.

6.0 CONCLUSIONS

Air-oxidized UO_2 spent fuel samples representing a wide range of oxidation times, temperatures, fuel types, and final oxide compositions indicated by oxidation weight gains were analyzed by X-ray diffractometry, transmission electron microscopy, Auger electron spectrometry, and scanning electron microscopy. Conclusions from this work in relation to modeling and predicting the behavior of LWR spent fuel in dry air storage are as follows:

- The oxidation behavior of spent fuel in air at 135 to 230°C differs from that of nonirradiated UO_2. Present understanding of oxidation in nonirradiated UO_2 is inapplicable to spent UO_2 fuel.
- The onset of significant U_3O_8 formation occurs at higher average O/Ms in LWR spent fuel (between O/Ms of 2.5 and 2.7) than in nonirradiated UO_2. Formation of U_3O_8 is delayed to longer times in the spent fuel.
- Powder formation is not a reliable indicator of U_3O_8 formation during oxidation of spent fuel. Powders formed during oxidation tests at 135 and 150°C are mostly UO_2 and U_4O_9. At 170, 190, 210, and 230°C, U_3O_8 is produced without powder formation.
- High O/Ms (>3.0) determined by oxidation weight gains are associated with the formation of uranium oxide hydrates.
- The phase development sequence in spent fuel during the 135 to 230°C tests was usually $UO_2 \rightarrow \gamma\text{-}U_4O_9 \rightarrow \alpha\text{-}U_3O_8 \rightarrow UO_3 \cdot H_2O$ (dehydrated schoepite) $UO_3 \cdot 2H_2O$ (schoepite). In some tests, $\alpha\text{-}U_3O_7$ also appeared between U_4O_9 and $\alpha\text{-}U_3O_8$.
- Significant volume expansion of spent fuel during oxidative phase transformations may occur by several mechanisms besides U_4O_9 conversion. Other proposed expansion mechanisms include formation of uranium oxide hydrates, microcrack formation in U_4O_9 or U_3O_7, and bubble formation by release of trapped fission gases during oxidation. Microstructural evidence of these effects was observed during this work.

7.0 PLANS FOR CONTINUING WORK

The oxidation tests with bare fuel and nonirradiated UO_2 are being continued to cumulative times of 35,000 hours or more to assure that the oxidation rates determined by weight-gain measurements remain stable during proposed intervals of dry storage in air. The tests will be completed in 1990. Also in these tests are artificially breached fuel rods. Fuel samples from rods with cladding that split open during the tests are being analyzed to determine the cause of the splitting. Results of the analyses by ceramography, immersion density measurement, O/M determination, XRD, and TEM will be reported in 1991 (Volume IV of this report series). Also, selected samples of oxidized bare fuel will be further characterized by XRD to monitor phase development at the long exposure times.

8.0 REFERENCES

Abmann, H., E. Merz, A Naoumidis, H. Nickel, H. Stehle, and G. N. Walton. 1982. Gmelin Handbook of Inorganic Chemistry. Suppl. Vols. C1, C2, C3, C4, C5, eds. K. Buschbeck and C. Keller. 8th ed. Springer-Verlag, New York.

Allen, G. C., P. A. Tempest, and J. W. Tyler. 1987. "Oxidation of Polycrystalline UO_2 Studied Using X-ray Photoelectron Spectroscopy and X-ray D Diffraction." J. Chem. Soc. Faraday Trans., 83:925-935.

Bennett, M. J., J. B. Price, and P. Wood. 1987. "Influence of Manufacturing Route and Burnup on the Oxidation and Fission Gas Release Behaviour of Irradiated Uranium Dioxide in Air at 175-400°C." In Proceedings from Chemical Reactivity of Oxide Fuel and Fission Product Release, pp. 157-174. Berkeley Nuclear Laboratories, Berkeley, California.

Boase, D. G., and T. T. Vandergraff. 1977. "The Canadian Spent Fuel Storage Canister: Some Materials Aspects." Nuclear Technology 32:60-71.

Briggs, D., and M. P. Seah. 1983. Practical Surface Analysis by Auger Spectroscopy and X-ray Photoelectron Spectroscopy. eds. D. Briggs and M. P. Seah. John Wiley and Sons, New York.

Campbell, T. K., E. R. Gilbert, C. A. Knox, G. D. White, G. F. Piepel, and C. W. Griffin. 1987. Interim Results from UO_2 Fuel Oxidation Tests in Air. PNL-6201, Pacific Northwest Laboratory, Richland, Washington.

Colmenares, C. A. 1975. "The Oxidation of Throium, Uranium, and Plutonium." Solid State Chemistry, Vol. 9, Eds. J. O. McCaldin and G. Somorjai. Pergamon Press, Oxford, pp. 139-239.

Colmenares, C. A. 1984. "Oxidation Mechanisms and Catalytic Properties of the Actinides." Prog. Solid State Chemistry. Vol. 15, eds. G. M. Rosenblatt and W. L. Worrell, pp. 257-364. Pergamon Press, Oxford.

Einziger, R. E., and R. V. Strain. 1986. Oxidation of Spent Fuel Between 250 and 360°C. EPRI NP-4524, Electric Power Research Institute, Palo Alto, California.

Guenther, R. J., D. E. Blahnik, T. K. Campbell, U. P. Jenquin, J. E. Mendel, L. E. Thomas, and C. K. Thornhill. 1988. Characterization of Spent Fuel Approved Testing Material - ATM-103. PNL-5109-103, Pacific Northwest Laboratory, Richland, Washington.

Hoekstra, H. R., and S. Siegel. 1973. "The Uranium Trioxide-Water System." J. Inorg. Nucl. Chem. 35:761-779.

Hoekstra, H. R., S. Siegel, and F. X. Gallagher. 1970. "The Uranium-Oxygen System at High Pressure." J. Inorg. Chem. 32:3237-3248.

Joint Committee on Powder Diffraction Studies (JCPDS). 1988. Powder Diffraction File - Inorganic Phases. JCPDS-International Center for Diffraction Data, Swarthmore, Pennsylvania.

Keller, G. 1973. "The Actinides: Binary and Ternary Oxides, Hydroxides and Hydrous Oxides, Peroxides, Phosphates, and Arsenates." In Comprehensive Inorganic Chemistry, eds. J. C. Bailar et al., pp. 219-276. Pergamon Press, New York.

McCarthy, J. M., and L. E. Thomas. 1985. "Preparation of TEM Specimens from Highly Radioactive Materials." In. Proceedings of the 43rd Annual Meeting of the Electron Microscopy Society of America, ed. G. W. Bailey, pp. 184-185. San Francisco Press, San Francisco.

Roberts, J. P. 1988. "Limited Proprietary Review of Nuclear Regulatory Commission (NRC) Staff's Final Safety Evaluation Report (SER) for the FW Energy Applications." In Topical Report for the Foster Wheeler Modular Vault Dry Store (M.V.D.S.) for Irradiated Nuclear Fuel, Revision 1. Project M-46. (Accession No. 8803290114-880323.)

Roth, R. S., T. Negas and L. P. Cook. 1981. Phase Diagrams for Cerasists, Volume IV. American Ceramics Society, Columbus, Ohio.

Smith, D. K. 1984. "Uranium Mineralogy." In Uranium Geochemistry, Mineralogy, Exploration, and Resources, ed. B. DeVivo. Institution of Mining and Metallurgy, London.

Taylor, P., E. A. Burgess and D. G. Owen. 1980. "An X-Ray Diffraction Study of the Formation of β-UO2 $_{33}$ $_{0}$n UO_2 Pellet Surfaces in Air at 229 to 275°C." J. Nucl. Mater. 88:153-160.

Thomas, L. E., J. M. McCarthy, and E. R. Gilbert. 1986a. "TEM Examination of Oxidized Spent Fuel." In Proceedings of the Third International Spent Fuel Storage Technology Symposium/Workshop, Vol. 2, CONF-860417, U.S. Department of Energy, Seattle, Washington.

Thomas, L. E., J. M. McCarthy, and E. R. Gilbert. 1986b. "Transmission Electron Microscopy of Oxidized UO_2 Spent Fuel." In Proceedings of the 44th Annual Meeting of the Electron Microscopy Society of America, April 14-18, San Francisco, California.

Thomas, L. E., and R. J. Guenther. 1989. "Characterization of Low Gas Release LWR Fuels by Transmission Electron Microscopy." In Proceedings of the Material Research Society Symposium. Vol. 27, pp. 293-300.

Thomas, L. E., R. E. Einziger, and R. E. Woodley. 1989. "Microstructural Examination of Oxidized PWR Spent Fuel by Transmission Electron Microscopy." J. Nucl. Mater. 166:243-251.

Thornhill, C. K., T. K. Campbell and R. E. Thornhill. 1988. Storage of Spent Fuel in Air, Volume 1 - Design and Operation of a Spent Fuel Testing Facility. PNL-6640, Vol. 1, Pacific Northwest Laboratory, Richland, Washington.

Weigel, F., and H. R. Hoekstra. 1986. "Compounds of Uranium." In The Chemistry of the Actinide Elements, 2nd ed. Vol. 1. eds. Katz, J.G.T. Seaborg, and L. R. Morss, pp. 256-289. Chapman and Hall, London, New York.

Westrum, Jr., E. F., and F. Gronvold. 1962. "Triuranium Heptaoxides: Heat Capacities and Thermodynamic Properties of α- and β-U_3O_7 from 5 to 350°K." J. Phys. Chem. Solids. 23:39-53.

White, G. D., and E. R. Gilbert. 1986. "Comparison of the Oxidation Behavior of BNL, CRNL, and PNL UO_2 Pellets." In Proceedings of the Third International Spent Fuel Storage Technology Symposium/Workshop, CONF-860417, U.S. Department of Energy, Seattle, Washington.

White, G. D., C. A. Knox, E. R. Gilbert, and A. B. Johnson, Jr. 1983. "Oxidation of UO_2 at 150-350°C." In Proceedings of the U.S. Nuclear Regulatory Commission Workshop on Spent Fuel/Cladding Reaction During Dry Storage, NUREG/CP-0049, pp. 102-110, U.S. Nuclear Regulatory Commission, Gaithersburg, Maryland.

APPENDIX A

REFERENCE X-RAY DIFFRACTION PATTERNS

APPENDIX A

REFERENCE X-RAY DIFFRACTION PATTERNS

To aid identification of uranium oxides and uranium oxide hydrates formed by oxidation of UO_2 or spent UO_2 fuel, reference X-ray diffraction patterns from the JCPDS database (JCPDS 1988) are plotted in Figures A.1, A.2 and A.3. The patterns indicate the intensities of the X-ray peaks as a function of diffraction angles (for copper K_α X-rays) of lattice interplanar spacings (d-spacings). By overlaying these "stick figure" patterns with experimental patterns having the same horizontal scales of diffraction angles, the individual phases in phase mixtures can be readily identified.

In Figure A.1, the numerous (36) reference diffraction patterns from uranium oxides are grouped by pattern similarities. Most of the uranium oxides have one of two structure types: the UO_2-based fluorite structure or the α-U_3O_8 structure. Patterns from high-pressure phases (marked with a "*") are included for completeness but may be disregarded for matching U-O phases formed at 1-atm pressure.

In Figure A.2, the patterns for U_3O_7-type phases are shown for the angular range of 46 to 60° 2θ most useful for distinguishing the various fluorite-structure phases. Patterns in Figures A.1 and A.3 are plotted over the full angular range of data acquisition in general XRD work, 3 to 80° 2θ.

For the U-O phases observed in oxidized fuels, the best JCPDS card matches were Nos. 5-550 for UO_2, 20-1344 for U_4O_9 (the lattice parameter of experimentally observed U_4O_9 was slightly larger than the reference value), 15-4 for α-U_3O_7, 24-1172 for α-U_3O_8, and 13-407 for $UO_3 \cdot 2H_2O$ (schoepite).

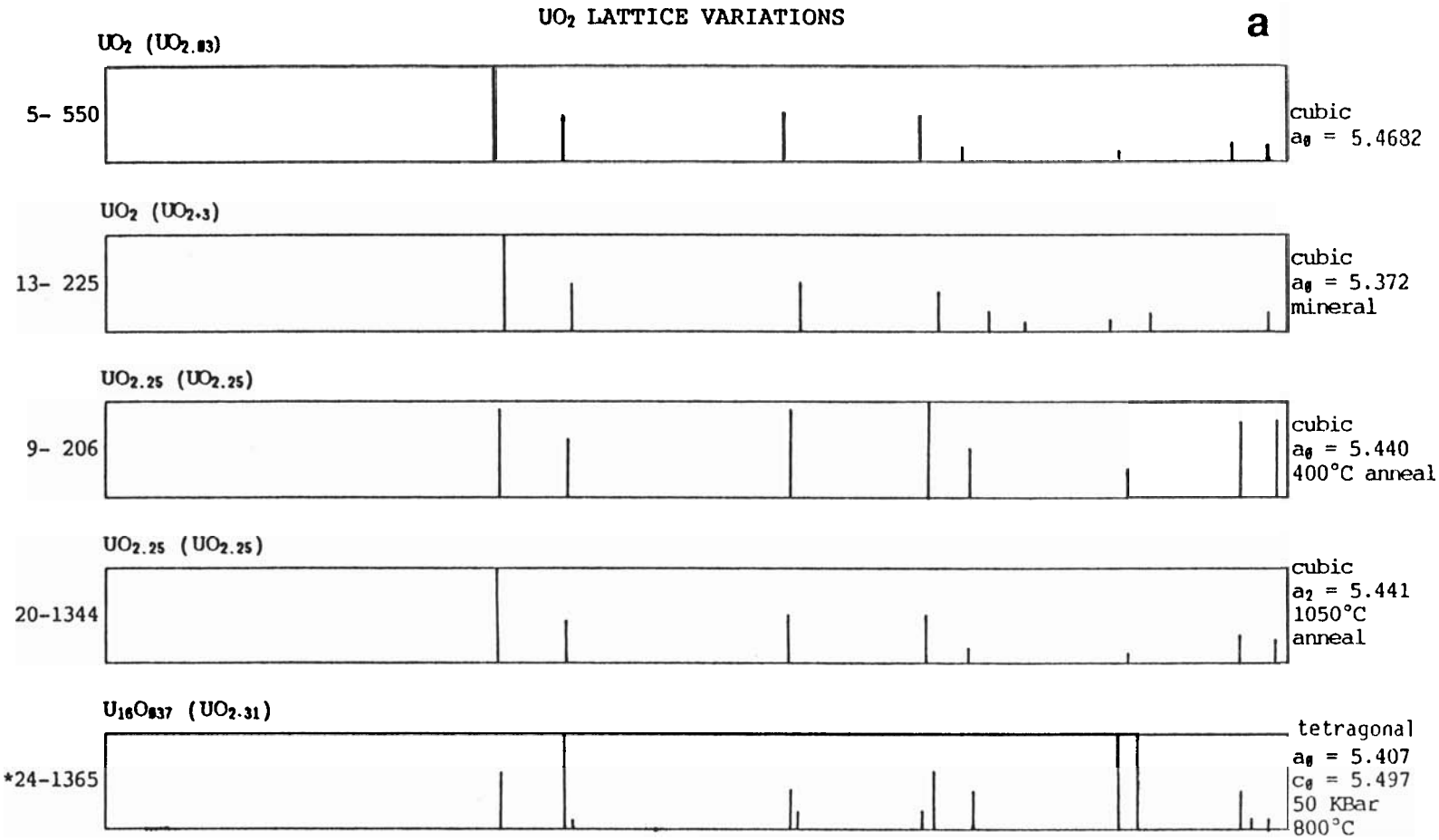

* indicates high pressure phase

FIGURE A.1. Reference X-Ray Diffraction Patterns for Uranium Oxides. Diffracted intensity vs diffraction angles from 3 to 83° 2θ. From JCPDS database (JCPDS 1988).

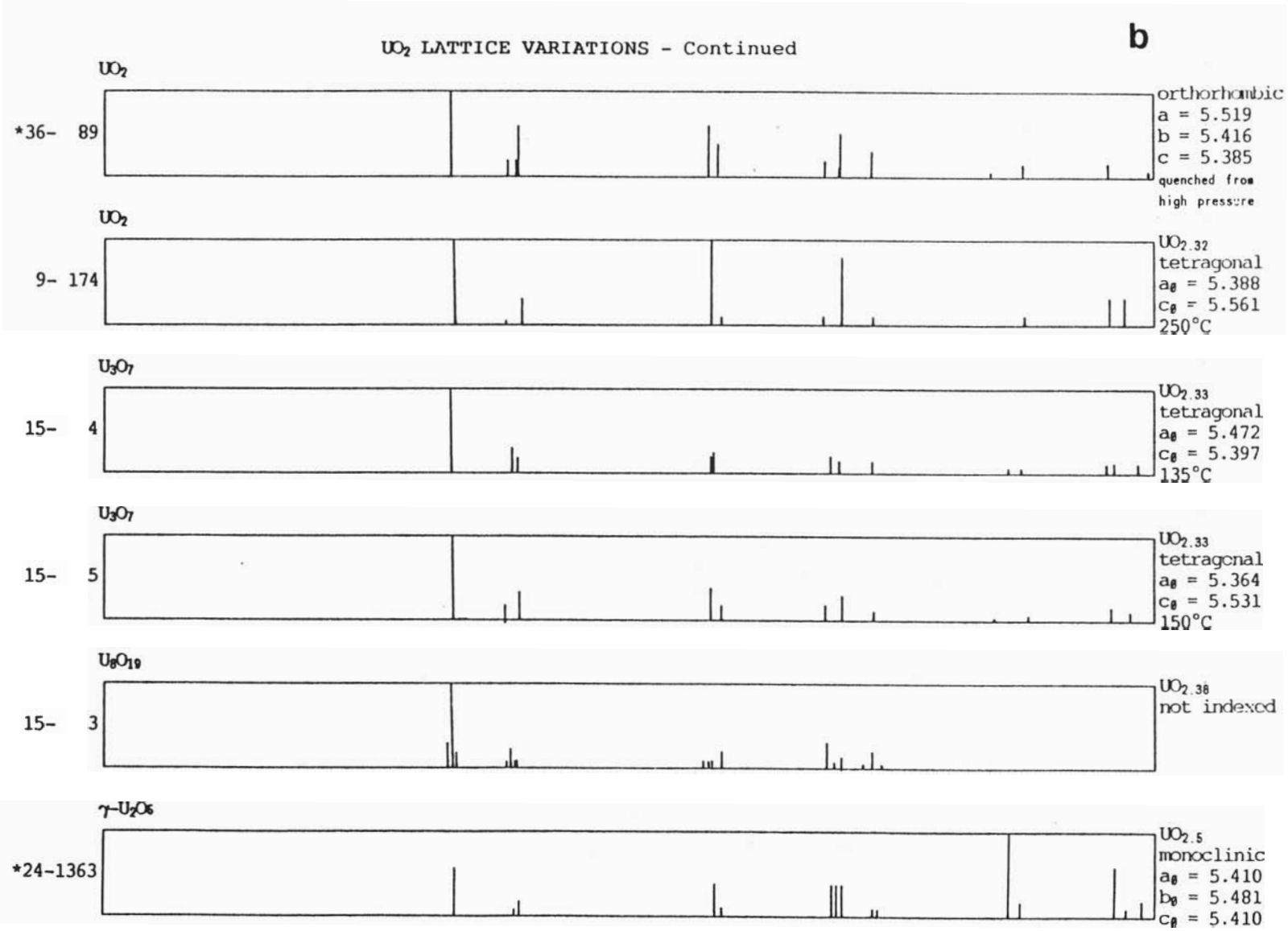

FIGURE A.1 (contd)

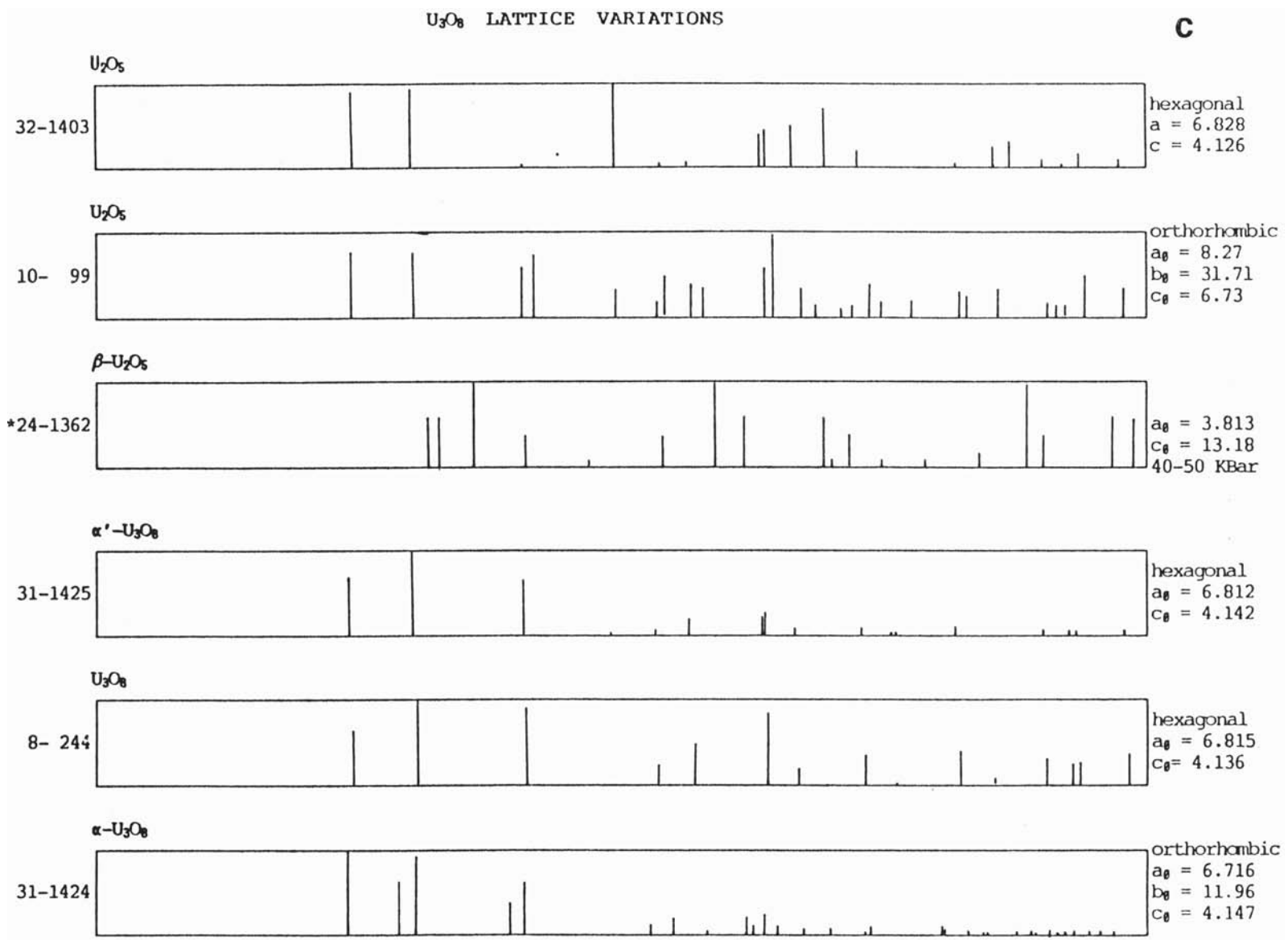

FIGURE A.1. (contd)

U_3O_8 (Continued)

d

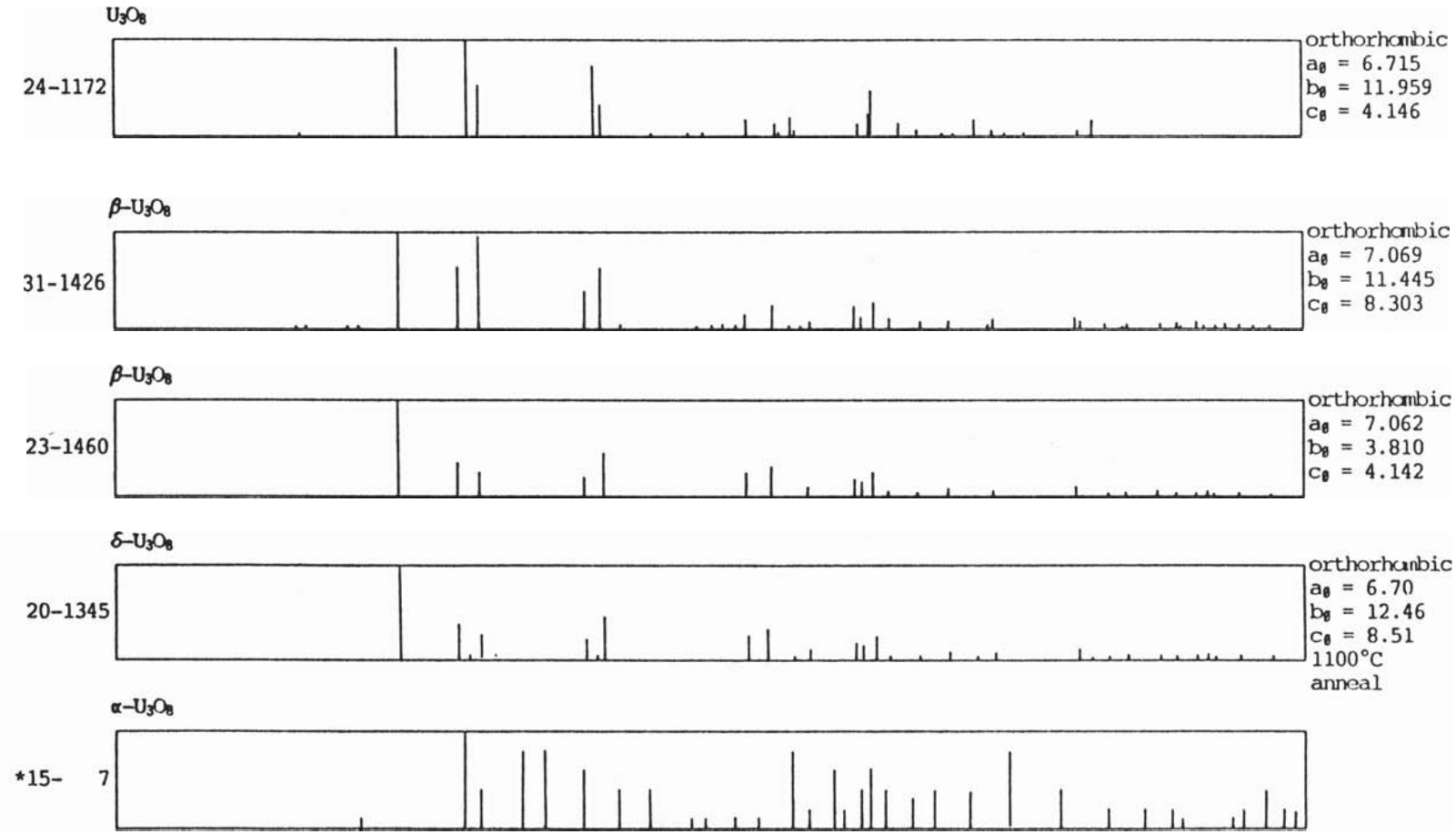

FIGURE A.1 (contd)

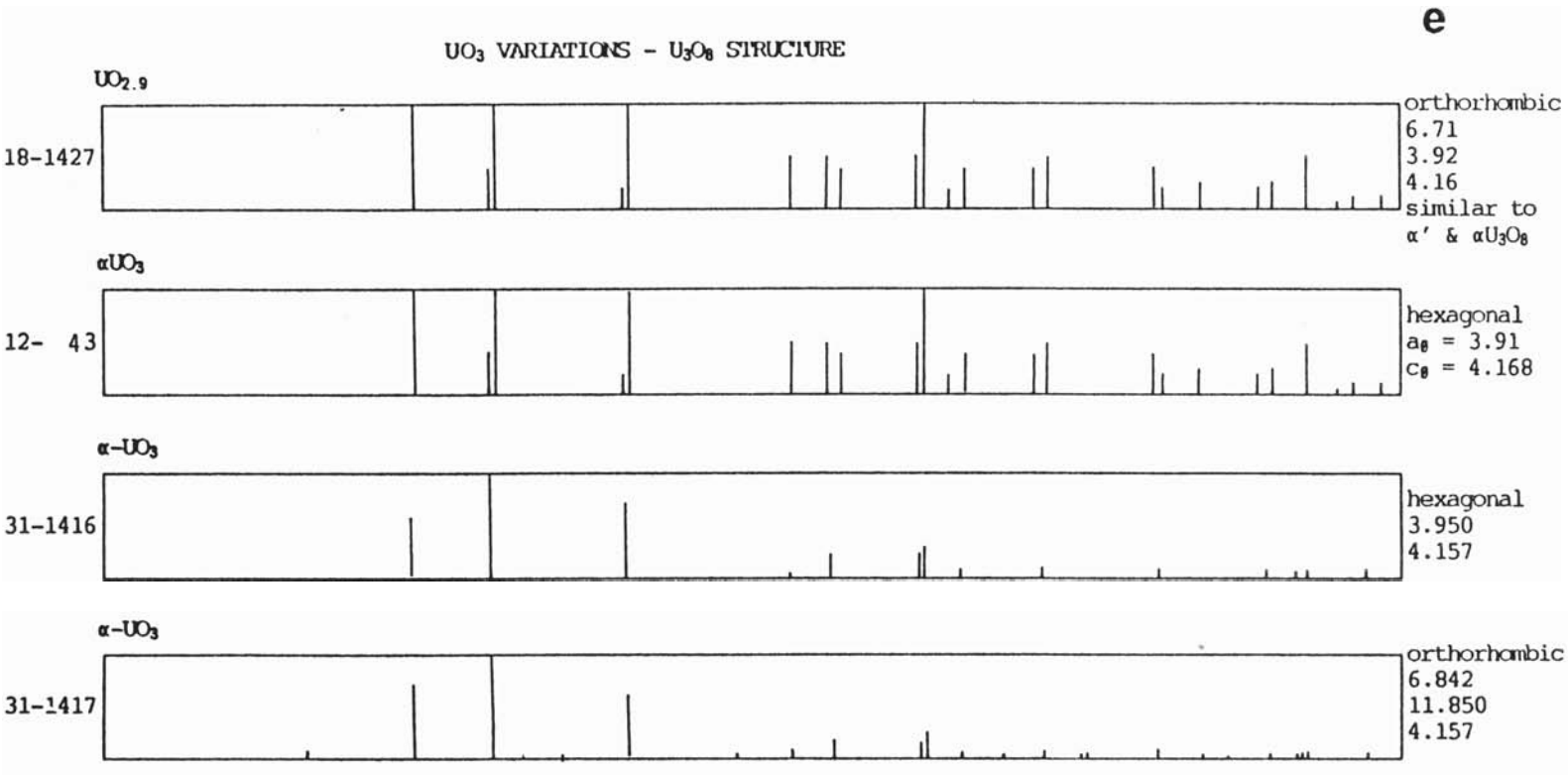

18-1428 β-UO_3 Similar to 31-1418 and 22-1079

FIGURE A.1 (contd)

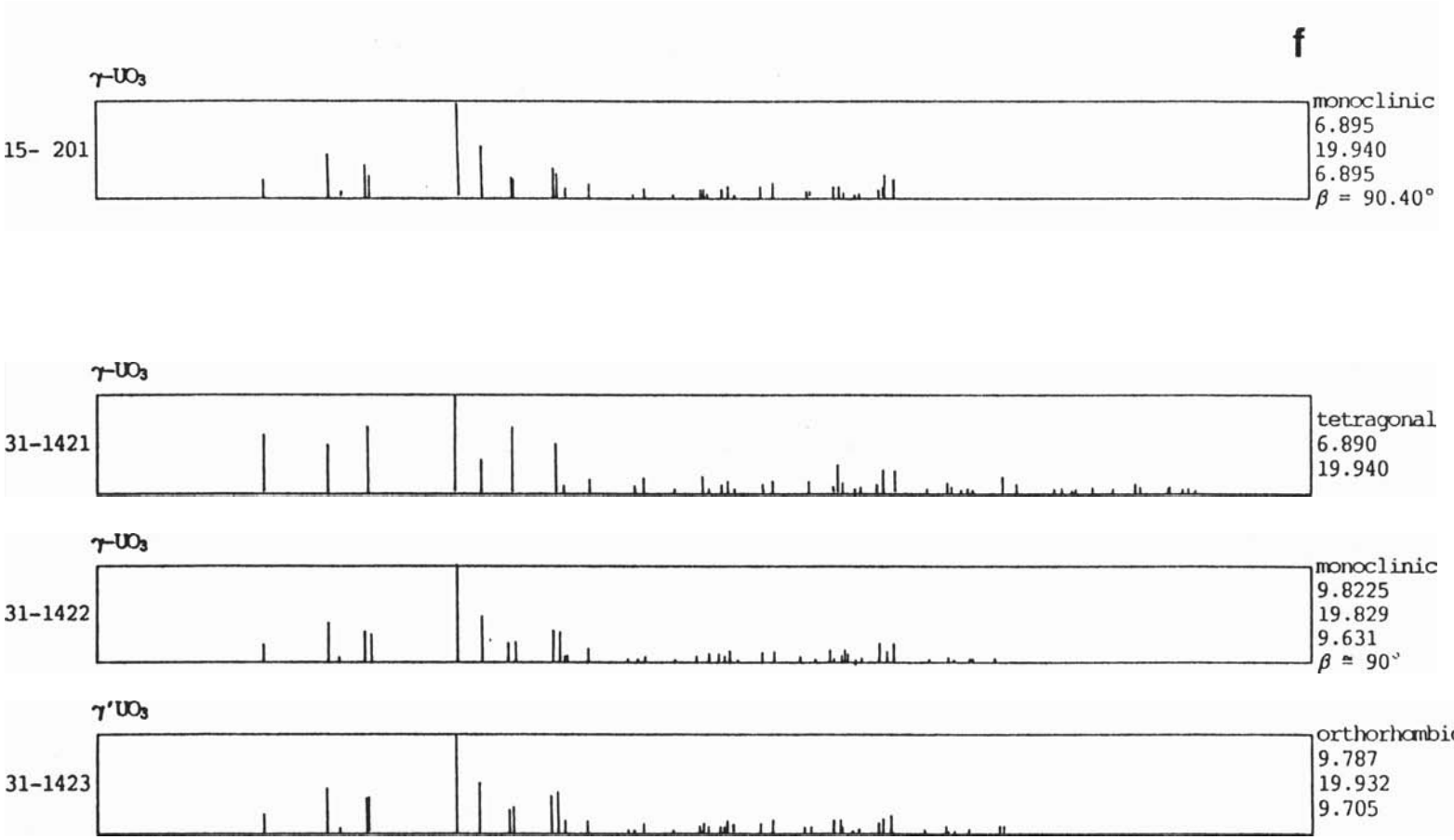

FIGURE A.1. (contd)

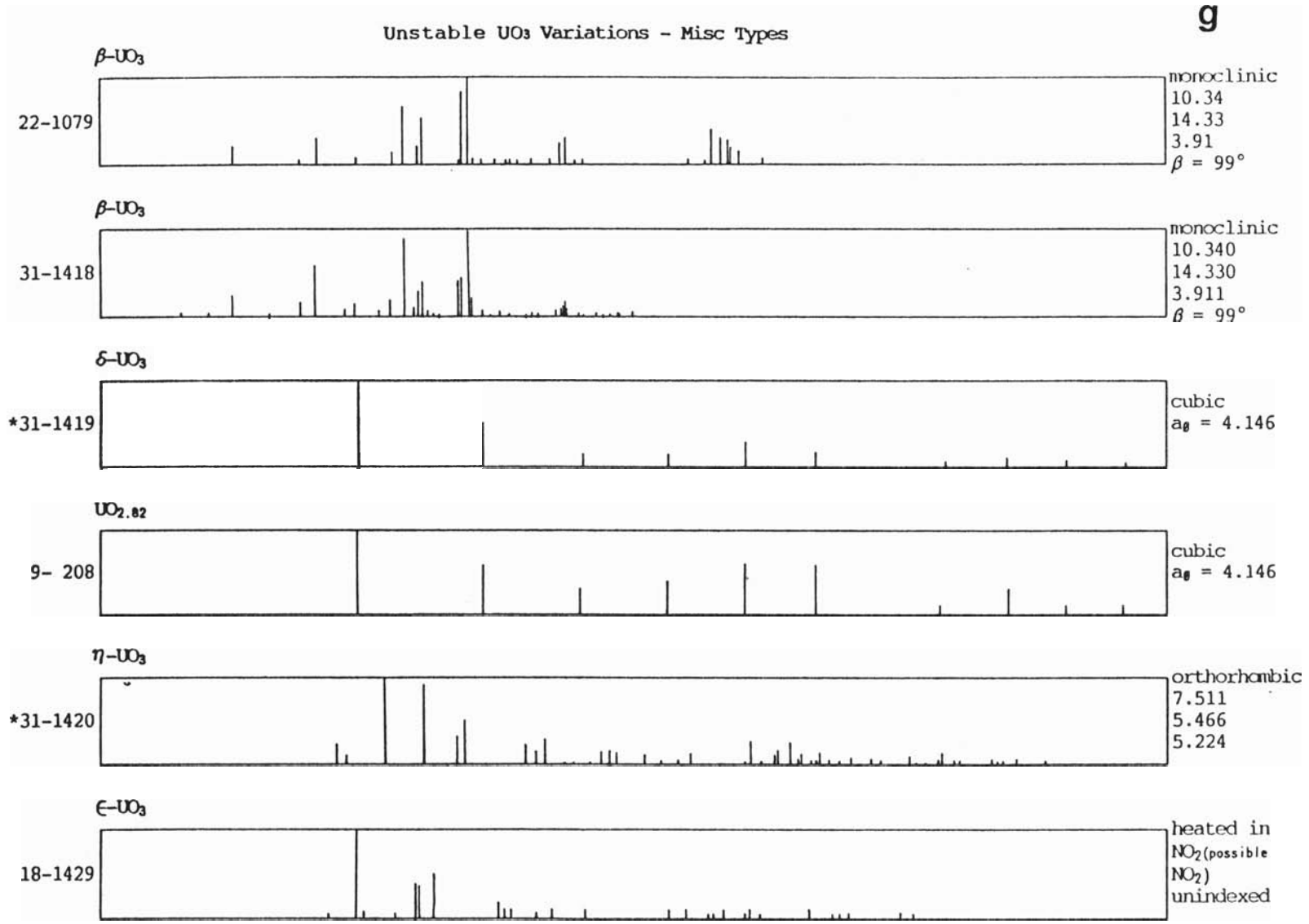

FIGURE A.1 (contd)

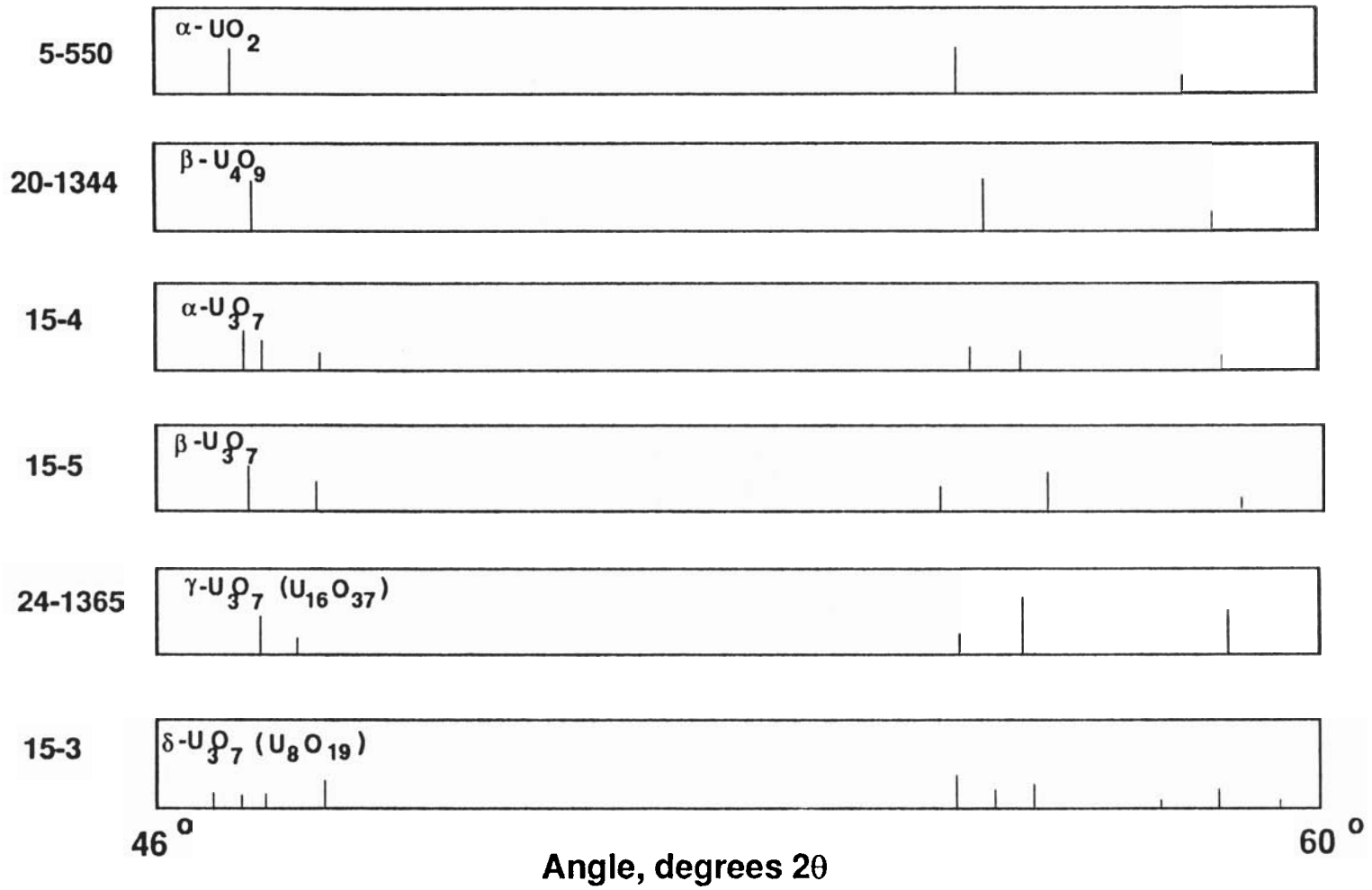

FIGURE A.2. Reference X-Ray Diffraction Patterns for U_3O_7 Phases. Diffracted intensity vs diffraction angles from 46 to 60248 2θ. From JCPDS database (JCPDS 1988).

SCHOEPITE VARIATIONS

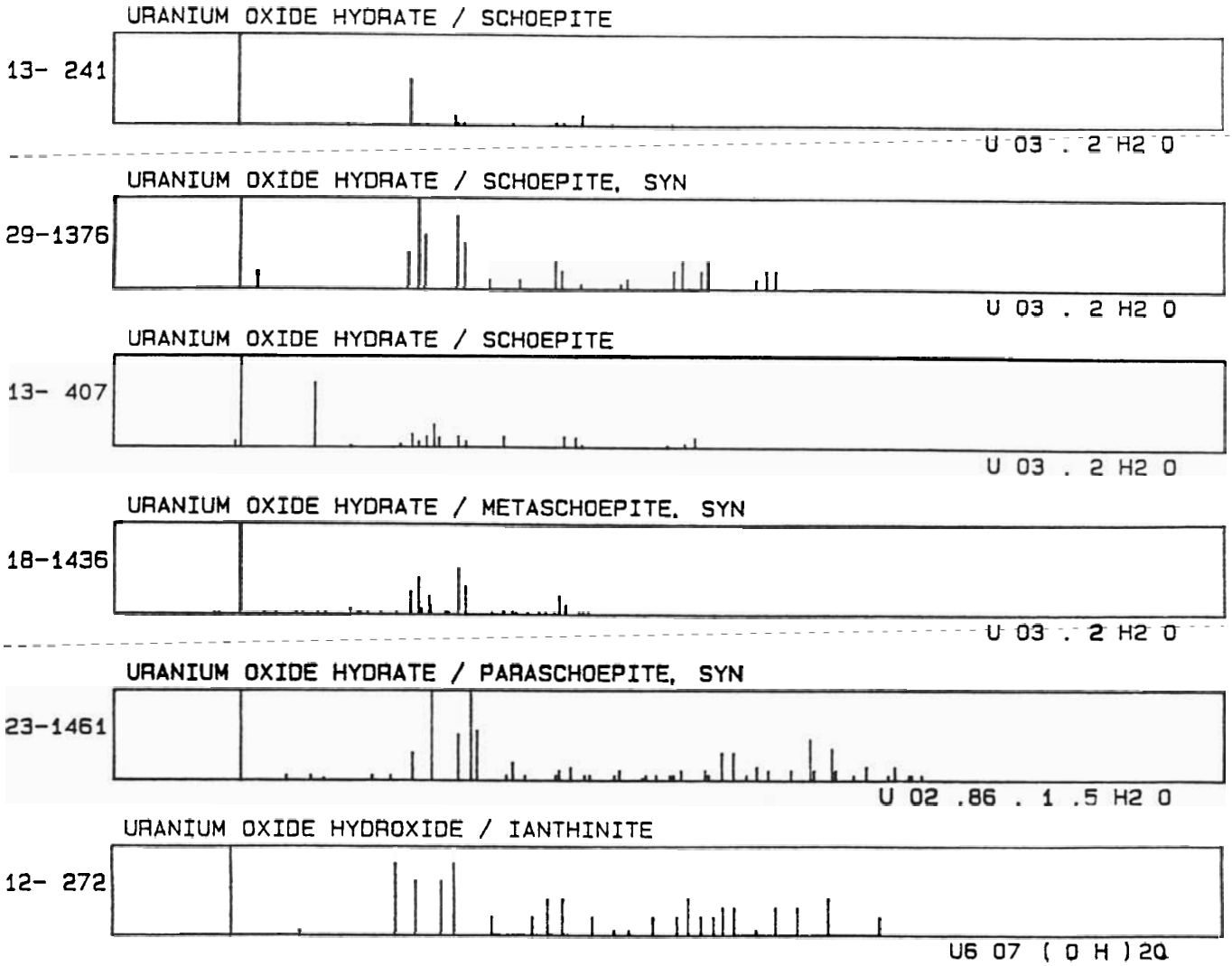

Note: 13-407 is a mixture of schoepite and dehydrated schoepite--α-$UO_2(OH)_2$.

FIGURE A.3. Reference X-Ray Diffraction Patterns for Uranium Oxide Hydrates. Diffracted intensity vs diffraction angles from 3 to 83° 2θ. From JCPDS database (JCPDS 1988).

NAMED $UO_3 \cdot H_2O$ VARIATIONS

α-$UO_2 \cdot (OH)_2$ (Dehydrated Schoepite)

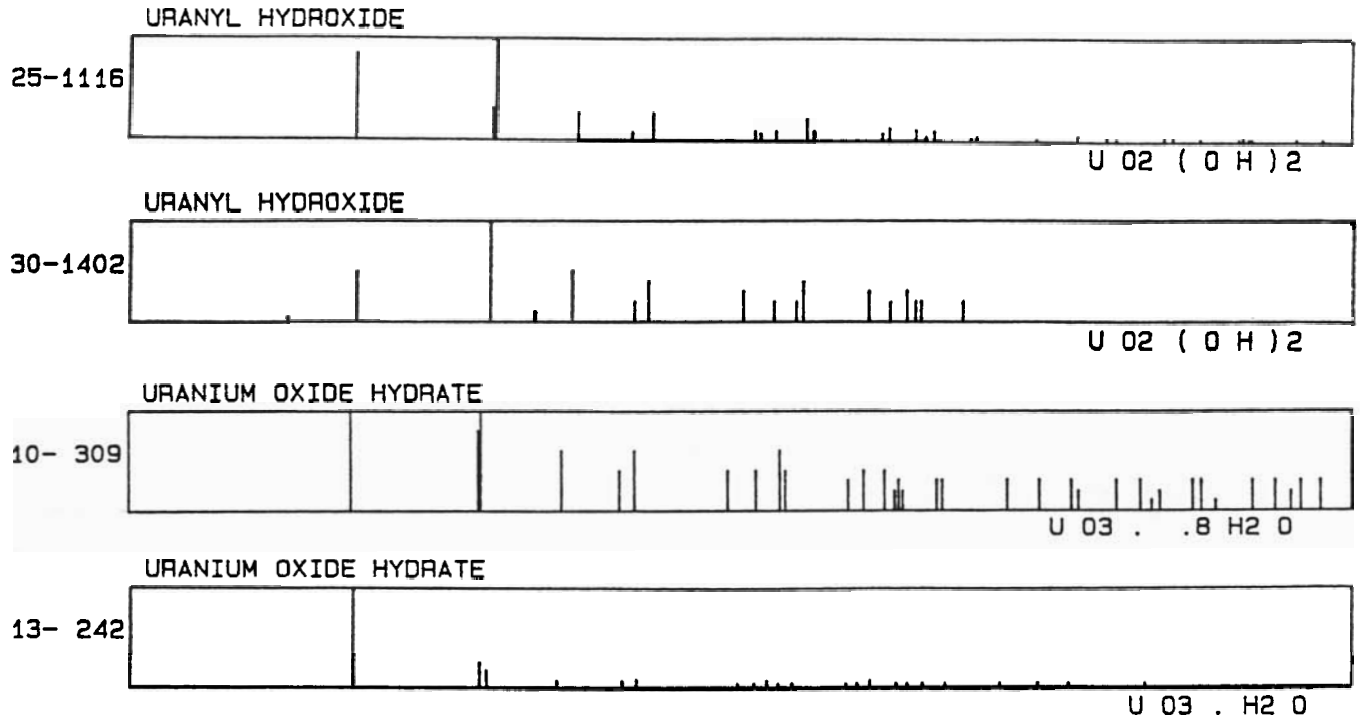

β-$UO_2 \cdot (OH)_2$

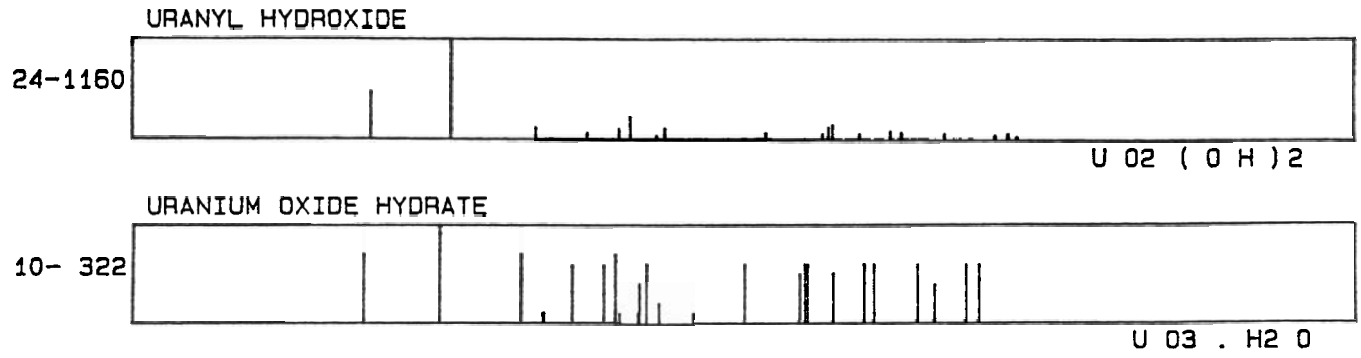

γ-$UO_2 \cdot (OH)_2$

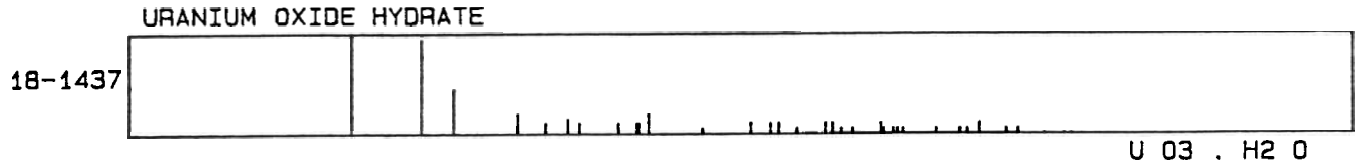

FIGURE A.3. (contd)

PEROXIDES

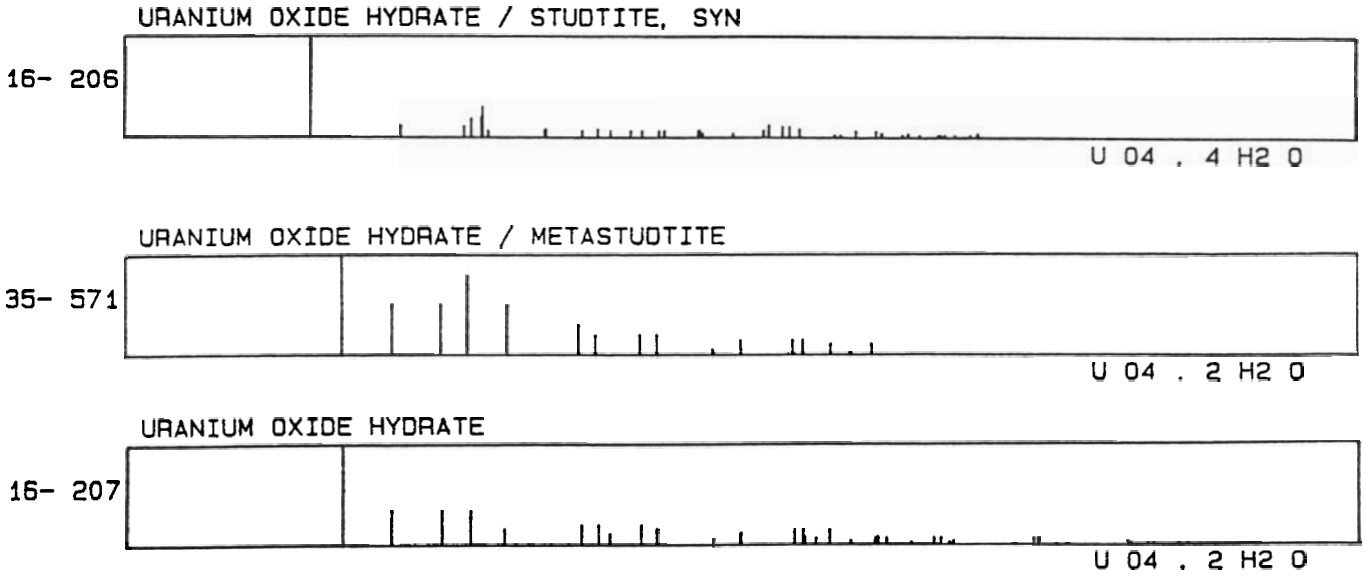

OTHER HYDROXIDE HYDRATES

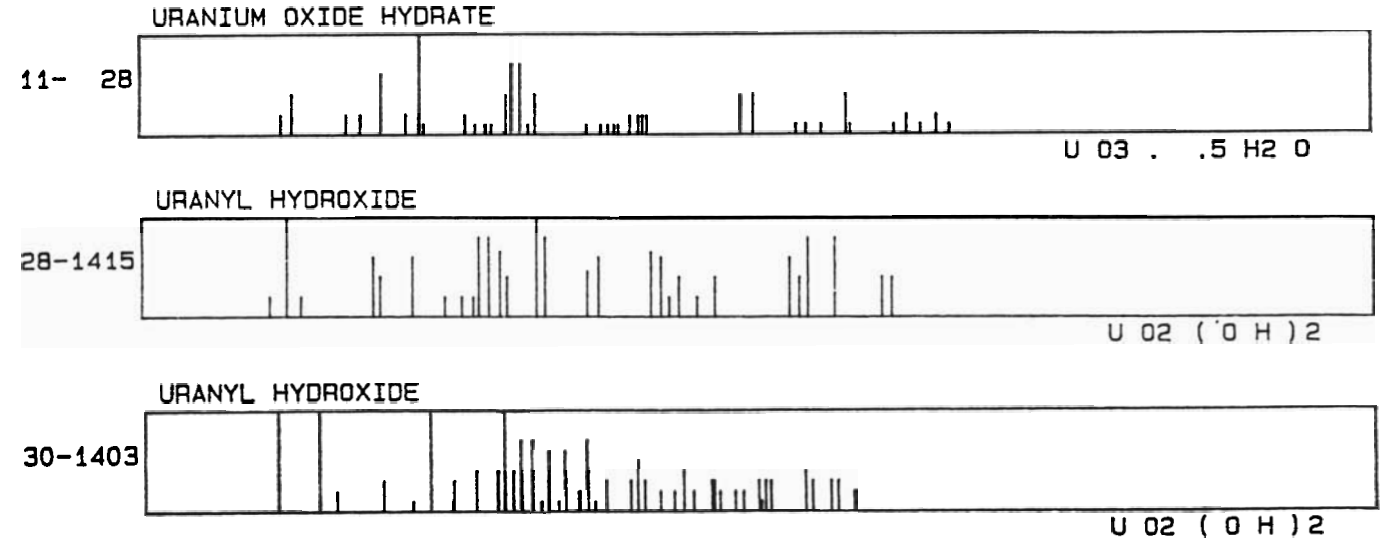

FIGURE A.3. (contd)

OTHER HYDROXIDE HYDRATES

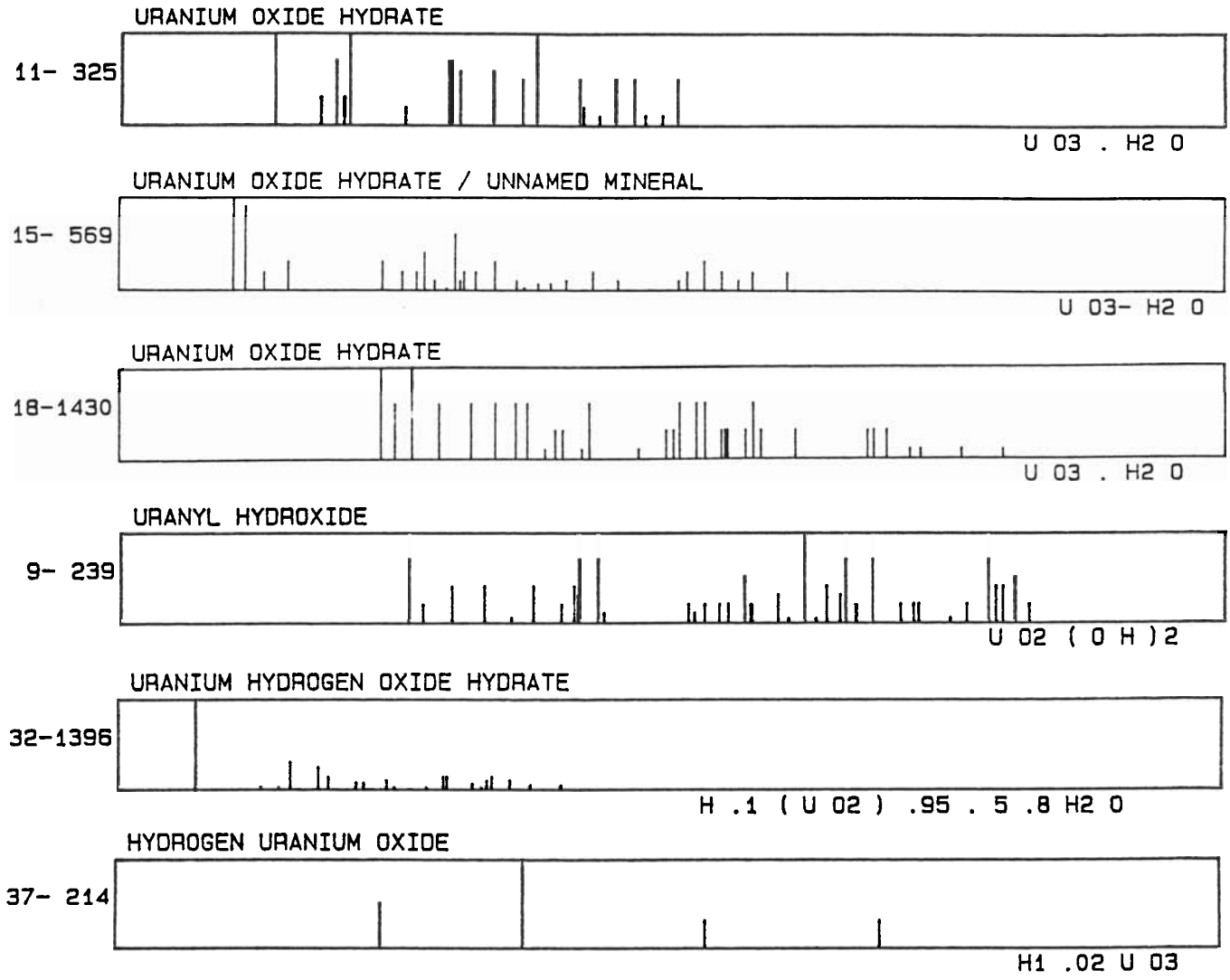

FIGURE A.3. (contd)

APPENDIX B

CRYSTALLOGRAPHIC DATA FOR URANIUM OXIDES AND URANIUM OXIDE HYDRATES

APPENDIX B

CRYSTALLOGRAPHIC DATA FOR URANIUM OXIDES AND URANIUM OXIDE HYDRATES

The exact phases formed between UO_2 and UO_3 are strongly dependent on experimental variables. Many of these phases are metastable and are sensitive to the nature of the starting materials and oxidation conditions. Table B.1 gives crystallographic and density information for the commonly identified polymorphs. The following describes these phases and their conditions of formation from nonirradiated material.

UO_2-UO_{2+x}: The range of oxygen solubility in UO_2 increases rapidly with increasing temperatures above about 400°C. At the oxidation test temperatures in this work, oxygen solubility in UO_2 is negligible.

U_4O_9: Three polymorphs of U_4O_9 have been identified, all of which are cubic and based on a superstructure of the UO_2 lattice. In β-U_4O_9, the usual variant, the excess oxygen is fully ordered to form a superlattice with four times the UO_2 lattice dimensions. The superlattice reflections are now always observable on X-ray diffraction patterns, and seem to occur only from carefully annealed samples. When present, the ordering is easily detectable by electron diffraction. Heating the β phase above about 500°C sometimes forms γ-U_4O_9, which has a partially disordered structure and gives characteristic diffuse scattering reflections in electron diffraction. The stability region for the γ form is not well established. Another variant, α-U_4O_9, forms from the β phase below 65°C.

U_3O_7: At least four polymorphs are identified, all of questionable stability. These are α-U_3O_7 (tetragonal, c/a - 0.986), β-U_3O_7 (tetragonal, c/a = 1.031), γ-U_3O_7 or $U_{16}O_{37}$ (tetragonal, c/a = 1.017), and δ-U_3O_7 or U_8O_{19} (monoclinic, b/a = 1.034, α = 90.29°). γ and δ-U_3O_7 are high pressure phases formed at 16 to 60 kbar, but both have been reported at normal pressures (Westrum and Gronvold 1962). α-U_3O_7 has been prepared by oxidizing UO_2

TABLE B.1. Characteristics of Uranium Oxide Phases

Structure Type	Formula	O/M Ratio	Symmetry	Lattice Parameters, nm a_o	b_o	c_o		Density, g/cm^3 Exper.	X-ray
UO_2	UO_2	2.0	fcc	0.5470	-	-	-	10.95	10.964
U_4O_9	β-U_4O_9	2.20-2.25	cubic	4 x 0.544	-	-	-	-	11.299
U_3O_7	α-U_3O_7	2.27-2.33	tetr.	0.5472	-	0.5397	c/a = 0.989	-	-
	β-U_3O_7	2.33-2.34	tetr.	0.5364	-	0.5531	c/a = 1.031	11.17	-
	γ-U_3O_7* ($U_{16}O_{37}$)	2.31	tetr.	5.407	-	0.5497	c/a = 1.017	-	11.366
	δ-U_3O_7* (U_8O_{19})	2.37	mono.	0.5378	0.5559	0.5378	β = 90.29°	11.34	11.402
	γ-U_2O_5*	2.5	mono.	0.5410	0.5481	0.5410	β = 90.49°	10.36	11.51
	β-U_2O_5*	2.5	hex.	0.3813	-	1.318	-	10.76	11.15
U_3O_8	α-U_2O_5	2.5	hex.	0.6828	-	0.4126	-	-	-
	U_8O_{21} (U_3O_{8-x})		ortho.	0.7796	8 x 0.3958	2 x 0.4145	-	-	8.341
	α-U_3O_8	2.67	ortho.	0.7796	3 x 0.3987	0.4147	-	-	8.395
	β-U_3O_8	2.67	ortho.	0.7062	0.3810	0.4142	-	-	8.326
	α-UO_3	3.0	ortho.	0.684	11 x 0.395	0.4157	-	7.3	7.3
UO_3	A-UO_3	3.0	noncryst.	-	-	-	-	6.8	-
	γ-UO_3	3.0	ortho.	0.9813	1.993	0.9711	-	7.80	8.00
	β-UO_3	3.0	mono.	1.034	1.433	0.3910	β = 99.03°	8.25	8.3
	δ-UO_3	3.0	cubic	0.416	-	-	-	6.69	6.60
	ε-UO_3	3.0	tricl.	0.4002	0.3841	0.4165	α = 98.10° β = 90.20° γ =120.2°	8.54	8.67
	η-UO_3	3.0	ortho.	7.511	5.466	5.224		8.62	8.86

* High-pressure phases

Note: Structurally similar U_3O_8 phases may have hexagonal or orthorhombic symmetry

References: Weigel and Hoekstra, 1986; Keller, 1973; Westrum and Gronvold, 1962; Hoekstra, Siegel and Gallagher, 1970.

powder in air at 135°C, and is the most commonly observed mineral form (Smith 1984). β-U_3O_7 is the commonly observed form produced by oxidizing UO_2 in air at 150 to 275°C.

Besides the usual U_3O_7 phases, other distorted-fluorite-structure phases have been formed at high pressures. γ-U_2O_5 and an unnamed orthorhombic phase (JCPDS Card No. 36-89) are examples. Based on X-ray diffraction studies and density measurements, another high-pressure phase, β-U_2O_5, appears transitional between fluorite and U_3O_8 structure types. High pressures tend to stabilize the fluorite structure, but the high-pressure phases are not necessarily relevant to the phases formed by oxidizing spent fuel in air.

U_3O_8: Apart from α-U_2O_5, a high-pressure phase of questionable existence at atmospheric pressure, the U_3O_8-structure phases are U_8O_{21} or U_3O_{8-x} (also called U_5O_{13}), α-U_3O_8, α'-U_3O_8, β-U_3O_8, and α-UO_3. β-U_3O_8 is a high-temperature form. Hexagonal and orthorhombic indexing are used (almost interchangeably) for these phases, and comparison of the X-ray patterns shows that the structures are essentially minor variations.

UO_3: One amorphous and six crystalline modifications of UO_3 are known. Data for these phases are included in Table 1. α-UO_3 is a variant of the U_3O_8 structure. γ-UO_3, the stable form shown on most phase diagrams has a different structure type.

Uranium hydrates and peroxides: Crystallographic information and densities of the uranium trioxide hydrates and several uranium peroxides are provided in Table B.2. These phases were reviewed by Hoekstra and Siegel (1973) and Weigel and Hoekstra (1986). Uranium hydrate minerals were reviewed by Smith (1984). Densities for the uranium oxide hydrates are significantly lower than those of the U_3O_8-structure phases of UO_3.

TABLE B.2. Characteristics of the Uranium Trioxide Hydrates and of the Uranium Peroxides

Names	Formula	Symmetry	Lattice Parameters, nm			Angles	Density, g/cm^3	
			a_o	b_o	c_o		Exp.	X-ray
schoepite (schoepite-I)	$UO_3 \cdot 2H_2O$	orth.	1.474	1.666	1.436		5.00	-
metaschoepite (schoepite-II)	$UO_3 \cdot 2H_2O$	orth.	1.473	1.672	1.399			
paraschoepite (schoepite-III)	$UO_3 \cdot 2H_2O$	orth.	1.522	1.683	1.412			
dehydrated schoepite α-$UO_2(OH)_2$	$UO_2(OH)_2$ ($UO_3 \cdot xH_2O$) x=0.8 to 1.0	orth.	0.424 to 0.430	1.030 to 1.019	0.686 to 0.692		6.63 to 6.71	6.73
β-$UO_2(OH)_2$	$UO_2(OH)_2$ ($UO_3 \cdot H_2O$)	orth.	0.564	0.629	0.994		5.73	
γ-$UO_2(OH)_2$	$UO_2(OH)_2$ ($UO_3 \cdot H_2O$)	mono.	0.642	0.552	0.556	β=112°77'	5.55	5.56
unnamed	$H_2U_3O_{10}$ $UO_{2.86} \cdot 0.5H_2O$ x=0.3 or 0.5	tricl.	0.682	0.742	0.556	α=108.5 β=125.5 γ=88.2	6.7	6.85
studtite	$UO_4 \cdot 4H_2O$	mono.	1.18	0.680	0.425	β=93°51'	5.15	
metastudtite	$UO_4 \cdot 2H_2O$	orth.	0.651	0.878	0.4211	-		
ianthinite	$UO_2 \cdot 5UO_3 \cdot 10H_2O$	orth.	1.152	3.03	7.15			

References: Weigel and Hoekstra,1986; Smith, 1984; Hoekstra and Siegel, 1973.

APPENDIX C

ANALYTICAL INSTRUMENTS AND METHODS

APPENDIX C

ANALYTICAL INSTRUMENTS AND METHODS

Described in this Appendix are the equipment, analytical methods used in examining the spent fuel, and the information obtained from each method. Although there is some overlap between methods, each analytical method provides a different type of information related to material structure and composition, and each requires different sample preparation techniques. The analytical methods used were transmission electron microscopy (TEM), scanning electron microscopy (SEM), scanning Auger microscopy (SAM), and X-ray diffraction (XRD). Three of the methods, TEM, SEM, and SAM, use finely focused electron beams in a high vacuum environment to examine the sample at high magnifications and to obtain crystallographic or chemical information from very small volumes or surface areas of the sample. X-ray diffraction, on the other hand, is a bulk analysis method used primarily to identify the phases in relatively large volumes of sample material. The instruments and operating parameters are described in Table C.1.

TEM

Transmission electron microscopy is used to examine and analyze on a fine scale the microstructure, crystalline phases, and defects present in solids. This is accomplished by transmitting a beam of relatively high energy (100-200 keV) electrons through a very thin section of sample (<150 mn thick) to form an image of the internal structure of the material. The image resolution in the TEM can approach the atomic level--it is possible, for example to directly image crystalline lattice planes. In the usual diffraction contrast imaging mode, the best microstructural resolution is typically 0.3 to 0.5 nm. When operated in the electron diffraction mode, the TEM provides an electron diffraction pattern of the sample area, allowing determination of crystalline structures and identification of crystalline phases. Most diffraction is done in the selected-area mode, which provides sample areas as small as about 0.5 μm in diameter. For diffraction analyses

TABLE C.1. Analytical Instruments and Operating Parameters

Instrument: Transmission Electron Microscope
Manufacturer and Model: JEOL 2000FX
Beam Energy: 200 keV
Modifications: Si(Li) solid-state X-ray detector and computer-based multichannel analyzer (Tracor Northern 5500 Series II)

Instrument: Scanning Electron Microscope
Manufacturer and Model: JEOL 35C
Beam Energy: 15-25 keV
Modifications: Microscope column enclosed in movable lead shielding to allow examination of highly radioactive samples.

Instrument: High Resolution Scanning Auger Microprobe
Manufacturer and Model: Perkin Elmer PHI Model 660
Beam Energy and Current: Typically 20 keV at 25 nA
Modifications: Microprobe and high vacuum equipment enclosed in movable lead shielding to allow examination of highly radioactive samples. Facility for in situ fracturing of sample particles in ancillary vacuum chamber.

Instrument: X-Ray Powder Diffractometer
Manufacturer and Model: Scintag
Beam Characteristics: Cu-K X-rays
Modifications: Peltier-cooled solid-state (Si-Li) X-ray detector with tantalum-shielded entrance slit.

NOTE: Manufacturers and models of the major analytical instruments used in this work are indicated above as a means of implicitly indicating the operational performance characteristics of the instruments. These listings should not be construed as product endorsements.

of very small features (<10 nm), microbeam diffraction methods are used. The TEM can also provide elemental composition data using energy-dispersive X-ray spectrometry (EDS), where the energy spectra of X-rays emitted by the beam/sample interaction are analyzed. In this work, EDS was used only to help identify fission product phases in the fuel samples.

SEM

Scanning electron microscopy is used primarily to reveal the topography and gross microstructure of surfaces; e.g., particle or grain size and shape,

structure of fracture surfaces, and oxide scale structure). SEM images of surfaces offer much greater resolution and depth of field than optical microscopes. In SEM, a focused 15-35 keV electron beam scans the sample surface, and an image is formed from backscattered electrons or from secondary electrons. Contrast is created by local changes in sample surface orientation, texture, and electrical characteristics, and by differences in average atomic number. Elemental analysis can be performed in the SEM using the EDS technique described above, but was not used in this work.

SAM

Scanning Auger microscopy is used primarily for compositional analysis of surfaces. This technique is in some ways similar to SEM in that the sample surface is scanned by a moderately energetic electron beam (3-20 keV). For compositional or microchemical analysis, the electrons emitted by the Auger emission process (Briggs and Seah 1983) are collected and analyzed. The SAM can also be used in an SEM imaging mode by collecting secondary electrons, and this mode is generally used to locate a region for analysis. Unlike SEM, SAM is a true surface analysis technique because the Auger electrons that are detected are emitted by only the first few atomic layers of the solid. Each element produces a different Auger electron energy spectrum, hence analysis of the Auger electron energy spectra can be used to determine surface composition. While elemental analysis is the primary operational mode of the SAM, Auger electron spectroscopy can also infer information on surface chemistry. Changes in bonding due to different oxidation states of an element can alter the energy spectrum of electrons emitted by an element, providing a means to distinguish different oxide phases. Because Auger electrons are emitted only from the near-surface, information can be obtained as a function of depth by performing SAM analysis while simultaneously eroding the surface by sputtering or ion beam milling. In principle, SAM could then be used to detect and characterize thin layers of higher oxides forming on the spent UO_2 fragments and particles.

XRD

X-ray powder diffractometry is used for identifying crystalline phases present in relatively large samples. In the powder diffraction technique used here, sample powders covering a surface area ~2 cm^2 by 1-3 μm deep were scanned with a collimated, X-ray beam in a diffractometer and the scattered X-rays were detected with a solid-state energy-dispersive detector. In crystalline materials, some of the incident X-rays are diffracted at discrete angles. The X-ray detector coupled with data reduction instrumentation produces a spectrum of X-ray intensity as a function of diffraction angle. From this spectrum, the lattice spacings can be determined directly using a simple equation (the Bragg equation) that relates the location (diffraction angle) of a given peak to the lattice spacing. From symmetry considerations, the presence or absence of certain peaks among a set of peaks provides information on the type(s) of crystals producing the spectrum, allowing phase identification. In practice, phase identification is usually made by comparing an "unknown" diffraction spectrum with reference spectra from known phases, e.g., the JCPDS Powder Diffraction Files (JCPDS 1988).

DISTRIBUTION

No. of Copies

OFFSITE

12 DOE/Office of Scientific and Technical Information

R. Stein
Office of Civilian Radioactive Waste Management
U.S. Department of Energy
RW-30
Washington, DC 20585

T. Nguyen
Office of Civilian Radioactive Waste Management
U.S. Department of Energy
RW-32
Washington, DC 20585

W. Danker
Office of Civilian Radioactive Waste Management
U.S. Department of Energy
RW-33
Washington, DC 20585

K. A. Klein
Office of Civilian Radioactive Waste Management
U.S. Department of Energy
RW-32
Washington, DC 20545

C. Head
Office of Civilian Radioactive Waste Management
U.S. Department of Energy
RW-32
Washington, DC 20545

J. S. Finucane
Energy Information Administration
U.S. Department of Energy
EI-53
Washington, DC 20545

No. of Copies

K. G. Golliher
U.S. Department of Energy
Albuquerque Operations Office
P.O. Box 5400
Albuquerque, NM 87115

S. Mann
U.S. Department of Energy
Chicago Operations Office
Argonne, IL 60439

M. Fisher
U.S. Department of Energy
Idaho Operations Office
785 DOE Place
Idaho Falls, ID 83402

S. T. Hinschberger
U.S. Department of Energy
Idaho Operations Office
785 DOE Place
Idaho Falls, ID 83402

C. Matthews
U.S. Department of Energy
Oak Ridge Operations Office
P.O. Box E
Oak Ridge, TN 37830

C. J. Dankowski
U.S. Department of Energy
Defense Programs
San Francisco Operations Office
1333 Broadway
Oakland, CA 94612

C. P. Gertz
U.S. Department of Energy
Waste Management Project Office
P.O. Box 98518
Las Vegas, NV 89193-8518

No. of Copies

B. A. Chin
Auburn University
Mechanical Engineering Dept.
247 Wilmore Laboratories
Auburn, AL 36830

P. Childress
Babcock & Wilcox Co.
P.O. Box 10935
Lynchburg, VA 24506-0935

L. A. Walton
Babcock & Wilcox Co.
P.O. Box 10935
Lynchburg, VA 24506-0935

P. A. File
Baltimore Gas and Electric Co.
Calvert Cliffs Nuclear Power Plant
Lusby, MO 20657

R. Kohli
Battelle, Columbus Division
505 King Avenue
Columbus, OH 43201

V. Pasupathi
Battelle, Columbus Division
505 King Avenue
Columbus, OH 43201

5 T. W. Wood
Battelle, Pacific Northwest Laboratories
370 L'Enfant Promenade SW
Washington, DC 20024-2115

G. H. Beeman
Battelle, Pacific Northwest Laboratories
370 L'Enfant Promenade SW
Washington, DC 20024-2115

Ralph Zee
Auburn University
Mechanical Engineering Dept.
247 Wilmore Laboratories
Auburn, AL 36830

No. of Copies

J. A. Carr
Battelle, Project Management Division
Office of Nuclear Waste Isolation
505 King Avenue
Columbus, OH 43201

G. A. Townes
BE Inc.
P.O. Box 145
New Ellenton, SC 29809

L. J. Jardine
Lawrence Livermore National Laboratory, L/24
P.O. Box 808
Livermore, CA 94550

G. E. Lucas
University of California
Dept. of Chemical and Nuclear Engineering
Santa Barbara, CA 93106

D. R. Olander
University of California
647 San Fernando Avenue
Berkeley, CA 94707

R. Kunita
Carolina Power & Light Co.
411 Fayetteville St.
P.O. Box 1551
Raleigh, NC 27602

L. Martin
Carolina Power & Light Co.
411 Fayetteville St.
P.O. Box 1551
Raleigh, NC 27602

G. C. Jobson
Chem-Nuclear Systems, Inc.
One Greystone West Building
240 Stoneridge Drive, Suite 100
Columbia, SC 29210

No. of
Copies

C. K. Anderson
Combustion Engineering, Inc.
1000 Prospect Hill Road
Windsor, CT 06095

N. Fuhrman
Combustion Engineering, Inc.
1000 Prospect Hill Road
Windsor, CT 06095

G. P. Wagner
Commonwealth Edison
Nuclear Stations Division
P.O. Box 767
Chicago, IL 60690

T. J. Marz
Consumers Power Company
1945 W. Parnall Road
Jackson, MI 49201

S. J. Raffety
Dairyland Power Coop.
2615 E. Ave. S.
LaCrosse, WI 54601

R. W. Rasmussen
Duke Power Company
P.O. Box 33189
Charlotte, NC 28242

Ebasco Services, Inc.
Two World Trade Center
New York, NY 10098

R. Stanford
Edison Electric Institute
1111 19th St., NW
Washington, DC 20036

R. Maughan
EG&G Idaho, Inc.
P.O. Box 1625
Idaho Falls, ID 83415

R. W. Lambert
Electric Power Research
Institute
P.O. Box 10412
Palo Alto, CA 94304

No. of
Copies

R. F. Williams
Electric Power Research
Institute
P.O. Box 10412
Palo Alto, CA 94304

G. T. Zamry
Florida Power & Light Co.
9250 W. Flagler St.
Miami, FL 33174

FLUOR Engineers, Inc.
Advanced Technology Division
P.O. Box C-11944
Santa Ana, CA 92711-1944

B. K. Agarwal
FW Energy Applications, Inc.
110 Orange Avenue
Livingston, NJ 07039

E. Engles
General Electric Co.
Morris Operation
Morris, IL 60450

W. L. Dobson
Gilbert Associates, Inc.
P.O. Box 1498
Reading, PA 19603

V. J. Barnhart
GNSI
135 Darling Dr.
Avon, CT 06001

B. Handly
Houston Lighting & Power Co.
Nuclear Fuels-SPII
12301 Kurland Dr.
Houston, TX 77034

E. R. Johnson
E. R. Johnson Associates, Inc.
11702 Bowman Green Drive
Reston, VA 22090

J. A. McBride
E. R. Johnson Associates, Inc.
11702 Bowman Green Drive
Reston, VA 22090

No. of
Copies

L. M. Trosten
LeBoeuf, Lamb, Leiby, & MacRae
1333 New Hampshire Ave. NW
Washington, DC 20036

L. B. Ballou
Lawrence Livermore National
Laboratory
P.O. Box 808
Livermore, CA 94550

L. D. Ramspott
Lawrence Livermore National
Laboratory
P.O. Box 808 - MS L404
Livermore, CA 94550

R. Stout
Lawrence Livermore National
Laboratory
Waste Package Tank, NNWSI
P. O. Box 808 - MS L206
Livermore, CA 94550

C. F. Smith
Lawrence Livermore National
Laboratory
P.O. Box 808
Livermore, CA 94550

J. H. Garrity
Maine Yankee Atomic Power Co.
Edison Drive
August, ME 04336

G. D. Whittier
Maine Yankee Atomic Power Co.
Edison Drive
August, ME 04336

R. Whale
Michigan Public Service
Commission
6545 Mercantile Way
Lansing, MI 48909

M. Litterman
Portland General Electric
Trojan Fuel
121 SW Salmon St.
Portland, OR 97204

No. of
Copies

H. F. Shaw
Lawrence Livermore National
Laboratory
Waste Package Task, NNWSI
P.O. Box 808 - MS L206
Livermore, CA 94550

J. Houston
Nuclear Assurance Corp.
5720 Peachtree Parkway
Norcross, GA 30092

C. B. Woodhall
Nuclear Assurance Corp.
5720 Peachtree Parkway
Norcross, GA 30092

J. Clark
Nuclear Fuel Services
6000 Executive Blvd.
Rockville, MD 20852

B. Lehnert
NUTECH Engineers
145 Martinvale Lane
San Jose, CA 95119

G. J. Antonucci
NUS Corporation
910 Clopper Rd.
Gaithersburg, MD 20878

J. V. Massey
Reedy & Associates
15951 Los Gatos Blvd., Suite 1
Los Gatos, CA 95032

J. Van Cleve
Oak Ridge National Laboratory
P.O. Box X
Oak Ridge, TN 37831

M. Kupinski
Northwest Utilities Service Co.
P. O. Box 270
Hartford, CT 06101

M. Schwartz
2244 University Avenue
Sacramento, CA 95825

No. of Copies

D. Woods
Ralph M. Parsons Co.
700 West Walnut Street
Pasadena, CA 91124

A. A. Fuierer
Rochester Gas and Electric Corporation
89 East Avenue
Rochester, NY 14649-0001

D. Stahl
SAIC
101 Convention Center Drive
Suite 407
Las Vegas, Nevada 89109

G. C. Allen
Sandia National Laboratory
Division 6323
Transportation Technology Center
P.O. Box 5800
Albuquerque, NM 87185

J. F. Ney
Sandia National Laboratory
Division 6323
Transportation Technology Center
P.O. Box 5800
Albuquerque, NM 87185

T. L. Sanders
Sandia National Laboratory
P.O. Box 5800
Albuquerque, NM 87185

E. Kuhns
Stone and Webster Engineering Corporation
1 Penn Plaza, 250 W. 34th St.
New York, NY 10119

E. Gordon
Transnuclear, Inc.
507 Newmark Esplanade
Rockville, MD 20850

J. Mangusi
Transnuclear, Inc.
1 N. Broadway
White Plains, NY 10601

No. of Copies

B. R. Teer
Transnuclear, Inc.
1 N. Broadway
White Plains, NY 10601

TRW, Exploration/Pro
P.O. Box 441807
Houston, TX 77244-1807

M. Keyhani
University of Tennessee
College of Engineering
414 Dougherty Eng. Bldg.
Knoxville, TN 37996-2210

R. J. Mullin
Tennessee Valley Authority
1101 Market St.
BR6N Space 40A
Chattanooga, TN 37402

F. C. Sturz
U.S. Nuclear Regulatory Commission
Office of Nuclear Materials Safety and Safeguards
Washington, DC 20555

C. Feldman
U.S. Nuclear Regulatory Commission
Office of Nuclear Materials Safety and Safeguards
Washington, DC 20555

W. R. Pearson
U.S. Nuclear Regulatory Commission
Regulatory Applications Division
MS NL-007
Washington, DC 20555

C. H. Peterson
U.S. Nuclear Regulatory Commission
Office of Nuclear Materials Safety and Safeguards
MS 623-SS
Washington, DC 20555

No. of
Copies

J. Roberts
U.S. Nuclear Regulatory
Commission
Office of Nuclear Materials
Safety and Safeguards
Washington, DC 20555

L. C. Rouse
U.S. Nuclear Regulatory
Commission
Division of Fuel Cycle
Material Safety
Washington, DC 20555

S. P. Turel
U.S. Nuclear Regulatory
Commission
Office of Nuclear Materials
Safety and Safeguards
Washington, DC 20555

P. K. Shaver
U.S. Tool and Die, Inc.
4030 Route 8
Allison Park, PA 15101

W. J. Wachter
U.S. Tool and Die, Inc.
1465 Glenn Avenue
Glenshaw, PA 15116

J. A. Nevshemal
Toledo Edison Co.
2155 Kathy Lane
Genoa, OH 43430

E. A. Bassler
Westinghouse Electric Corp.
P.O. Box 2728
Pittsburgh, PA 15230

C. F. Davis
Westinghouse Electric Corp.
Waste Technology Services Div.
P.O. Box 10864
Pittsburgh, PA 15236

K. M. Maloney
Department of Physics
Southern University
Baton Rouge, LA 70813

No. of
Copies

E. Benz
R. F. Weston Co.
955 L Enfant Plaza SW
8th Floor
Washington, DC 20024-2119

N. Dayem
R. F. Weston Co.
955 L Enfant Plaza SW
8th Floor
Washington, DC 20024-2119

T. Arul Mozhi
R. F. Weston Co.
955 L Enfant Plaza SW
8th Floor
Washington, DC 20024-2119

D. Stahl
Science Application
International Corp.
101 Convention Center Drive
Las Vegas, NV 89109

R. W. Knoll, M-36
Johnson Controls, Inc.
507 E. Michigan Street
Milwaukee, WI 53202

C. Pescatore
Brookhaven National Laboratory
Associated Universities, Inc.
Upton Long Island, NY 11973

P. S. Klanian
Westinghouse Electric Corp.
c/o West Valley Nuclear Services
P.O. Box 191
West Valley, NY 14171

P. K. Ray
Mechanical Engineering Dept.
Tuskegee University
Tuskegee, AL 36088

K. L. Walter
Department of Chemical
Engineering
Prairie View A & M Research
Foundation
Prairie View, TX 77446-0397

ONSITE

2 DOE Richland Operations Office

C. E. Collantes
E. C. Norman

1 Westinghouse Hanford Company

C. L. Brown

89 Pacific Northwest Laboratory

M. J. Apted
W. J. Bailey
J. O. Barner
C. E. Beyer
D. J. Bradley
H. C. Burkholder
L. A. Charlot
T. D. Chikalla
J. E. Coleman
J. M. Creer (5)
M. E. Cunningham
P. G. Doctor
R. E. Einziger
M. D. Freshley
E. R. Gilbert (20)
R. J. Guenther
R. F. Hazelton
C. M. Heeb
R. E. Heineman
A. B. Johnson, Jr.
M. R. Kreiter
D. D. Lanning
S. C. Marschman
J. L. McElroy
M. A. McKinnon
J.T.A. Roberts
E. P. Simonen
O. D. Slagle
H. D. Smith
R. I. Smith
J. L. Straalslund
L. A. Strope
L. E. Thomas (25)
C. K. Thornhill
R. C. Walling
C. N. Wilson
Publishing Coordination
Technical Report Files (5)